

C. Examples of numerical simulation by the model

So far, the model has been successfully applied to simulations of convective clouds (Ikawa *et al.*, 1987; Ikawa, 1988), mountain waves (Ikawa and Nagasawa, 1989; Ikawa, 1990; Saito and Ikawa, 1991) and orographic convective rainfall (Ikawa, 1985). However, they are mostly 2-dimensional. The verification of the model was made by comparing model results with 2-dimensional nonlinear analytic solutions of hydrostatic mountain waves by Lilly and Klemp (1979) (see Ikawa, 1988; Saito and Ikawa, 1991). In this chapter, the model will be checked against 3-dimensional linear analytic solutions of nonhydrostatic mountain waves. 3-dimensional simulations of local winds and convective snow clouds will be shown, with more refined and sophisticated parameterizations of physical processes than the older ones.

C-1. Verification of the model against 3-dimensional linear analytic solutions of nonhydrostatic mountain waves

In this section, the model-simulated mountain flow over a 3-dimensional mountain is verified by comparing it with the linear analytic solutions by Smith (1980).

C-1-1. Linear analytic solutions of 3-D nonhydrostatic mountain waves

For the steady flow of a vertically unbounded stratified Boussinesq fluid over a 3-dimensional small-amplitude topography, the following equation for vertical displacement of stream line $\delta(x, y, z)$ is obtained:

$$\frac{\partial^2}{\partial x^2} (\nabla^2 \delta) + \frac{N^2}{U^2} \nabla_H^2 \delta = 0, \quad (1-1)$$

where $\nabla_H^2 = \partial^2/\partial x^2 + \partial^2/\partial y^2$, $\nabla^2 = \nabla_H^2 + \partial^2/\partial z^2$, N is the Brunt-Väisälä frequency, and U is the environmental wind speed.

With constant N^2 and U^2 , the solution of Eq. (1-1) is easily obtained by using double Fourier transform analysis:

$$\delta(x, y, z) = \int \int_{-\infty}^{\infty} Z_s^{\sim}(k, l) e^{imz} e^{i(kx+ly)} dkdl, \quad (1-2)$$

where $Z_s^{\sim}(k, l)$ is the double Fourier transform of the mountain shape $Z_s(x, y)$ defined as

$$Z_s^{\sim}(k, l) = \frac{1}{4\pi^2} \int \int_{-\infty}^{\infty} Z_s(x, y) e^{-i(kx+ly)} dx dy, \quad (1-3)$$

m in Eq. (1-2) is calculated by the horizontal wave number vector (k, l) as follows:

$$m^2 = \frac{k^2 + l^2}{k^2} \left(\frac{N^2}{U^2} - k^2 \right). \quad (1-4)$$

For $k^2 > N^2/U^2$, the positive imaginary root of Eq. (1-4) is chosen, and for $k^2 < N^2/U^2$, the sign of m is chosen to be the same as that of k in order to satisfy the upper radiation condition.

For the case of hydrostatic approximation, Eq. (1-4) is further simplified as follows:

$$m = \frac{N}{U} \frac{(k^2 + l^2)^{1/2}}{k}. \quad (1-5)$$

Once δ is obtained, the vertical velocity component w is easily obtained using the kinematic condition for steady flow

$$w = U \frac{\partial \delta}{\partial x}. \quad (1-6)$$

The bell-shaped mountain with circular contours

$$Z_s(x, y) = \frac{h_m}{(r^2/a^2 + 1)^{3/2}}; \quad r = (x^2 + y^2)^{1/2} \quad (1-7)$$

is used for an example of mountain shape, where “ h_m ” is the height of the mountaintop and “ a ” is the horizontal scale of the mountain. h_m is set to 100m, and typical atmospheric values of $U = 8\text{m/s}$ and $N = 0.01\text{s}^{-1}$ are chosen.

The analytic solution is calculated by using discrete complex Fourier transform. The mountain shape $Z_s(x, y)$ is discretized on the grid mesh with an interval $\Delta x = \Delta y = a/3$. The mesh size $Nx = Ny = 128$ is used.

C-1-2. Description of the numerical model

Numerical simulation is also performed and the experimental result is compared. In the simulation, the horizontal grid interval of $\Delta x = \Delta y = a/3$ is used, while the variable grid interval $\Delta z = 40\text{m} \sim 1200\text{m}$ is used for the vertical grid interval. The grid number of $(Nx, Ny, Nz) = (60, 40, 32)$ is used for Cases a) and b), while $(Nx, Ny, Nz) = (60, 21, 32)$ is used for Case c). The time interval $\Delta t = 30\text{sec}$ is used. The anelastic scheme with Boussinesq approximation is employed, and an absorbing layer is imposed at the highest 10 layers to prevent a false reflection of mountain wave from the upper boundary. Open lateral boundary condition is employed except for Case c). For the smooth start-up, the mountain height is initially set to zero, and it is raised linearly to the ordinary height (100m) during the first 60 time steps, equivalent to the model time of $t = 30\text{min}$.

C-1-3. Comparison between numerical and analytic solutions

a) Case with wide horizontal scale mountain shape

Firstly, we show the comparative results for the case of wide horizontal scale mountain shape. In Eq. (1-7), the horizontal scale “ a ” is set to 6km. In this case, the product of the Scorer number N/U and “ a ” is 7.5, which means that the horizontal scale of the mountain is much larger than the distance of down-wind drift during a buoyancy oscillation. The nonhydrostatic effect is expected to be small. The horizontal grid interval of $\Delta x = \Delta y = 2\text{km}$ is used for the calculation of the analytic solution and the numerical simulation.

Figures C-1-1 a) ~ d) show the vertical velocity w at various levels obtained by the nonhydrostatic analytic solution. In these figures, the altitudes are $z = 2.44\text{km}$, 1.30km , 0.74km and 0.34km in order, and correspond to $zN/U \simeq \pi$, $\pi/2$, $\pi/4$ and $\pi/8$. The mountaintop is located at $x = y = 127\text{km}$, and the area from $x = 96\text{km}$ to $x = 190\text{km}$ and $y = 96\text{km}$ to $y = 158\text{km}$ is shown. Near the ground, the pattern of the updraft in the windward side and the pattern of the downdraft in the lee side are roughly symmetric as shown in Fig. C-1-1 d). However, the updraft in the windward side diminishes with the height, and it almost disappears in Fig. C-1-1 b) ($z = 1.3\text{km}$). On the other hand, another U-shaped updraft region develops in the lee, and the patterns of the vertical velocity become asymmetric further aloft.

Figures C-1-1 e) ~ h) show the vertical velocity w at various levels obtained by the numerical simulation after $240\Delta t$ ($t = 120\text{min}$). In these figures, the altitudes are about 2.44km , 1.30km , 0.74km and 0.34km above the ground surface in order, and correspond to the 12th, 9th, 7th and 4th level of the model. In this case, the dimensions of the model domain are $(Lx, Ly) = (118\text{km}, 78\text{km})$, and the mountaintop is located at $x = y = 39\text{km}$. The area from $x = 8\text{km}$ to $x = 102\text{km}$ and $y = 8\text{km}$ to $y = 70\text{km}$ is shown in these figures.

As shown in Figs. C-1-1 g) and h), near the ground the pattern of w by the model agrees well with those by the analytic solution except for the small numerical noises. Further aloft, although the width of the U-shaped updraft region in the lee in Fig. C-1-1 e) is somewhat smaller than in Fig. C-1-1 a), the characteristics of the pattern of w by the analytic solution are well reproduced by the simulation.

Figures C-1-3 a), b) show the vertical cross-section of w through the vicinity of the mountaintop (at $y = 126\text{km}$) obtained by hydrostatic and nonhydrostatic analytic solutions. They quite resemble each other since the hydrostatic approximation is applicable in this case. Fig. C-1-3 c) shows the vertical cross section of w through the vicinity of the mountaintop

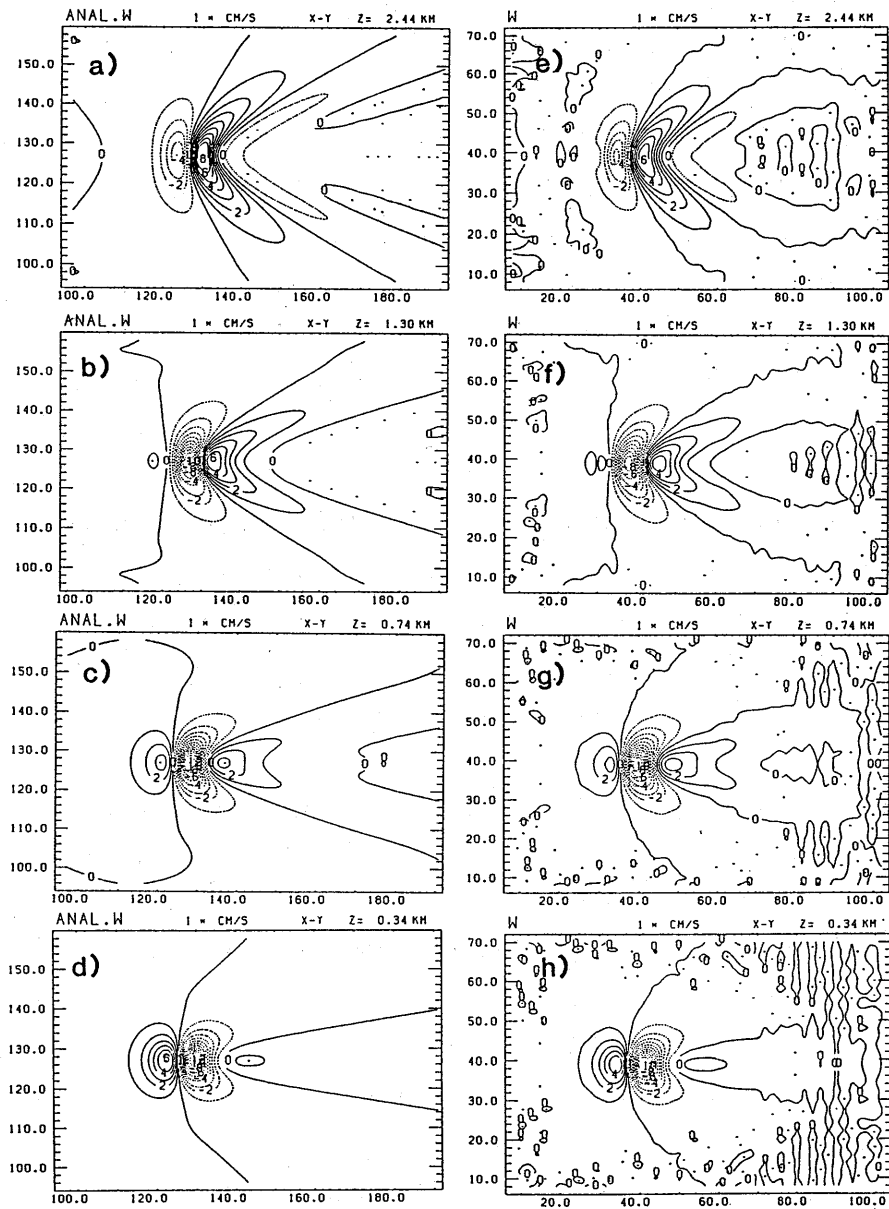


Fig. C-1-1 a) ~ d) Horizontal cross-section of vertical velocity (w) at various levels obtained by the non-hydrostatic analytic solution for the case of $aN/U = 7.5$ ($U = 8$ m/s, $N = 0.01$ s $^{-1}$, $a = 6$ km), $h_m = 100$ m. The altitudes are indicated at the upper right of each figure. The contour interval is 1 cm/s.

e) ~ h) Horizontal cross-section of w at various levels by the numerical simulation ($t = 120$ min). The altitudes above the ground surface (z^*) are indicated at the upper right of each figure.

(at $y = 38\text{km}$) obtained by numerical simulation. Although the model-simulated mountain wave decreases with the increase of the height mainly by the imposed absorbing layer, the characteristic of the mountain wave which propagates vertically is well reproduced.

b) Case with small horizontal scale mountain shape

Secondly, a comparison is performed for the case of smaller horizontal scale mountain shape. In Eq. (1-7), smaller horizontal scale of $a = 1.2\text{km}$ is used. The height of the mountaintop h_m , the atmospheric values U and N are the same as those of the former case. In this case, the product of the Scorer number N/U and " a " is 1.5, and nonhydrostatic effect is expected to become significant. Horizontal grid interval of $\Delta x = \Delta y = 400\text{m}$ is used for the calculation of the analytic solution and the numerical simulation.

Figures C-1-2 a) ~ d) show the vertical velocity w at various levels obtained by the nonhydrostatic analytic solution. In these figures, the altitudes are the same as in Figs. C-1-1 a) ~ d). The mountaintop is located at $x = y = 25.4\text{km}$, and the area from $x = 19.2\text{km}$ to $x = 38.0\text{km}$ and $y = 19.2\text{km}$ to $y = 31.6\text{km}$ is shown. The contour interval of these figures is five times larger than that used in Fig. C-1-1 owing to the increasing of the incline of the mountain slope. On comparing these figures with Figs. C-1-1, the trailing lee waves appear in the lee of a U-shaped updraft region. These trailing lee waves with horizontal wavelength of $2\pi U/N$ ($\simeq 5\text{km}$) are due to the buoyancy oscillation by the nonhydrostatic effect.

Figures C-1-2 e) ~ h) show the vertical velocity w at various levels obtained by the numerical simulation after $120\Delta t$ ($t = 60\text{min}$). In these figures, the altitudes are the same as in Figs. C-1-1 e) ~ f). The dimensions of the model domain are $(Lx, Ly) = (23.6\text{km}, 15.6\text{km})$, and the mountaintop is located at $x = y = 7.8\text{km}$. The area from $x = 1.6\text{km}$ to $x = 20.4\text{km}$ and $y = 1.6\text{km}$ to $y = 14.0\text{km}$ is shown in these figures, where the model-simulated flows agree quite well with the results of nonhydrostatic analytic solutions shown in Figs. C-1-2 a) ~ d). The lee oscillations due to the nonhydrostatic effect are also well reproduced by the simulation.

Figures C-1-3 d) and e) show the vertical cross-section of w through the vicinity of the mountaintop (at $y = 25.2\text{km}$) obtained by the hydrostatic and nonhydrostatic analytic solutions. In the case of the hydrostatic solution shown in Fig. C-1-3 d), the pattern of w is the same as in Fig. C-1-3 a) except for the contour interval. On the other hand, in the case of the nonhydrostatic solution shown in Fig. C-1-3 e), the pattern of w is quite different from Fig. C-1-3 b). The difference between them is due to the buoyancy oscillation

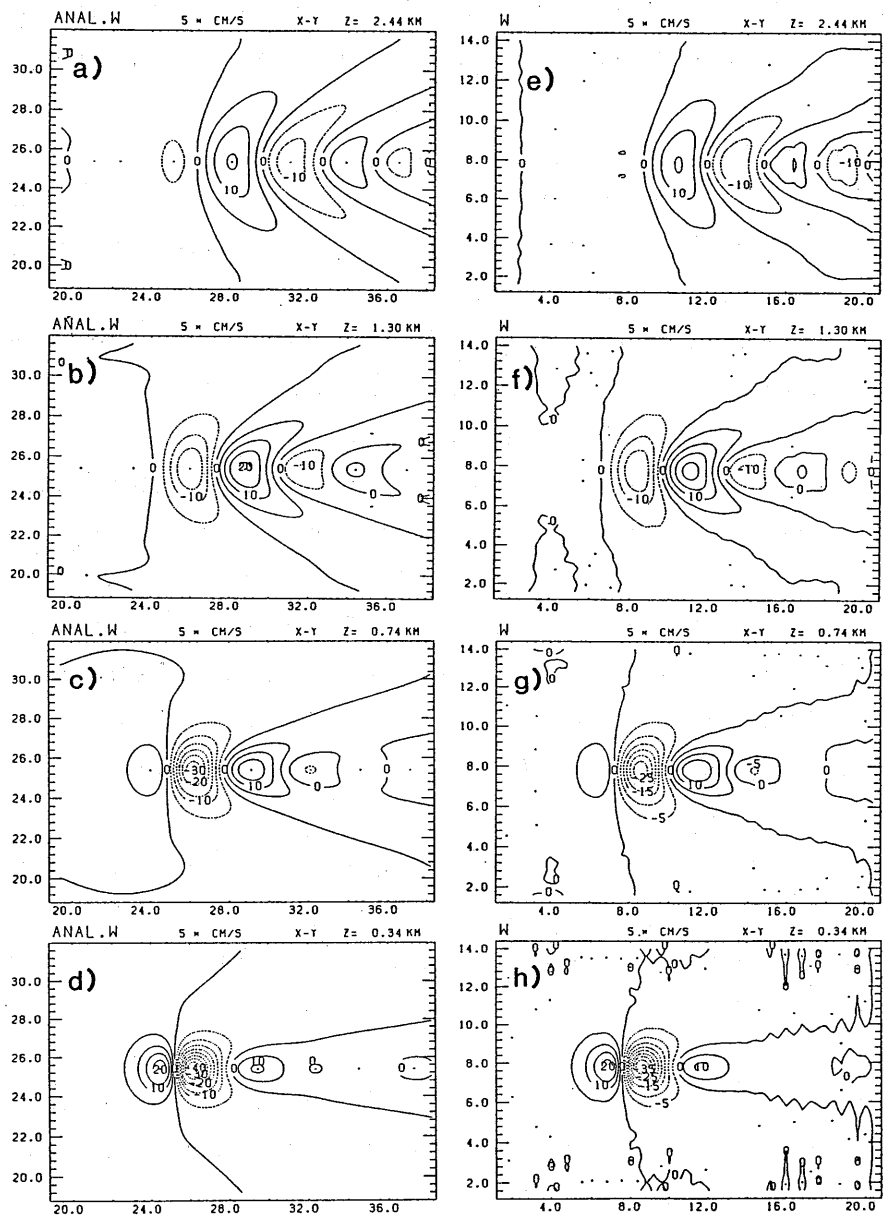


Fig. C-1-2 a) ~ h) As in Figs. C-1-1 a) ~ h) but for $aN/U = 1.5$ ($a = 1.2$ km). The contour interval is 5 cm/s.

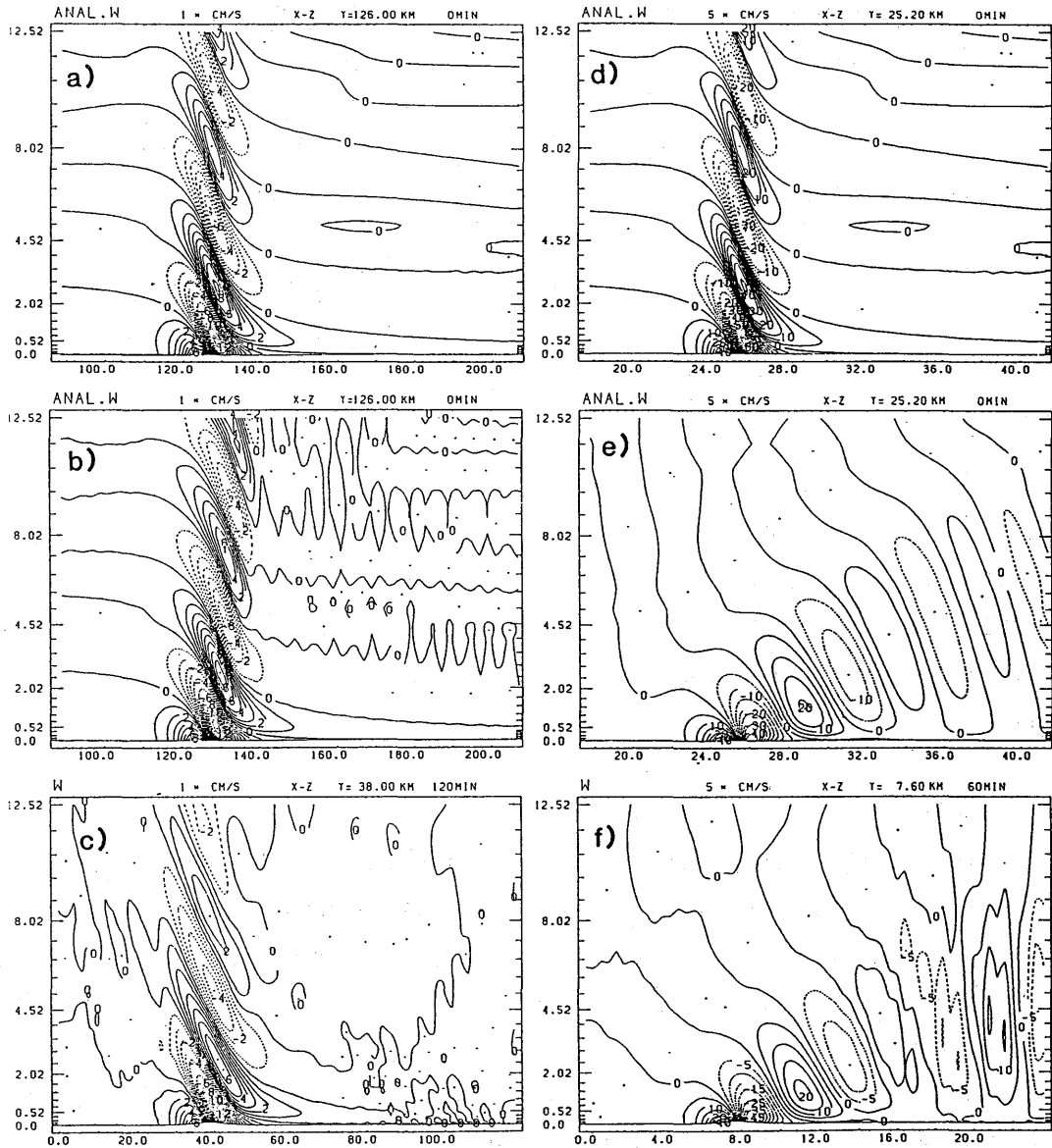


Fig. C-1-3 a) The vertical cross-section of w in the vicinity of the mountaintop obtained by the hydrostatic analytic solution for the case of $aN/U = 7.5$ ($a = 6$ km). The contour interval is 1 cm/s. The graduations on the vertical axis show the altitudes of the levels of the numerical model corresponding to the variable vertical grid interval.
 b) As in a) but by the nonhydrostatic analytic solution.
 c) As a) but by the numerical simulation.
 d) ~ f) As in a) ~ c) but for $aN/U = 1.5$ ($a = 1.2$ km). The contour interval is 5 cm/s.

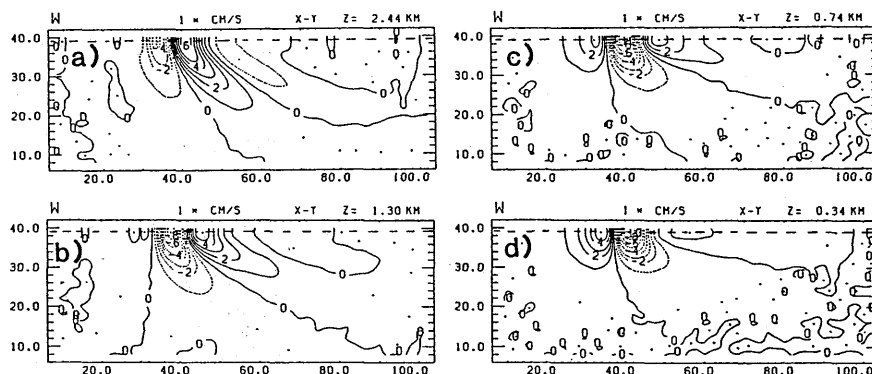


Fig. C-1-4 a) ~ d) As in Figs. C-1-1 e) ~ h) but by the numerical simulation with half domain. Broken line along $y = 39$ km shows the location of free-slip lateral boundary.

by the nonhydrostatic effect. Fig. C-1-3 f) shows the vertical cross-section of w through the vicinity of the mountaintop (at $y = 7.6$ km) obtained by the numerical simulation. The model-simulated flow well agrees with the result of the nonhydrostatic analytic solution shown in Fig. C-1-3 e). The open lateral boundaries located at $x = 0.2$ km and 23.2 km using radiation condition appear to work well.

c) Case with half domain

In the examples of numerical simulation shown in the former sub-sections, a bell-shaped mountain with circular contours was used for the mountain shape. The mountain waves indicated in Figs. C-1-1 and C-1-2 have symmetric patterns with respect to the xz -plane through the mountaintop. In the case of the simulation of such a symmetric flow, we can save the numerical resources by the use of free-slip rigid wall lateral boundary condition with half domain. In this sub-section, the open lateral boundary condition is used for only yz -planes at inflow and outflow sides, while the free-slip lateral boundary condition is used for the xz -planes. A bell-shaped mountain with $a = 6$ km is given for the mountain shape as in Case a), but the model domain is reduced to half of Case a). The grid number of $(Nx, Ny, Nz) = (60, 21, 32)$ is used.

Figures C-1-4 a) ~ d) show the vertical velocity w at various levels obtained by the numerical simulation with half domain ($t = 120$ min). In these figures, the altitudes of the cross-sectional planes are the same as in Figs. C-1-1 e) ~ h). In this case, the dimensions of the model domain are $(Lx, Ly) = (118$ km, 40 km) and the mountaintop is located at

$x = y = 39\text{km}$. The rigid wall lateral boundaries are located at the xz -planes through the mountaintop (along $y = 39\text{km}$, shown by broken line) and at $y = 1\text{km}$. As shown in these figures, the patterns of w quite agree with the results of full domain simulation shown in Figs. C-1-1 e) ~ h).

Generally, the flow obtained by the simulation using half domain with free-slip lateral boundaries agrees with the flow obtained by the simulation using full domain with symmetric orography and periodic lateral boundaries.

C-2. 3-dimensional simulations of local winds in Japan

In this section, 3-dimensional simulations of local winds in Japan are shown as examples of numerical simulation. Although these are preliminary experiments using simple environmental conditions, these results show us that the model has the potentiality for the future realistic simulation.

C-2-1. Land-sea breeze in the Kanto district

Originally designed to simulate convective phenomena, our nonhydrostatic model is applicable to such phenomena as the land-sea breeze since the model includes the physical processes. Circulations by the land-sea breeze are generally moderate phenomena and hydrostatic approximation is available in most cases, while simulation of them is a good test of the model's physical processes for the boundary layer. In this sub-section, we will show the results of the 3-dimensional simulation of the land-sea breeze in the Kanto district and

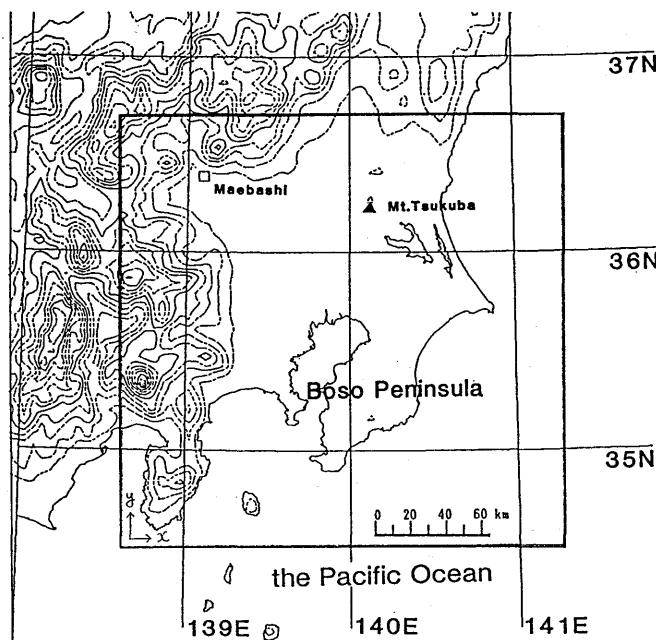


Fig. C-2-1 Geographical map of the Kanto district. The rectangle framed by heavy solid lines shows the area where the simulation is performed. The height contour interval is 200m.

show the performance of the model.

Figure C-2-1 shows a geographical map of the Kanto district. In this figure, the rectangle framed by heavy solid lines shows the area where the simulation is performed. In the simulation, this area is represented by $(Nx, Ny, Nz) = (50, 50, 22)$ grid points. The horizontal grid interval $\Delta x = \Delta y = 5\text{km}$ is used, while the variable grid interval $\Delta z = 40\text{m} \sim 800\text{m}$ is used for the vertical grid interval. The dimensions of the model domain are $(Lx, Ly, H) = (245\text{km}, 245\text{km}, 8.0\text{km})$.

In the simulation, anelastic equations are used, while the Boussinesq approximation is not employed. The environmental wind is set to zero, considering that the simulation of a day in which synoptic wind is weak. A constant lapse rate of $d\theta/dz = 3\text{K/km}$ ($N = 0.01\text{s}^{-1}$) is chosen for the typical atmospheric stability. The sea surface temperature is fixed at 15°C , while the ground temperature Tg is given by the following sinusoidal function with an amplitude of 10°C :

$$Tg = T_{\text{ref}} + 10 \sin\left(\frac{2\pi t}{T}\right), \quad (2-1)$$

where T_{ref} is the temperature of the reference atmosphere at the model surface which is calculated using surface height with a constant lapse rate of $d\theta/dz = 3\text{K/km}$, and T is a period of 24hours. The time interval of $\Delta t = 20\text{sec}$ is used, and the simulation is performed until $t = 8\text{hours}$ ($1440\Delta t$). The roughness length of the ground surface is assumed to be 10cm. The Coriolis parameter of $f = 8.57 \times 10^{-5}\text{s}^{-1}$ is used, corresponding to the latitude of the Kanto district (36°N).

Figure C-2-2 a) shows the simulated wind vectors at the lowest level (about 20m above the surface) after $720\Delta t$ ($t = 4\text{hrs}$). In this time, the ground temperature has risen about 8.5°C from the initial time. The valley breeze develops in the mountain area. Owing to the difference between the sea surface temperature and the ground temperature, sea breezes occur along the coast line.

Figure C-2-2 b) shows the simulated wind vectors at the lowest level after $1440\Delta t$ ($t = 8\text{hrs}$). In this time, the sea breeze intrudes into the land area and forms frontal lines in the plain area. In the mountain area, the valley wind further develops, and forms a large-scale circulation.

Figures C-2-3 a) ~ d) show the typical daily change of the surface wind in the Kanto district at every 3hours for a weak synoptic wind case, which was reported by Kawamura (1977). The simulated surface wind shown in Fig. C-2-2 b) well represents the characteristics

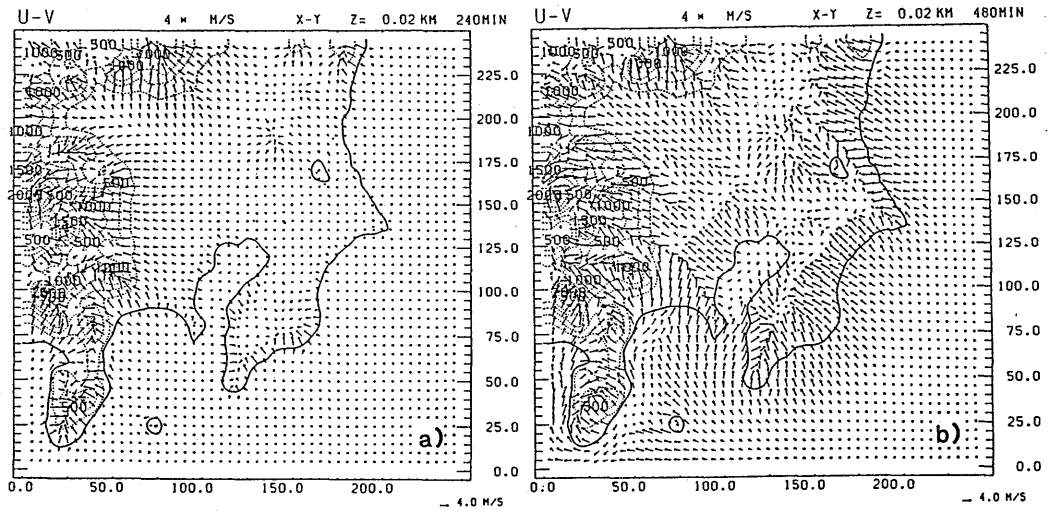


Fig. C-2-2 a) The simulated lowest level (about 20m above the surface) wind vectors at $t = 4$ hrs. The lower right arrow indicates the scale of 4 m/s. The broken lines mean height contour at every 250m.
 b) As in a) but for $t = 8$ hrs.

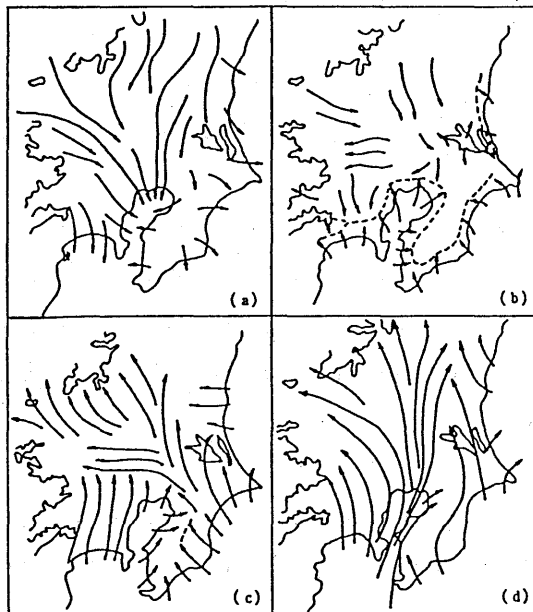


Fig. C-2-3 a) ~ d) The typical daily change of the surface wind in the Kanto District at every 3 hours reported by Kawamura (1977). a) 06LST, b) 09LST, c) 12LST, d) 15LST.

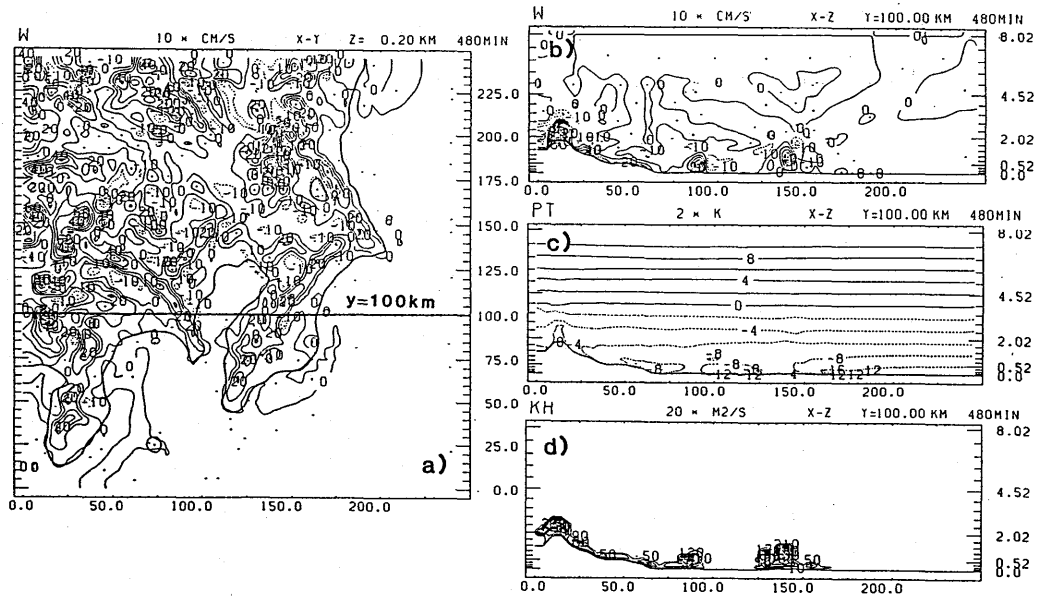


Fig. C-2-4 a) The vertical velocity (w) at the 4th level of the model (about 200m above the surface). The contour interval is 10 cm/s. Broken lines show the negative value (downward motion). Heavy line indicates the location of the vertical cross-section shown in Figs. C-2-4 b) ~ d).
 b) The vertical cross-section of the vertical velocity along $y = 100$ km (heavy line in Fig. C-2-4 a)). The contour interval is 10 cm/s. The graduations on the vertical axis show the altitudes of the levels of the model corresponding to the variable vertical grid interval.
 c) As in b) but for the potential temperature. The contour interval is 2K. Deviation from 300K is indicated.
 d) As in b) but for the diffusion coefficient determined by the turbulent closure model. The contour interval is 20 m^2/s .

of the typical circulation about 12LST in the Kanto district shown Fig. C-2-3 c).

Figure C-2-4 a) shows the vertical velocity at the 4th level of the model (about 200m above the surface) after 8hrs. The updrafts develop over the mountain area due to the positive buoyancy caused by the difference between the atmospheric temperature over the mountain area and the temperature of the reference atmosphere.

Figures C-2-4 b), c) and d) show the vertical cross-section of the vertical velocity, the potential temperature and the diffusion coefficient determined by the turbulent closure model along $y = 100$ km (shown by a heavy line in Fig. C-2-4 a)). The top-height of the updrafts is about 1km from the ground surface. On the ground surface, the diffusion coefficient is increased by the production of the turbulent energy due to the positive buoyancy production term.

C-2-2. Local downslope wind “Yamaji-kaze” in Shikoku Island

The “Yamaji-kaze” is one of the most well-known local winds in Japan. It is a strong downslope wind which occurs over the northern coastal plain of Shikoku Island when the low-level synoptic wind is southerly. Figure C-2-5 shows a geographical map of Shikoku Island, located in western Japan. In its northern central part, the Shikoku Mountains run from east to west. Mt. Ishizuchi (1981m) and Mt. Tsurugi (1955m) are located in the western and eastern part of the Shikoku Mountains, respectively. The central part of the Shikoku Mountains between Mt. Ishizuchi and Mt. Tsurugi is relatively low. The Yamaji-kaze occurs in the narrow northern slope of the Shikoku Mountains facing Hiuchi-nada. The most severe Yamaji-kaze occurs around Doi (○) and Mishima (⊙). Observational studies (Akiyama, 1956; *etc.*) have pointed out the following characteristic features of the Yamaji-kaze.

- a) A northerly wind opposite to the southerly synoptic wind is observed as one of the premonitory symptoms (“Sasoi-kaze”).
- b) In the early stage, the surface wind direction exhibits a sudden variation along a line of discontinuity (“Yamaji-kaze front”).
- c) A northerly wind opposite to the southerly downslope wind prevails over Hiuchi-nada (“Domai”).
- d) Strong winds are seldom observed on the windward side of Shikoku Island such as around

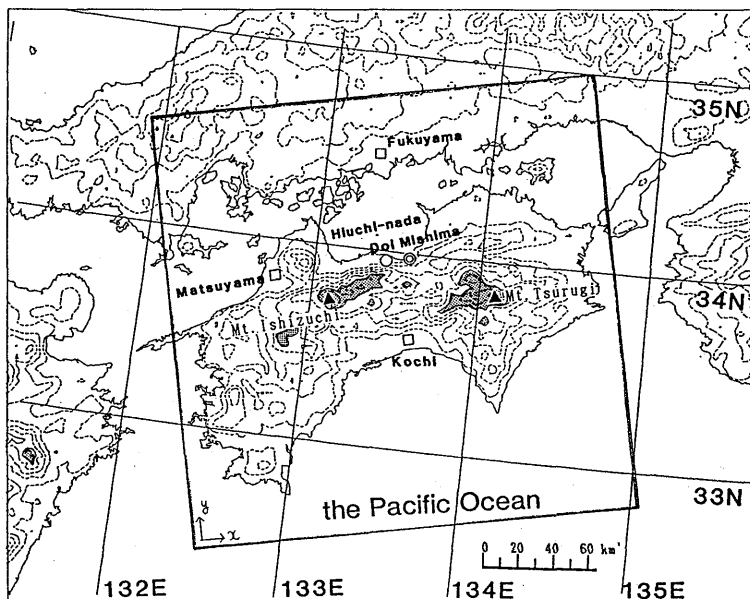


Fig. C-2-5 Geographical map of Shikoku Island, western Japan. The rectangle framed by solid lines shows the area where the simulation is performed. The height contour interval is 200m. The areas above 1000m height are shaded.

Kochi. e) Low surface pressures are observed in the coastal areas facing Hiuchi-nada ("Hiuchi-nada depression").

Saito and Ikawa (1991) made a numerical study of the Yamaji-kaze using a nonhydrostatic model and succeeded in explaining these phenomena in terms of the internal hydraulic jump and the reversed flow just behind it. However, their experiments were performed by 2-dimensional model using an averaged orography and physical processes such as the surface friction were neglected. As will be shown later, the Yamaji-kaze is evidently influenced by the complicated 3-dimensional effect of the actual orography. In this sub-section, we will show some examples of the experiments of 3-dimensional simulation of the Yamaji-kaze. In Fig. C-2-5, the rectangle framed by heavy solid lines shows the area where the simulation is performed. In the simulation, this area is represented by $(Nx, Ny, Nz) = (50, 50, 32)$ grid points. The horizontal grid interval $\Delta x = \Delta y = 5\text{km}$ is used, while the variable grid interval $\Delta z = 40\text{m} \sim 1200\text{m}$ is used for the vertical grid interval. The dimensions of the model domain are $(Lx, Ly, H) = (245\text{km}, 245\text{km}, 18.0\text{km})$.

In the simulation, anelastic equations are used, while the Boussinesq approximation is not employed. An absorbing layer is imposed at the highest 10 layers. The lower boundary is assumed to be thermally insulated and heat flux from the surface is neglected. The time interval of $\Delta t = 30\text{sec}$ is used, and the simulation is performed until $t = 4\text{hrs}$ ($480\Delta t$). For the smooth start-up, the height of orography is set to zero initially, and is raised linearly to the ordinary height during the first 60 time steps ($t = 30\text{min}$). The environmental wind is set to $V = 6\text{m/s}$, assuming a constant SSE-ly wind. A constant lapse rate of $d\theta/dz = 3\text{K/km}$ ($N \approx 0.01\text{s}^{-1}$) is chosen for the typical atmospheric stability.

Three kinds of experiment, a) no Coriolis force and no surface friction, b) Coriolis force and no surface friction, and c) Coriolis force and surface friction, are performed.

a) No Coriolis force and no surface friction

Firstly, the simulation is performed for the simplest condition with no Coriolis force and no surface friction. Figure C-2-6 a) shows the simulated wind vectors at the lowest level (about 20m above the surface) after $120\Delta t$ ($t = 1\text{hrs}$). The surface wind becomes weak in the windward side around Kochi by the blocking effect of the Shikoku Mountains, while it increases on their northern slope. The surface wind over Hiuchi-nada is yet southerly as the environmental wind. At $t = 2\text{hrs}$ (Fig. C-2-6 b)), the surface wind further increases around Doi and Mishima, in the lee of the col of the Shikoku Mountains. Over the western part of

Hiuch-nada, a notable weak wind area develops. This weak wind area is located just behind the hydraulic jump which is generated by the wave breaking. At $t = 3$ hrs (Fig. C-2-6 c)), the southerly wind around the eastern edge of Hiuchi-nada forms a jet-like area of strong wind. On the other hand, the surface wind over the western part of Hiuchi-nada turns to northerly, opposite to the southerly environmental wind. As shown in Fig. C-2-6 d), this northerly wind extends its area northward as the time elapses, and a cyclonic circulation is formed between this northerly wind and the strong southerly jet-like wind around the eastern edge of Hiuchi-nada. This northerly wind apparently corresponds to the "Domai",

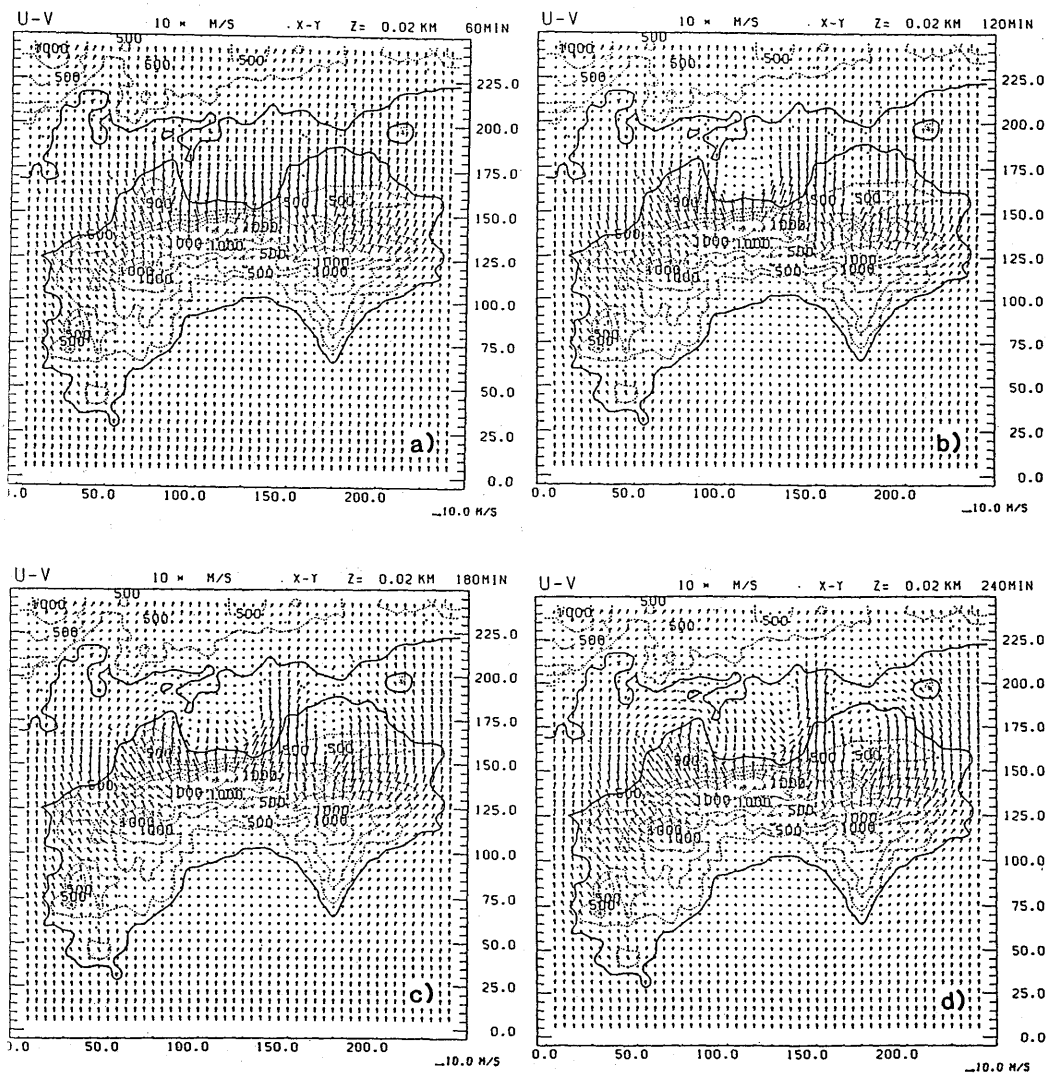


Fig. C-2-6 a) ~ d) The simulated lowest level ($z^* = 20$ m) wind vectors at every 1 hour. Lower right arrow indicates 10 m/s. The broken lines indicate height contour at every 250m.

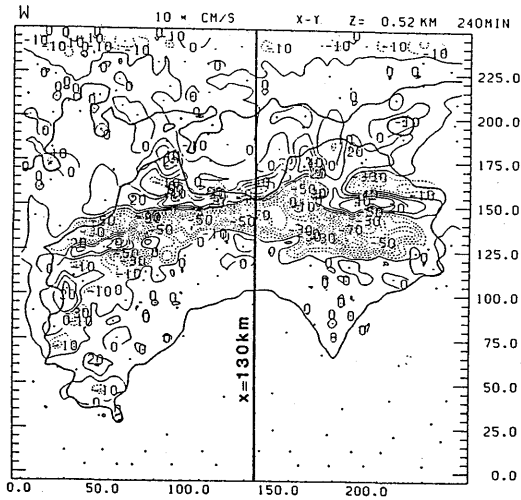


Fig. C-2-7 The vertical velocity (w) at the 4th level of the model (about 200m above the surface) and $t = 4$ hrs. The contour interval is 10 cm/s. Broken lines show the negative value (downward motion). Heavy line indicates the location of the vertical cross-section shown in Figs. C-2-8 a) ~ b).

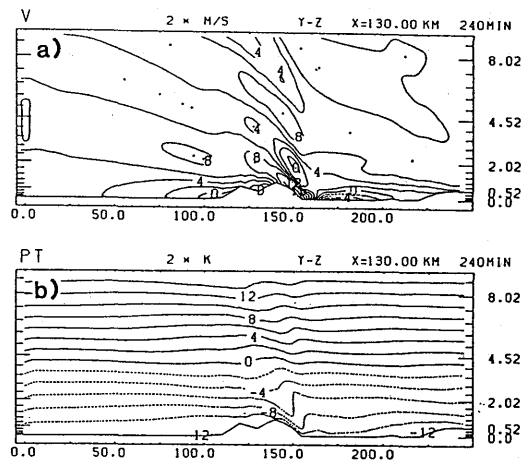


Fig. C-2-8 a) The vertical cross-section of the horizontal wind along $x = 130$ km (heavy line in Fig. C-2-7) at $t = 4$ hrs. The contour interval is 2 m/s. b) As in a) but for the potential temperature. The contour interval is 2K. Deviation from 300K is indicated.

one of the characteristic features of the Yamaji-kaze.

Figure C-2-7 shows the vertical velocity at the 4th level of the model (about 200m above the surface) at $t = 4$ hrs. A strong downdraft region which corresponds to the downslope wind is seen over the northern slope of the Shikoku Mountains, while another long and narrow updraft area is seen along the northern coast line facing Hiuchi-nada. This updraft area is located on the surface convergence between the southerly downslope wind and the northerly wind over Hiuchi-nada, and corresponds to the hydraulic jump.

Figures C-2-8 a), b) show the vertical cross-section of the southerly component of the horizontal wind and the potential temperature along $x = 130$ km (shown by a heavy line in Fig. C-2-7). In Fig. C-2-8 a), an area of negative horizontal wind which corresponds to the wave over-turning is seen at the level of 2km above the northern slope of the Shikoku Mountains at $y = 150$ km. A neutral stagnant layer is formed corresponding to this wave breaking, and the isentropes shown in Fig. C-2-8 b) are upright over the northern slope of the Mountains. Below it, the downslope wind greater than 16m/s is seen on their steep northern slope. The surface wind changes suddenly around $y = 160$ km. This abrupt change

corresponds to the internal hydraulic jump. On the north side of this abrupt change, a northerly wind greater 4m/s is seen over Hiuchi-nada.

b) Coriolis force and no surface friction

Secondly, the simulation is performed with the Coriolis force to check its effect on the Yamaji-kaze. Figure C-2-9 a) shows the simulated wind vectors at the lowest level after 4hrs. In this experiment, the Coriolis parameter of $f = 8.15 \times 10^{-5} \text{s}^{-1}$ is used, corresponding to the latitude of Shikoku Island (34 N). A geostrophic balanced field is given for the initial condition. On comparing this figure with Fig. C-2-6 d), the surface wind at the stagnant area around Kochi becomes a weak easterly wind. This slight westward component of the surface wind is caused by the westward pressure gradient force which originally balances eastward Coriolis force by the southerly environmental wind. The SE-ly surface wind in the north-western part of Shikoku Island around Matsuyama is enhanced by the effect of this westward pressure gradient force. No notable differences between Fig. C-2-6 d) and Fig. C-2-9 a) are seen in the flow patterns of the downslope wind and the northerly wind over Hiuchi-nada.

c) Coriolis force and surface friction

Next, the simulation is performed not only with the Coriolis force but also with the surface friction, whose effect on the Yamaji-kaze is tested. Over the land, the surface momentum fluxes are calculated from the similarity law, assuming a constant roughness length of 10cm and no heat fluxes. Over the sea, the surface momentum fluxes are determined from the formula by Kondo (1975), depending on the magnitude of the velocity of the surface wind. Figure C-2-9 b) shows the simulated wind vectors at the lowest level after $t = 4$ hrs. Compared with Fig. C-2-9 a), the surface wind is generally weak. The unnatural strong SE-ly wind around Matsuyama in Fig. C-2-9 a) is no longer seen and the strong southerly jet-like wind along the eastern edge of Hiuchi-nada is also reduced. On the other hand, the downslope wind around Doi is not so weakened, and the northerly wind over the western part of Hiuchi-nada is still obvious.

Figures C-2-10 a) and b) show the vertical cross-section of the southerly component of the horizontal wind and the potential temperature along $x = 130\text{km}$ (shown by a heavy solid line in Fig. C-2-7). Compared with Fig. C-2-8 a), the horizontal wind close to the ground surface is weakened by the effect of the surface friction, while the flow pattern is not

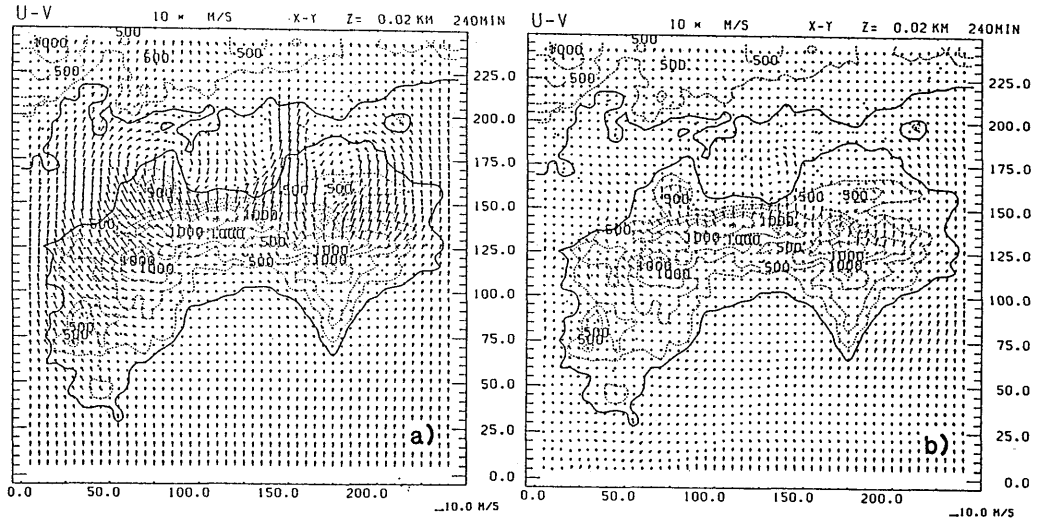


Fig. C-2-9 a) As in Fig. C-2-6 d) but for the case including Coriolis force in the simulation.
 b) As in a) but for the case including Coriolis force and the surface friction in the simulation.

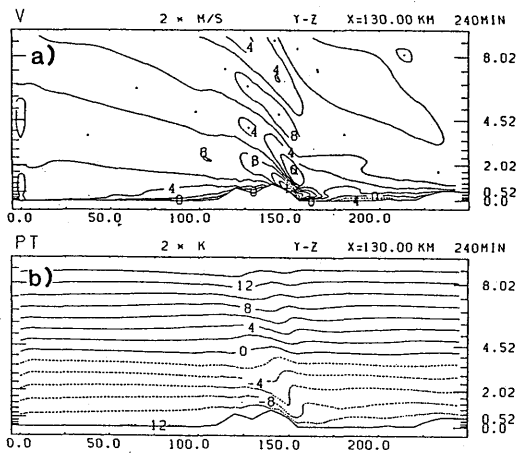


Fig. C-2-10 a), b) As in Figs. C-2-8 a), b) but for the case including Coriolis force and the surface friction in the simulation.

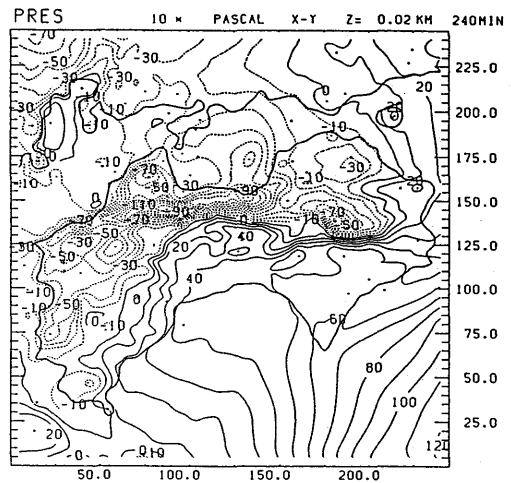


Fig. C-2-11 The simulated surface pressure deviation at $t = 4$ hrs. The contour interval is 10 hPa.

much different on the whole. An area of negative horizontal wind which corresponds to the wave over-turning is also seen at the level of 2km above the northern slope of the Shikoku Mountains at $y = 150$ km. Below it, the downslope wind greater than 14m/s is seen on their

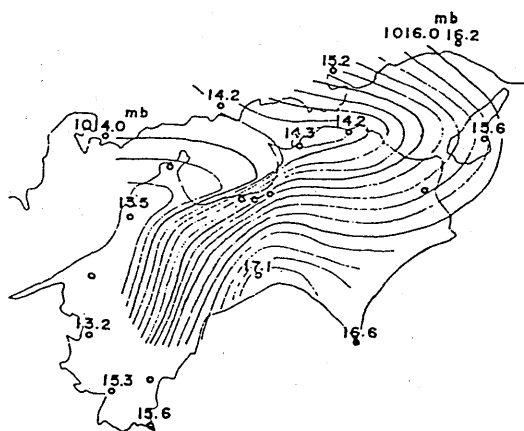


Fig. C-2-12 The averaged surface pressure in 4 hours observed in the Yamaji-kaze on 24 April, 1955. The contour interval is 0.2 mb. Adapted from Furukawa (1966).

northern slope. No notable differences are seen in the pattern of isentropes shown in Fig. C-2-10 b) either.

Figure C-2-11 shows the surface pressure deviation at $t = 4$ hrs. The surface pressure of the basic state is high on the east side and low on the west, balancing the Coriolis force by the southerly environmental wind, while it is high on the windward side of the Shikoku Mountains and low on the lee side. The magnitude of the minimum depression on the northern slope of the Mountains is about 1hPa. A low pressure area which corresponds to the location of the cyclonic circulation shown in Fig. C-2-9 b) is seen in the eastern part of Hiuchi-nada.

Figure C-2-12 shows the averaged surface pressure in 4 hours observed in the Yamaji-kaze on 24 April, 1955 (Furukawa, 1966). The surface pressure pattern shown in Fig. C-2-11 well expresses the characteristics of the observed surface pressure. The surface pressure deviation in the lee side of the Shikoku Mountains shown in Fig. C-2-12 is almost twice as great as that in Fig. C-2-11. It appears that this difference is caused by the difference of the magnitude of the environmental wind. The southerly synoptic wind in the lower level was greater than 10m/s in the observation of the Yamaji-kaze on 24 April 1955, while it is 6m/s in the simulation.

d) Remarks

The northerly wind over Hiuchi-nada simulated in the former sub-sections is believed to

have some inherent similarities to the reversed flow behind the hydraulic jump which was studied by Saito and Ikawa (1991). However there exists quantitative difference between the occurrence of the two reversed flows. In the 2-dimensional experiments with a homogeneous atmosphere using an averaged orography of Shikoku Island and the Chugoku Mountains by Saito and Ikawa (1991), the reversed flow behind a stationary jump occurred for the case of $U = 4\text{m/s}$, but the jump propagated leeward and the occurrence of the reversed flow was obscure for the case of $U = 6\text{m/s}$. In the 3-dimensional experiment shown in sub-section C-2-2 a), the hydraulic jump almost stays along the northern coast line facing Hiuchi-nada, and an obvious northerly wind develops on the north side of the jump for the case of $U = 6\text{m/s}$. Namely, the northerly wind over Hiuchi-nada occurs more readily for the case of 3-dimensional experiment. This difference appears to be mainly caused by the 3-dimensional effect of the orography of the Island. Considering the fact that the Yamaji-kaze is accompanied by the "Domai" except in extraordinarily strong synoptic wind cases, the easiness of the occurrence of the northerly wind over Hiuchi-nada which was shown in the 3-dimensional experiment appears to be an encouraging result.

It appears that the Yamaji-kaze is not considerably affected by the Coriolis force. However, the Coriolis force is indispensable to obtain the realistic pressure pattern such as is shown in Fig. C-2-11.

The magnitude of the surface wind by the Yamaji-kaze is significantly affected by the surface friction. It appears that the selective effect of the surface friction owing to the difference of the roughness on land and sea makes the flow pattern of the Yamaji-kaze more realistic.

As was stated before, the experiments shown here are preliminary ones using simple conditions. The horizontal resolution employed in the simulation (5km) may not be adequate. More experiments will be required for the further understanding of the effect of the 3-dimensional orography on the Yamaji-kaze and the behavior of its associated hydraulic jump.

Acknowledgement:

The authors wish to express their thanks to Professor Fujio Kimura of Tohoku University and Shunji Takahashi of the Applied Meteorological Research Division of the MRI for their helpful guidance about geographical data.

C-3. 3-dimensional simulation of the convective snow cloud observed over the Sea of Japan[†]

— Sensitivity to ice crystal nucleation rates —

C-3-1. Introduction

The coastal region of northern Japan, facing the Sea of Japan, is famous for its heavy snowfall (e.g., Matsumoto *et al.*, 1967). The heavy snowfall is associated with the abundant heat and moisture supply from the warm sea surface (10°C) into the cold air (0°C) blowing from Siberia (e.g., Ninomiya, 1968). The snowfall is brought about by convective snow clouds with the temperature of cloud base and top being $-5 \sim -10$ and $-20 \sim -30^\circ\text{C}$, respectively. However, the cloud microphysical aspects of the heavy snowfall have not been fully investigated yet, observationally or numerically.

Magono and Lee (1973) measured the vertical distribution of the shape, number concentration and mass of snow crystals and mass of cloud droplets at formative, mature and decaying stages of convective snow clouds around Otaru (43.2N, 141.0E) in Hokkaido, northern Japan, utilizing snow crystal sonde. Isono *et al.* (1966) measured the ice nucleus concentration and number precipitation rate of snow and graupel at Wajima (37.4N, 136.9E), and found a correlation between the two. Harimaya and Sato (1989) and Mizuno *et al.* (1990) measured the contribution ratio of riming to the growth of snow flakes and its dependence on meteorological conditions. Their studies suggest that the riming process is a primary process in precipitation formation of convective snow clouds. Recently, Murakami and Matsuo (1990) developed a Hydrometeor Video Sonde (HYVIS) which can measure the vertical distribution of hydrometeors utilizing two types of TV cameras, and Murakami *et al.* (1990) observed convective snow clouds at Tobishima (39.25N, 139.55E) by use of HYVIS. From these observations, it was revealed that few rain drops exist, and they do not play a dominant role in precipitation formation; instead, accretion of cloud droplets by graupel and snow (riming) play a significant role in precipitation formation as well as depositional process; the maximum number concentration of ice crystals amounts to 10^4 – 10^5m^{-3} , one or two orders larger than that predicted by Fletcher's formula. These observational studies

[†] This is a preliminary report on the research carried out in collaboration with H. Mizuno, T. Matsuo, M. Murakami and Y. Yamada, Physical Meteorology Research Division of the MRI (Ikawa *et al.*, 1991).

provide important and useful information about the cloud microphysical processes taking place in clouds. To supplement these observational studies, numerical and theoretical studies are needed, in addition to better organized intensive and extensive field observations.

Takahashi (1983) conducted numerical simulation of an isolated winter cumulus by use of a 2-dimensional (axisymmetric) model with highly sophisticated cloud microphysics, the so-called bin method, focusing on the electrification. Ikawa *et al.* (1987) and Ikawa (1988a) simulated the convective cloud band observed over the Sea of Japan (Sakakibara *et al.*, 1988) by use of a 2-dimensional model with a bulk parameterization scheme of cloud microphysics where the mixing ratios of water vapor, cloud water, cloud ice, snow and graupel are predicted. Ikawa (1988) demonstrated that the dominant processes in precipitation formation are the condensation of water vapor to form supercooled cloud droplets and accretion of them (riming) by snow and graupel, rather than the depositional growth of ice particles. However, his simulation is 2-dimensional, and the bulk parameterization adopted in his model does not predict the number concentrations of cloud ice (pristine ice crystals), snow (ice crystals greater than pristine ice crystals and snow aggregates) and graupel, and has some ambiguous (or ad-hoc) parts in the parameterization of ice nucleation.

Recently, Cotton *et al.* (1986) and Murakami (1990) developed the bulk parameterization schemes of cloud microphysics in which the number concentrations of ice crystals and snow aggregates are predicted in addition to the mixing ratios of water substances. Cotton *et al.* applied the scheme to the simulation of orographic snowfall from stratiform clouds observed in Colorado in winter. Murakami applied his scheme to the convective cloud observed in Montana in summer. Their schemes appear to be promising for realistic simulation of clouds.

One of the purposes of this paper is to present a bulk parameterization of cloud microphysics which predicts not only the number concentrations of cloud ice and snow but also that of graupel in addition to the mixing ratios of six forms of water substance (water vapor, cloud water, rain, cloud ice, snow and graupel). The parameterization will be applied to a 3-dimensional simulation of the convective snow cloud observed over the Sea of Japan. The results will be compared with observations, and the performance and the insufficient parts of the parameterization scheme will be discussed.

Another purpose of this paper is to examine what the dominant processes are in forming precipitable particles and what the effects of ice nucleation rates are on precipitation formation. There have been many controversies on the disagreement between the number concentrations of ice crystals and ice-forming nuclei. Therefore, sensitivity experiments to

varying ice nucleation rates become necessary. These experiments may shed some light on the mechanism of the high number concentration of the observed ice particles and be useful in the assessment of the effect of seeding over the natural convective snow cloud.

In section C-3-2, observations of the cloud to be simulated are shown. In section C-3-3, the numerical model is described; in section C-3-4, experimental design is given. In section C-3-5, the results of the reference experiment are shown. In section C-3-6, the results of sensitivity experiments are shown and compared with each other. In section C-3-7, numerical results are compared with observations. In section C-3-8, the summary and conclusions are given.

C-3-2. Observations of the convective cloud

Special observations of convective clouds were conducted in winter from 1989 to 1991 by the joint research group consisting of members of the MRI, the Institute of Low Temperature Science of Hokkaido University, and the National Research Center for Disaster Prevention, by use of dual Doppler radars, HYVIS and other instruments. An isolated convective snow cloud was observed at 1500LST on Feb. 4, 1989 on Tobishima Island (39.25N, 139.55E), 30km north-west off the coast of Sakata, northern Japan. This cloud is the object of the 3-dimensional simulation.

The synoptic chart of surface pressure at 0900LST is shown in Fig. C-3-1. The vertical profiles of wind, temperature and relative humidity are displayed in Fig. C-3-2. A HYVIS was launched into the cloud successfully, and measured the liquid water content, number concentration of cloud droplets and ice crystals in addition to temperature and relative humidity as a function of height, as displayed in Fig. C-3-3 (Murakami *et al.*, 1990). In counting the number of ice particles, those which are of amorphous shape or smaller than $50\mu\text{m}$ in diameter are excluded. Ice particles of amorphous shape appear to be fragments produced by collision of ice particles with the sampling surface. If they are included, the maximum number of ice particles around $z = 2.0\text{km}$ is $2 \times 10^6\text{m}^{-3}$. From the figure, it is noticed that the number concentration of ice crystals is very large as compared to 10^3m^{-3} expected from Fletcher's formula for the cloud top temperature of -20°C , and in spite of the presence of this large number of ice crystals, there exists cloud water as much as $0.1\text{g}/\text{m}^3$. As seen from radar reflectivity patterns shown in Fig. C-3-4 (Yamada *et al.*, 1990), the horizontal and vertical scales of the convective cloud is about 5km and 3km, with the maximum reflectivity less than 30dBZ.

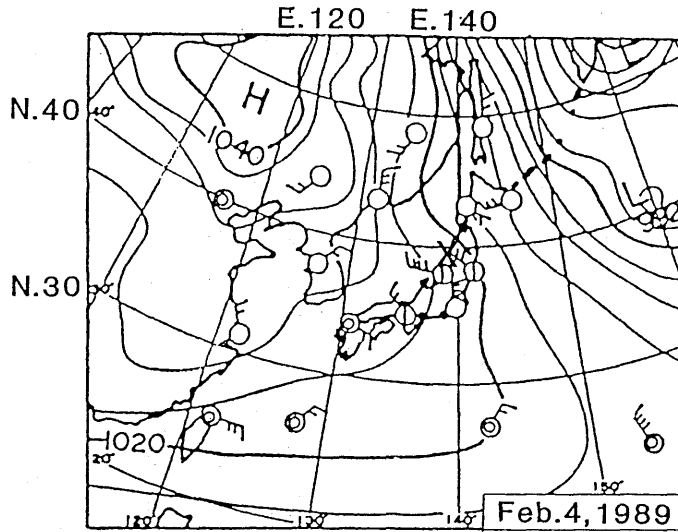


Fig. C-3-1 Surface synoptic pressure chart at 0900LST, Feb. 4, 1989 with the contour interval of 4 hPa. Observation area is indicated by x.

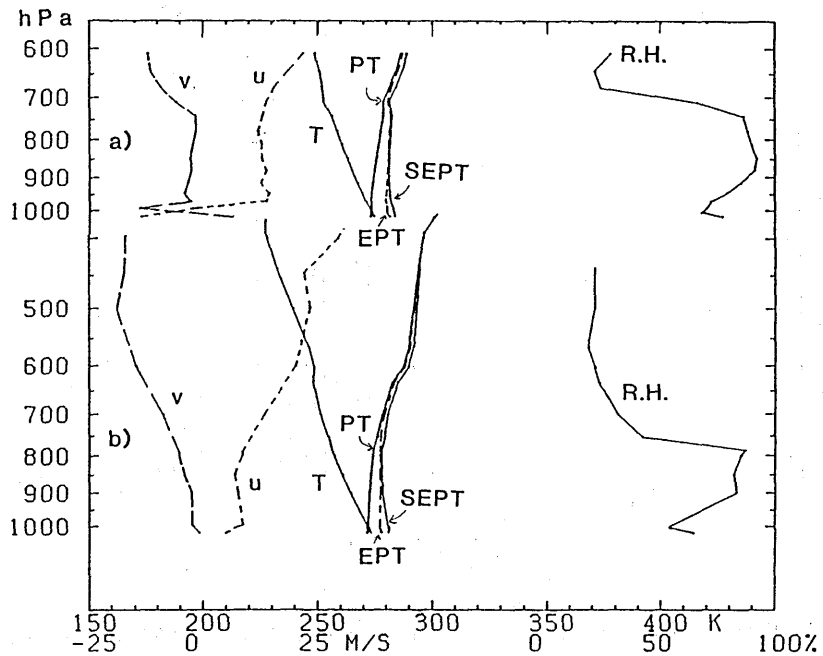


Fig. C-3-2 Vertical profiles of wind (u, west-east component; v, south-north component), temperature (T), potential temperature (PT), equivalent potential temperature (EPT), saturation equivalent potential temperature (SEPT) and relative humidity (R.H.). a) at 1500LST, Feb. 4, 1989 at To-bishima. b) at 0900LST, Feb. 4, at Akita (39.72N, 140.10E).

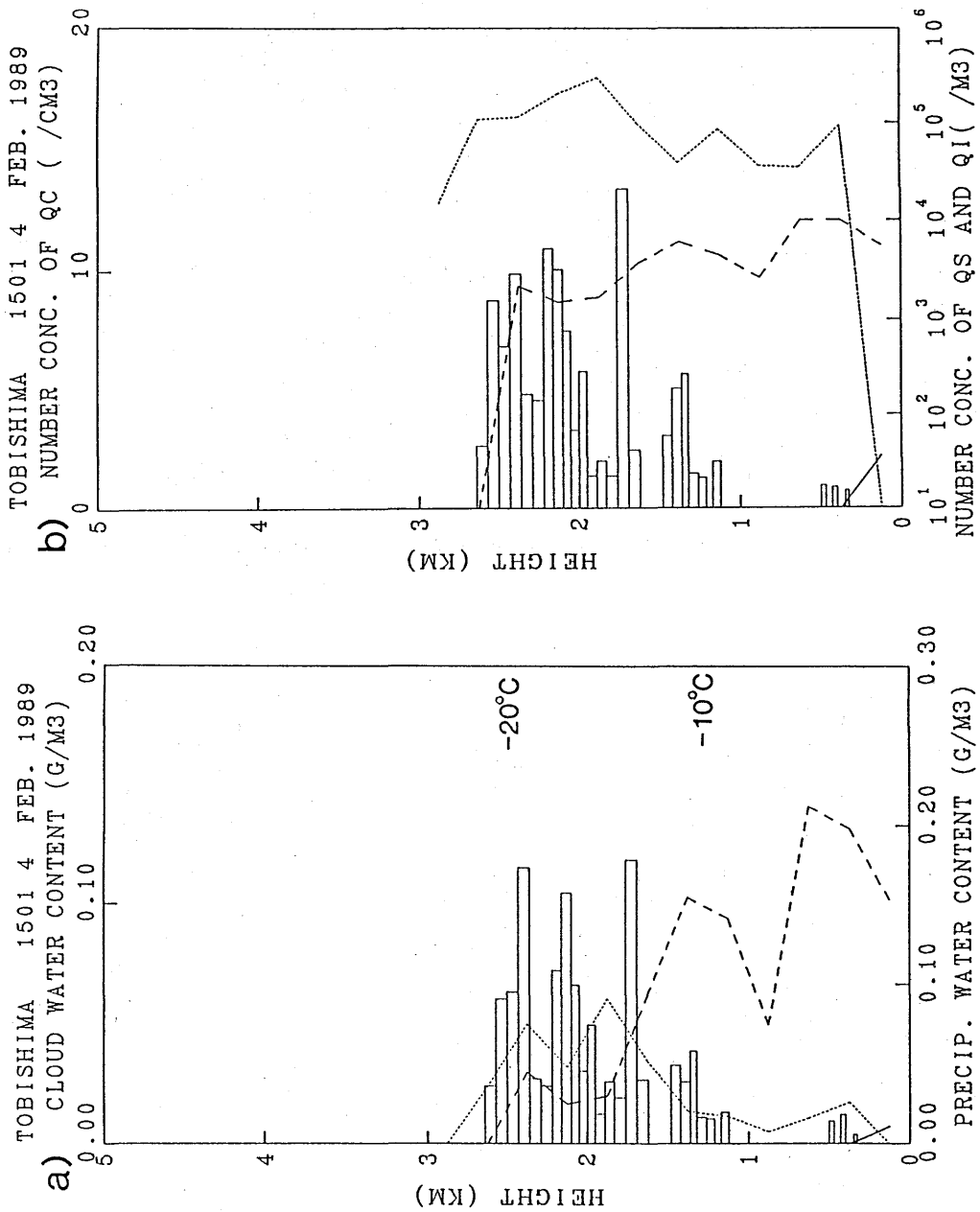
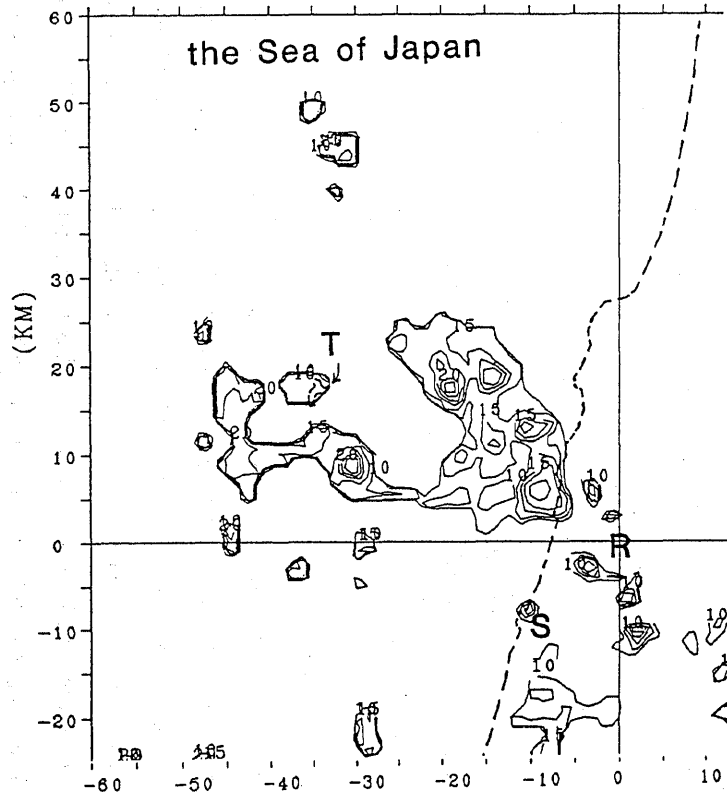


Fig. C-3-3 Vertical distribution of hydrometeors measured by HYVIS, 1500LST, Feb. 4, 1989 (Courtesy to Murakami *et al.*, 1990).

- a) Cloud water contents (gm^{-3}), water contents of ice particles smaller than $300 \mu\text{m}$ in diameter (dotted line) and of those larger than $300 \mu\text{m}$ in diameter (broken line).
- b) Number concentrations of cloud droplets (cm^{-3}), ice crystals smaller than $300 \mu\text{m}$ in diameter (dotted line), and ice particles larger than $300 \mu\text{m}$ in diameter (broken line).

a) MRI 3CM DOPPLER RADAR
890204 145828 EL=1.7



b) MRI 3-CM DOPPLER REI
890204 145959 SAKATA
AZ=300.1

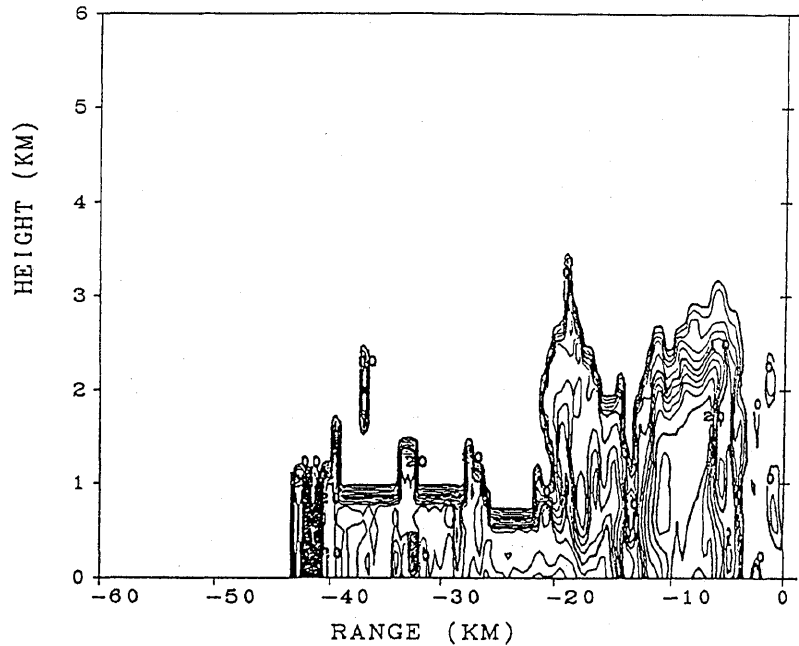


Fig. C-3-4 a) Radar echo patterns (PPI scan) at the elevation angle of 1.7° observed at 1500LST, Feb. 4, 1989. Contour interval is 2.5 dBZ. The locations of the radar site, Tobishima Island and Sakata, are indicated by R, T and S, respectively.
b) Radar echo patterns (REI scan) at the azimuth angle of 300° . Contour interval is 2.5 dBZ. The location of the radar site is at $x = 0$ km. (Courtesy to Yamada *et al.*, 1990).

C-3-3. Numerical model and parameterization of cloud microphysics

The numerical model is basically the same as Ikawa *et al.* (1987) unless specifically mentioned; the dynamical frame is mainly based on Clark (1977); subgrid turbulent mixing terms are parameterized based on Klemp and Wilhelmson (1978) and Deardorff (1980); for the time integration, E-HI-VI scheme (Ikawa, 1988) is used with the time averaging parameter of implicit scheme, $\alpha < 0.5$ (see Eq. (20) in Ikawa, 1988), the coefficient for the Robert-Asselin time filter, $\nu = 0.15$.

Parameterization of cloud microphysics is described in B-11 in this technical report.

The dimensions of the domain are $(LX, LY, LZ) = (10.0\text{km}, 10.0\text{km}, 4.35\text{km})$, with the grid number of $(NX, NY, NZ) = (26, 26, 26)$. Variable grid mesh is used in the z -coordinate, whose grid distance varies from 20m (below $z = 30\text{m}$) to 200m (above $z = 1.2\text{km}$). The lowest grid point is placed at $z = 10\text{m}$. The leap-frog time integration is used with the time interval of $\Delta t = 4\text{s}$. The lateral boundary condition is cyclic. The lower boundary is assumed to be the sea surface with a temperature of 10°C , and latent and sensible heat fluxes and momentum fluxes from the sea surface are calculated by use of the resistance law based on Kondo's work (see Ikawa *et al.*, 1987).

C-3-4. Experimental design

There is much uncertainty about ice nucleation. As will be shown later, the observed high number concentration of ice particles is 4 times larger than the maximum number concentration of ice particles simulated by the model where parameterizations for ice nucleation terms are based on three conventional theories, *i.e.*, Fletcher's deposition/sorption nucleation, Bigg's freezing of cloud droplets and Hallet-Mossop rime-splinter ice multiplication. The simulated radar reflectivity is larger by 10dBZ than the observed one (30dBZ). To simulate the cloud more realistically at least in the number concentration of ice crystals, amplification of nucleation rates is necessary.

Sensitivity experiments to varying ice nucleation rates are conducted for three purposes: 1) to simulate the cloud more realistically at least in the number concentration of ice crystals; 2) to see the precipitation formation mechanism in the cloud; 3) to see the effects of changing various kinds of ice nucleation rates on precipitation formation. As shown in Table C-3-1, in these sensitivity experiments, parameters in various kinds of ice nucleation terms are modified to produce more cloud ice in number (EXDS for Fletcher's deposition/sorption nucleation; EXFZ for Bigg's cloud droplet freezing; EXHM for Hallet-Mossop's secondary

Table C-3-1 Kinds of sensitivity experiments to varying ice nucleation terms with $\alpha\Delta t = 32$ and $r_0 = 75 \mu\text{m}$ employed. Results are summarized in Table C-3-3.

	deposition /sorption Eq. B-(11-16) Fletcher $a \exp(-bT_c)$ $a = 10^{-2}$ $b = 0.6$	freezing Eq. B-(11-18) Bigg $c \exp(-dT_c)$ $c = 10^2$ $d = 0.66$	ice splinter Eq. B-(11-21) Hallet-Mossop T_1, T_2, T_3, T_4 $=(-3, -5, -5, -8)$	seeding	fracturing by collision between snow and graupel particles (Eq. C-(3-1)) $A = 0$
EXN1	normal	normal	normal	no	normal
EXDS1	$a \rightarrow \times 10^3$	normal	normal	no	normal
EXDS2	$a \rightarrow \times 10^6$	normal	normal	no	normal
EXFZ1	normal	$c \rightarrow \times 10^2$	normal	no	normal
EXFZ2	normal	$c \rightarrow \times 10^5$	normal	no	normal
EXHM	normal	normal	T_1, T_2, T_3, T_4 $=(-3, -5, -28, -30)$	no	normal
EXS1	normal	normal	normal	0.95–1.75km	normal
EXS2	normal	normal	normal	1.75–3.15km	normal
EXBK1	normal	normal	normal	no	10
EXBK2	normal	normal	normal	no	100

ice nucleation).

EXBK is conducted to see the effects of the secondary ice particle generation by collision between snow and graupel particles (Vardiman, 1978; Griggs and Choulaton, 1986) which is given as below:

$$\text{Nigacs} = A \times \text{Ngacs}, \quad (3-1)$$

where Ngacs is the number of collisions between snow and graupel particles per second and A is a coefficient. In EXBK1 and EXBK2, A is assumed to be 10 and 100, respectively.

EXDS1 is regarded as a reference experiment, simply because the number concentration of cloud ice and snow and radar reflectivity are closer to the observed values than EXN1.

To assess the seedability to convective clouds, seeding experiments are conducted by adding the ice nucleation term of

$$100 \times \text{Pidsn}, \quad (3-2)$$

with substitution of $w = 5\text{m/s}$ and $T_c = -20^\circ\text{C}$, during the first 60min at $0.95 \leq z \leq 1.75\text{km}$ (EXS1) or at $1.75 \leq z \leq 3.15\text{km}$ (EXS2) all over the horizontal domain. The total number

of added ice nuclei will amount to 4×10^{17} (equivalent to 400kg dry ice) if the seeded area is water-saturated everywhere.

Another kind of sensitivity experiment is conducted to see the effect of the parameters $\alpha 2\Delta t$ (see Eq. B-(11-43)) and r_0 (see Table B-11-1 and Eq. B-(11-27)) which have a large influence on the conversion term of snow into graupel and that of cloud ice to snow, respectively. Experiments except for those listed in Tables C-3-4 and C-3-5 adopt $\alpha 2\Delta t = 32$ and $r_0 = 75\mu\text{m}$, unless specifically mentioned.

Initial environmental conditions are determined from observations (see Figs. C-3-2 and C-3-5). The initial wind velocity component projected on the 100° azimuth plane, u , has no vertical shear below $z = 2.5\text{km}$, while it has a shear of $4 \times 10^{-3} \text{ s}^{-1}$ above $z = 2.5\text{km}$. The initial wind velocity component projected on the 10° azimuth plane, v , is set to zero. Time integration is continued up to 213min, during which 3 groups of clouds appears successively. The first cloud is initiated artificially by adding the warm and moist perturbation to the initial field at the central part of the domain. The second and third groups of clouds are excited at the convergence zone that resulted from the collision of the cold outflows.

C-3-5. Results of reference experiment (EXDS1)

a) Overview of the evolution of the convective clouds and the water budget analysis

Figure C-3-5 shows the horizontally averaged values for U (horizontal wind component in the x -direction), temperature, mixing ratio of water vapor, potential temperature, equivalent potential temperature, saturation equivalent potential temperature and relative humidity at $t = 60\text{min}$. The sea surface temperature is 10°C . Initially, the potential temperature at $z = 10\text{m}$ is 0°C , but it is warmed up to 2°C at $t = 60\text{min}$. Environmental vertical wind shear between $z = 10\text{m}$ and cloud top ($z = 2.5\text{km}$) has changed from 0 to 10^{-3}s^{-1} mainly due to the surface friction.

Figure C-3-6 shows the horizontally averaged values for Q_c , $\log(N_i)$, Q_s , $\log(N_s)$, Q_g and $\log(N_g)$ as a function of time and height. The heights of 0°C , -10°C and -20°C are 0.05km, 1.2km and 2.4km respectively. The height of cloud base is about 0.7km and the height of cloud top increases from 2.5km to 3km. The maximum values of Q_c and Q_g are seen at the middle level ($z = 1.5\text{km}$), while those of N_i and N_s are seen at the upper level ($z = 2.2\text{km}$).

Figure C-3-7a shows the time evolution of the cloud in terms of the maximum values of mixing ratios of water species in air, precipitation rates of snow and graupel, number

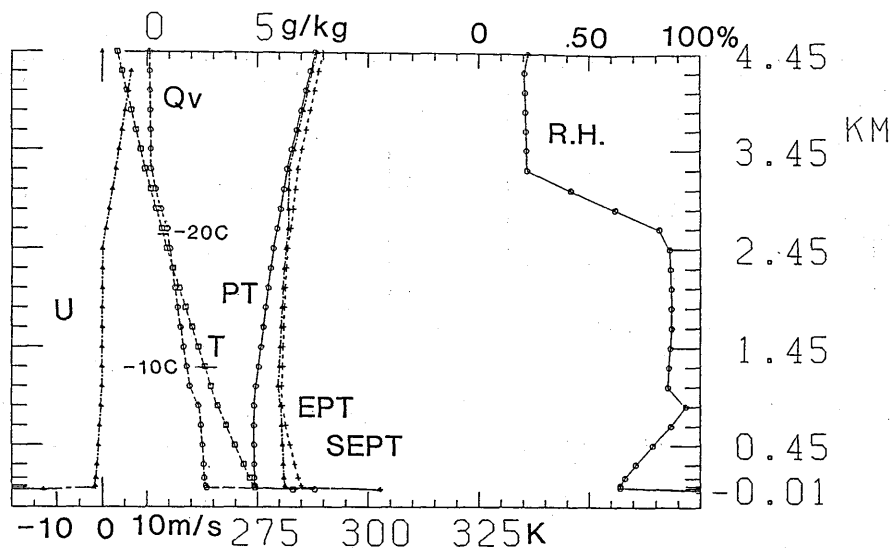


Fig. C-3-5 Horizontally averaged values for U (horizontal wind component in the x -direction), temperature, T , mixing ratio of water vapor, Q_v , potential temperature, PT , equivalent potential temperature, EPT , saturation equivalent potential temperature, $SEPT$, and relative humidity RH at $t = 60$ min by EXDS1.

concentration of cloud ice, snow and graupel and upward velocity, w , in the domain. Three maxima in upward velocity and cloud water appear at $t = 60$ min, 127min and 173min. The second and third maxima correspond to the newly generated clouds at the convergence zone where cold outflows from the older clouds collide. A similar initiation of convection by interacting outflows was simulated by Droegemeier and Wilhelmson (1985). About 13 ~ 20min later than the time when cloud water in air becomes maximum, graupel in air reaches its maximum, and about 20 ~ 27min later than the time when cloud water in air reaches its maximum, snow in air reaches its maximum. The life cycle of the simulated clouds is divided into 5 stages as shown in Table C-3-2.

Here, some useful quantities for water budget analysis are defined as follows:

Horizontally averaged and vertically integrated Q_x in air for the hydrometeor x (v , water vapor; c , cloud water; r , rain; i , cloud ice; s , snow; g , graupel).

$$TQ_x = \iiint \bar{\rho} Q_x dx dy dz / (LX \times LY) \quad (\text{kgm}^{-2});$$

Horizontally averaged and vertically integrated N_x in air,

$$TN_x = \iiint N_x dx dy dz / (LX \times LY) \quad (\text{m}^{-2});$$

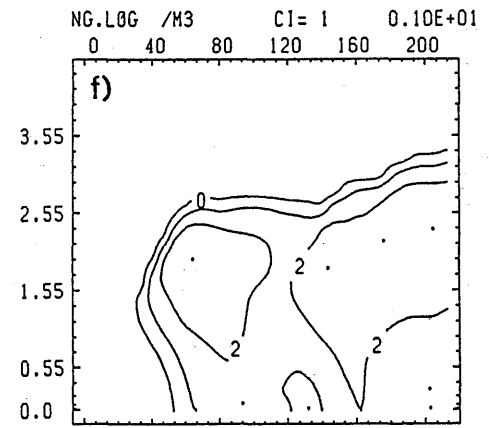
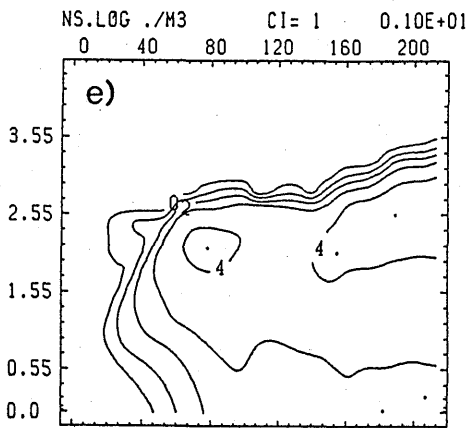
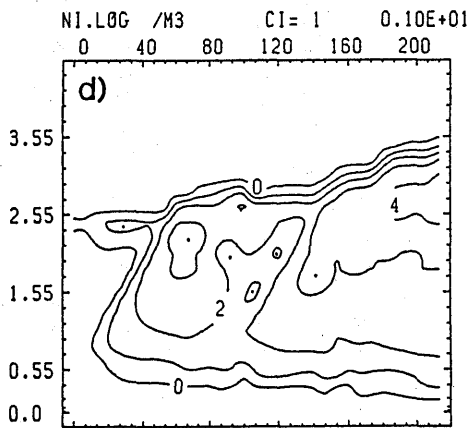
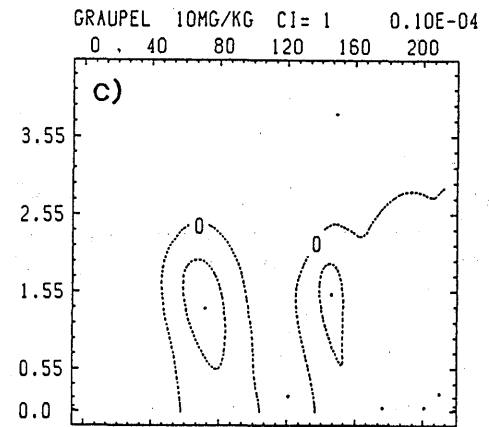
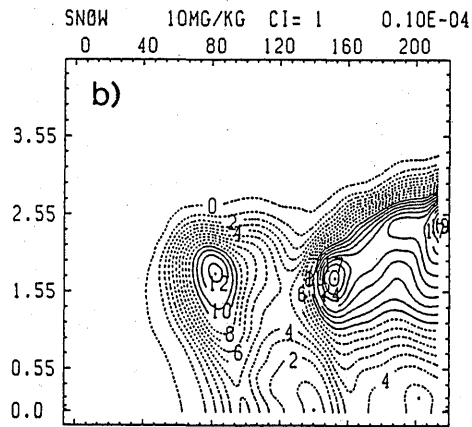
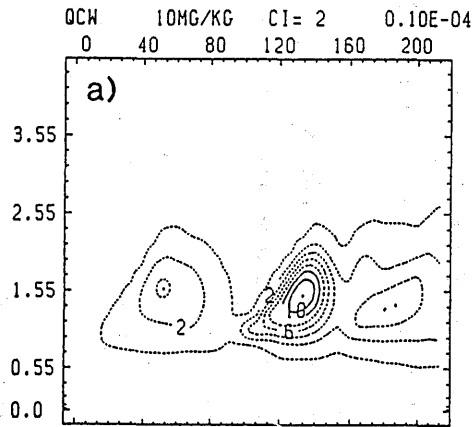


Fig. C-3-6 Horizontally averaged values by EXDS1 for (a) Q_c (10^{-5} kg/kg), (b) Q_s (10^{-5} kg/kg), (c) Q_g (10^{-5} kg/kg), (d) $\log_{10}(N_i)(N_i : m^{-3})$, (e) $\log_{10}(N_s)(N_s : m^{-3})$, and (f) $\log_{10}(N_g)(N_g : m^{-3})$ as a function of time and height. Contour intervals are indicated by "CI=nn".

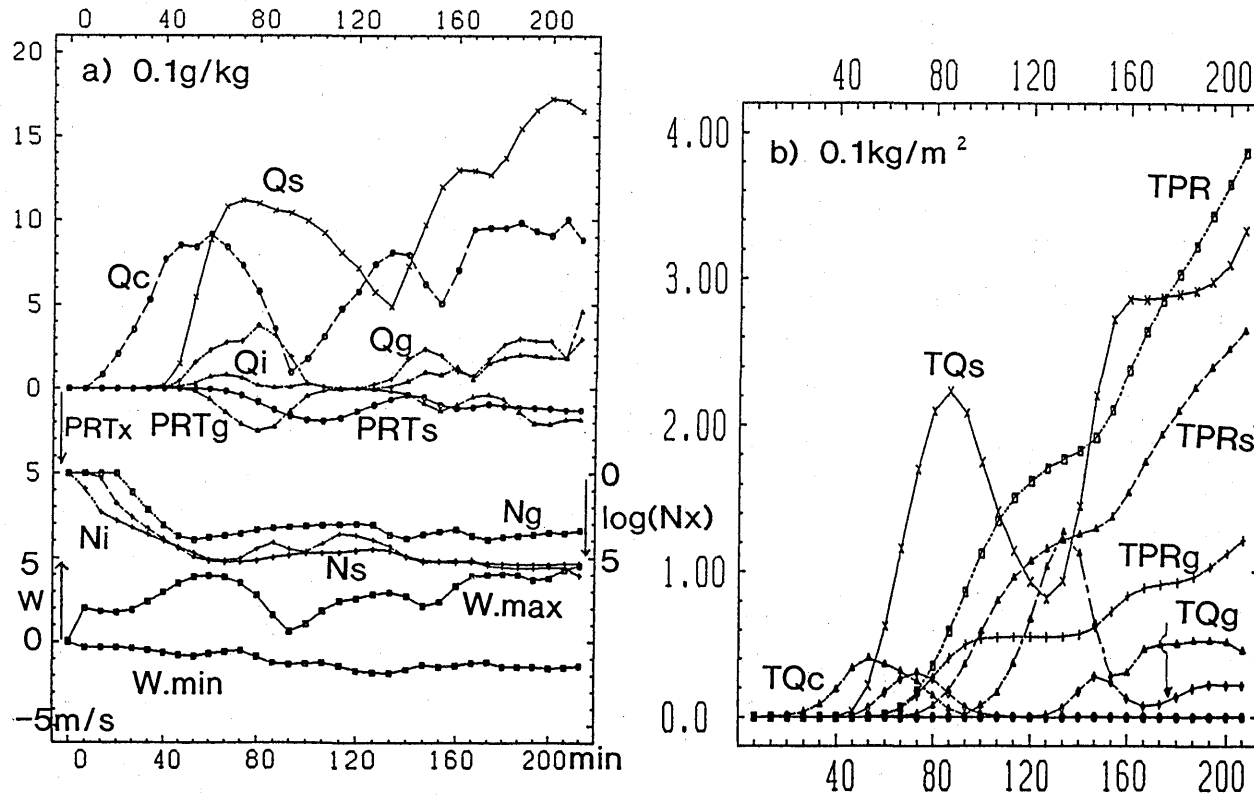


Fig. C-3-7 The results of EXDS1:

- a) The maxima of (upper part) Q_c (0.1 g/kg), Q_i (0.01 g/kg), Q_s (0.1 g/kg), Q_g (0.1 g/kg), and precipitation intensities (mm/hour) of snow and graupel, (central part) $\log_{10}(N_i)$, $\log_{10}(N_s)$, $\log_{10}(N_g)$, and (lower part) the maximum and minimum of the updraft w (m/s), as a function of time. N_i , N_s and N_g are the number concentrations of cloud ice, snow and graupel (m^{-3}), respectively. Data are sampled every 100 steps (6.67 min).
- b) TQ_c , TQ_s , TQ_g , TPR_s , TPR_g and $(TPR_s + TPR_g)$ (horizontally averaged vertically integrated quantities of Q_c , Q_s , Q_g and the horizontally averaged precipitation amounts of snow, graupel and (snow + graupel)) as a function of time. Unit is 0.1 kg/m^2 .

Table C-3-2 Life cycle of the convective clouds (the first group, 1; the second, 2) that appeared in EXDS1. The symbols $\uparrow \downarrow$ denote the time tendencies of increase and decrease, respectively. The symbols max and - denote the maximum and minimum values. Stages 1 and 2 might be called formative and developing stages, respectively; stages 3 and 4 mature and decaying stages; stage 5 a decayed stage.

stage	W	Qc	Qg	PRCP.g	Qs	PRCP.s	time (min)	
							1	2
1	\uparrow	\uparrow	0	0	0 (-)	0 (\downarrow)	20	107
2	max	max	\uparrow	0	\uparrow	0 (-)	60	134
3	\downarrow	\downarrow	max	\uparrow	\uparrow	\uparrow	80	147
4	- \downarrow	- \downarrow	\downarrow	max	max	\uparrow	80	160
5	\uparrow	\uparrow	-	\downarrow	\downarrow	max	100	167

Horizontally averaged and vertically integrated mass production term for the elementary cloud microphysical process Pxqqq,

$$TPxqqq(z_0 < z < z_1) = \int_{z_0}^{z_1} \iint \bar{\rho} Pxqqq dx dy dz / (LX \times LY) \quad (\text{kgm}^{-2}\text{s}^{-1});$$

Horizontally averaged and vertically integrated number production term for the elementary cloud microphysical process Nxqqq,

$$TNxqqq(z_0 < z < z_1) = \int_{z_0}^{z_1} \iint Nxqqq dx dy dz / (LX \times LY) \quad (\text{m}^{-2}\text{s}^{-1});$$

Horizontally averaged and vertically integrated total mass production term for the hydrometeor, x,

$$TPRD(Q_x) = \int_0^{z_1} \iint \bar{\rho} PRD(x) dx dy dz / (LX \times LY) \quad (\text{kgm}^{-2}\text{s}^{-1});$$

Horizontally averaged and vertically integrated total number production term for the hydrometeor, x,

$$TPNx = \int_0^{z_1} \iint NPRD(x) dx dy dz / (LX \times LY) \quad (\text{m}^{-2}\text{s}^{-1});$$

Horizontally averaged precipitation rate of x,

$$PRCPx = \int \int \bar{\rho} Qx \bar{U}x dx dy / (LX \times LY) \quad (\text{kgm}^{-2}\text{s}^{-1});$$

Horizontally averaged accumulated precipitation amount of x,

$$TPRx(t_1, t_2) = \int_{t_1}^{t_2} PRCPx dt \quad (\text{kgm}^{-2});$$

Horizontally averaged total precipitation amount,

$$TPR(t_1, t_2) = TPRr(t_1, t_2) + TPRs(t_1, t_2) + TPRg(t_1, t_2).$$

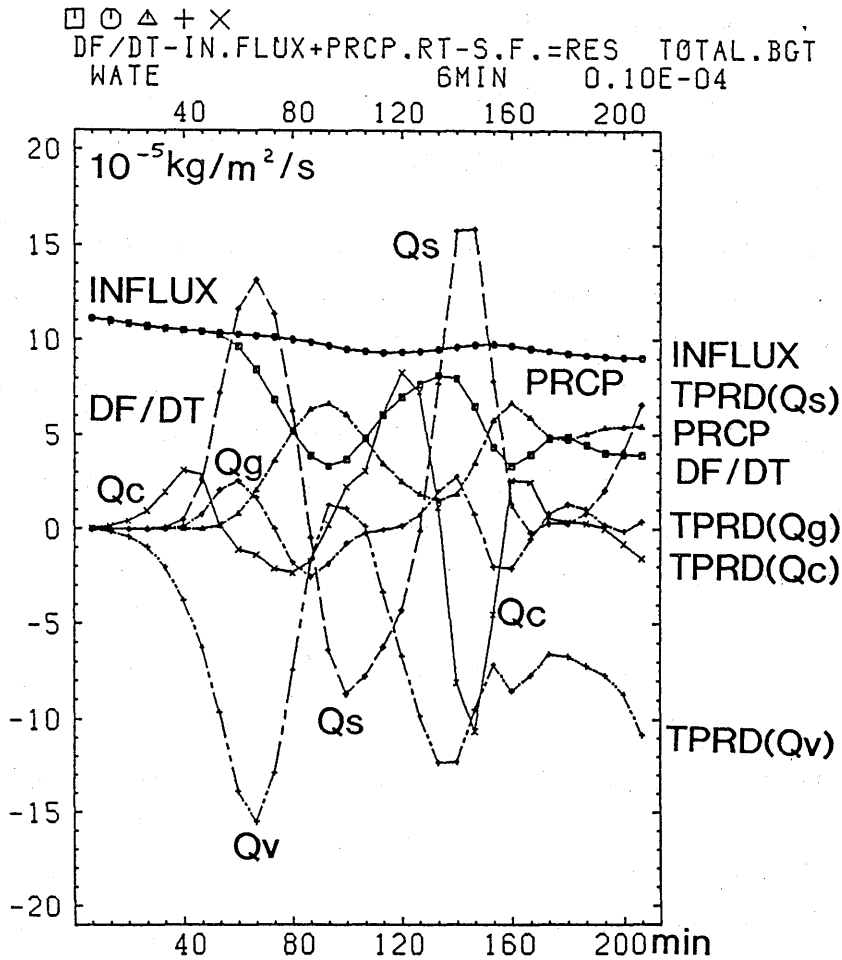


Fig. C-3-8 Water budget analysis for EXDS1. DF/DT , $INFLUX$, $PRCP$ ($10^{-5} \text{ kg/m}^2/\text{s}$) are shown as a function of time, together with $TPRD(Qv)$, $TPRD(Qs)$, $TPRD(Qg)$. Data are sampled every 100 steps (6.67 min).

Figure C-3-7b shows the time variations of TQc , TQs , TQg , $TPRs$, $TPRg$ and TPR .

Figure C-3-8 shows the water budget of the simulated cloud together with $TPRD(Qv)$, $TPRD(Qc)$, $TPRD(Qs)$ and $TPRD(Qg)$. The water budget equation is given as:

$$\frac{\partial F}{\partial t} - INFLUX + PRCP = RES,$$

where

$$F = TQv + TQc + TQr + TQi + TQs + TQg$$

$$PRCP = PRCP_r + PRCP_s + PRCP_g,$$

$$INFLUX = \iint \overline{\rho Q v'' w''} dx dy / (LX \times LY) \quad (\text{kgm}^{-2}\text{s}^{-1})$$

(the water vapor flux from the sea surface).

RES is a residual term, which should be zero if artificial diffusion terms and computational errors are absent. RES is below $10^{-6}\text{kgm}^{-2}\text{s}^{-1}$ (not shown in Fig. C-3-8). The water vapor flux from the sea surface is nearly constant ($1 \times 10^{-4}\text{kgm}^{-2}\text{s}^{-1}$ or 260Wm^{-2}). From the heat budget analysis (not shown here), the heating of the air due to the sensible heat supply is about 175Wm^{-2} ; that due to the cloud microphysical processes varies roughly in accord with $-Hv \times TPRD(Qv)$ (Hv , latent heat of vaporization); its maximum is about 450Wm^{-2} at $t = 67\text{min}$ and 140min ; the minimum is about -50Wm^{-2} at $t = 93\text{min}$.

The precipitation efficiency defined as

$$PRCP.EF(t_1, t_2) = \frac{TPR(t_1, t_2)}{\int_{t_1}^{t_2} INFLUX dt}$$

is about 0.3 for $(t_1, t_2) = (0\text{min}, 213\text{min})$ and 0.45 for $(t_1, t_2) = (120\text{min}, 213\text{min})$.

b) Individual fields at various stages of the cloud

Figures C-3-9, C-3-10 and C-3-11 show the cross sections of various fields at the developing to mature stage ($t = 60\text{min}$) of the first cloud, the mature to decaying stage ($t = 80\text{min}$) and the decayed stage of the first cloud and the formative stage of the newly excited cloud ($t = 120\text{min}$). Radar reflectivity is computed by use of Eq. 54 in Murakami (1990). The strong cold outflow at the decayed stage shown in Fig. C-3-11 b) is attributed to cooling by sublimation from snow. Figures C-3-9 k), l), C-3-10 k), l) and C-3-11 j) show the intercept parameter of the inverse exponential size distribution function, Nos and Nog . It is noticed that Nos and Nog are not constant but increase as the cloud evolves from the developing to the decaying stage. Nos at the upper and flanking parts tends to be large, suggesting the existence of a large number of small snow particles. The location of the maximum of Qs near the surface does not coincide with that of the maximum of Nos at $t = 80\text{min}$, while that of Qs coincides with that of Nos at $t = 120\text{min}$.

Figure C-3-12 shows the accumulated precipitation patterns of snow and graupel at 213min. Precipitation of graupel is more concentrated than that of snow. Precipitation

around $(x, y) = (4\text{km}, 0\text{km})$ is brought about by the second and third groups of clouds.

c) Cloud microphysical processes and precipitation formation

Figure C-3-13b shows the horizontally averaged values of Q_c , Q_s , Q_g , N_i , N_s and N_g at $t = 60\text{min}$ as a function of height. Figures C-3-13 a, c and d show the dominant processes which are horizontally averaged values as a function of height at $t = 60\text{min}$ relating to the production terms of cloud ice, snow and graupel, respectively. The figures corresponding to Fig. C-3-13 at $t = 80, 100$ and 120min are displayed in Fig. C-3-14, C-3-15 and C-3-16, respectively.

Figure C-3-17 shows the dominant mass production terms in forming snow and graupel as a function of time. Figure C-3-18 shows the mass production terms involving cloud ice. Cloud ice (pristine ice crystals) is generated mainly via deposition/sorption nucleation (P_{idsn}), and freezing of cloud droplets is $1/100$ of P_{idsn} . Cloud ice grows mainly via depositional growth (P_{idep}), and finally is turned into snow (P_{icns}). Depositional growth of cloud ice (P_{idep}) nearly balances the conversion term of cloud ice into snow (P_{icns}).

The number generation of snow is via conversion of cloud ice into snow (N_{icns}). The number of snow after mature stage decreases via aggregation (N_{sag}), precipitation (N_{sprc}) and sublimation. The number generation of graupel is via conversion of snow into graupel (N_{scng}) which is $1/100$ of N_{icns} .

Precipitation formation is summarized as shown in Fig. C-3-19:

- i) At the developing or mature stage (the stage 2-3; Fig. C-3-19a) of the cloud, the water vapor supplied from the warm sea surface condenses to form supercooled cloud water. Cloud ice grows into snow via depositional process. Snow grows via riming and depositional processes. Graupel grows primarily via riming process and secondarily via depositional process.
- ii) At the mature or decaying stage (the stage 3-4; Fig. C-3-19b), cloud water is almost depleted; above the cloud base, depositional growth of ice particles is more dominant than riming growth; the precipitation rate of ice particles is large, and the amount of sublimation below the cloud base is roughly $1/3 \sim 1/2$ of the amount of deposition above it.
- iii) At the decayed stage (the stage 5; Fig. C-3-19c), cloud water is almost depleted and no graupel particles are found and precipitation of graupel ceases; the amount of snow continues

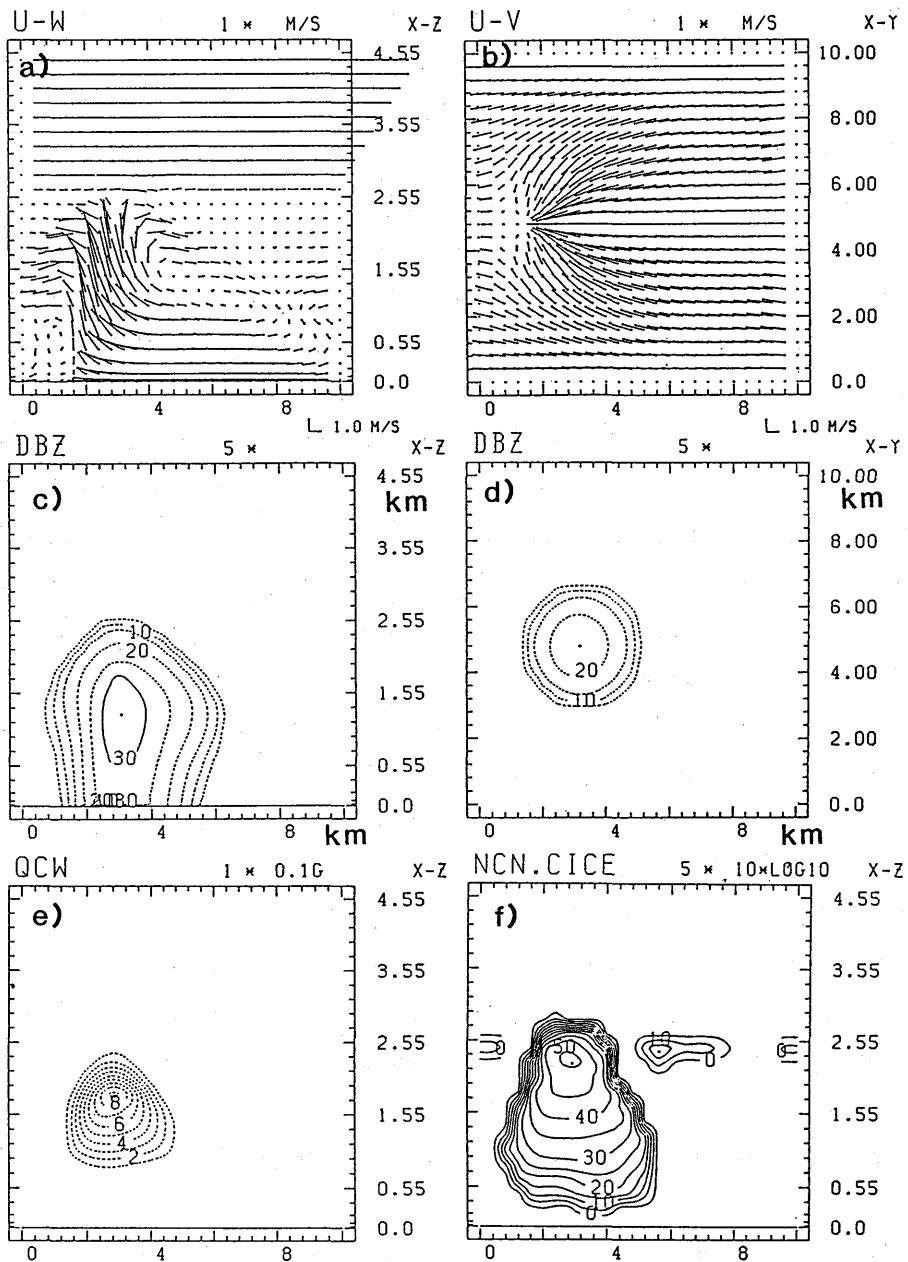


Fig. C-3-9 The cross sections of various fields at $t = 60$ min (the developing to mature stage of the first cloud) by EXDS1.

- a) X - z cross section of the u - w wind vector field at $y = 4.8$ km.
- b) X - y cross section of the u - v wind vector field at $z = 0.03$ km.
- c) X - z cross section of the radar reflectivity dBZ at $y = 4.8$ km with contour intervals of 5 dBZ.
- d) X - y cross section of the radar reflectivity dBZ at $z = 2.05$ km with contour intervals of 5 dBZ.
- e) X - z cross section of Q_c at $y = 4.8$ km with contour intervals of 0.1 g/kg.
- f) X - z cross section of $10 \times \log_{10}(Ni)$ at $y = 4.8$ km with contour intervals of 5. The unit of Ni is m^{-3} .

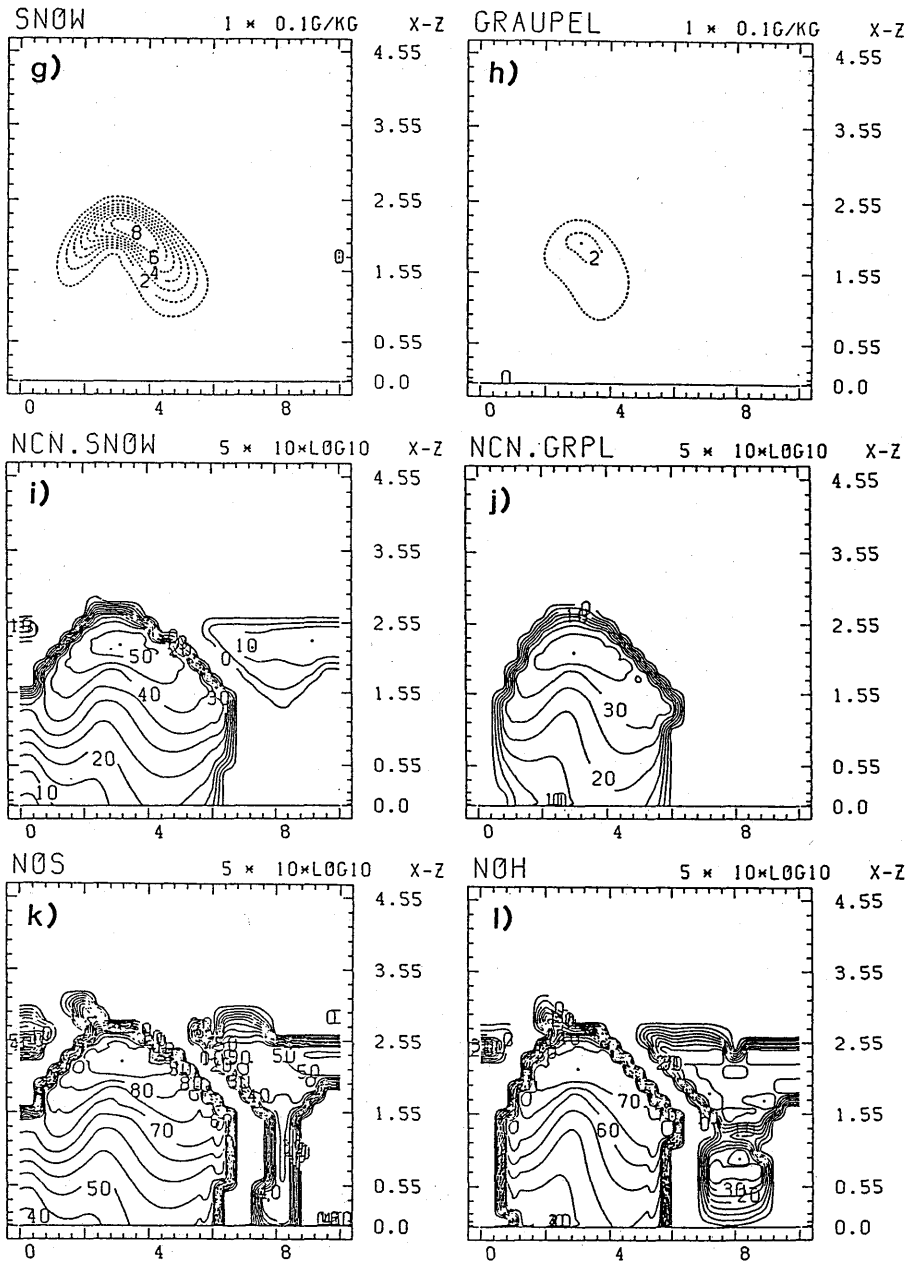


Fig. C-3-9 (Continued.)

- g) The same as e), but for Q_s .
- h) The same as e), but for Q_g .
- i) The same as f), but for N_s .
- j) The same as f), but for N_g .
- k) X-z cross section of $10 \times \log_{10}(N_{os})$ at $y = 4.8$ km with contour intervals of 5. The unit of N_{os} is m^{-4} .
- l) The same as k), but for N_{oh} .

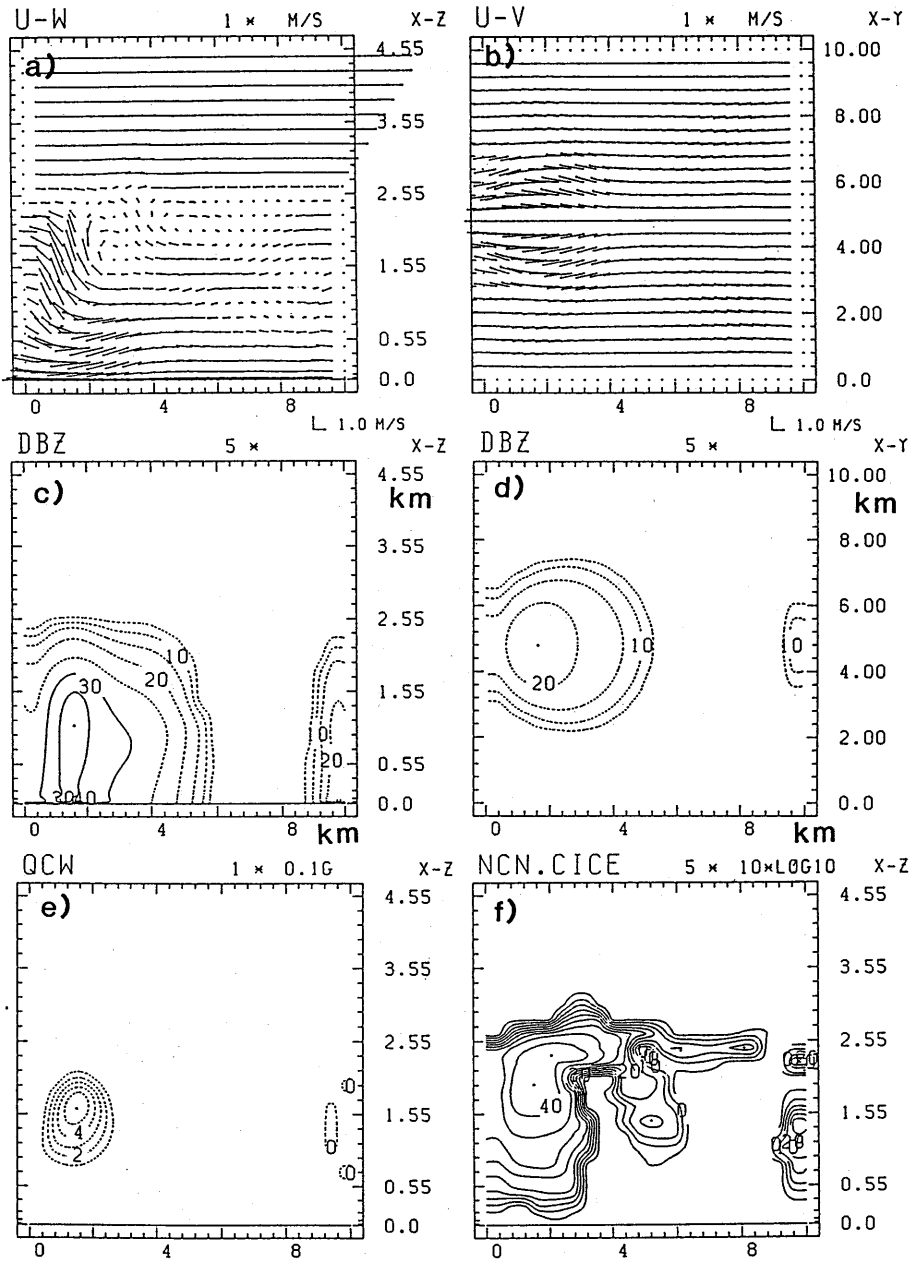


Fig. C-3-10 The same as Fig. C-3-9, but for $t = 80 \text{ min.}$

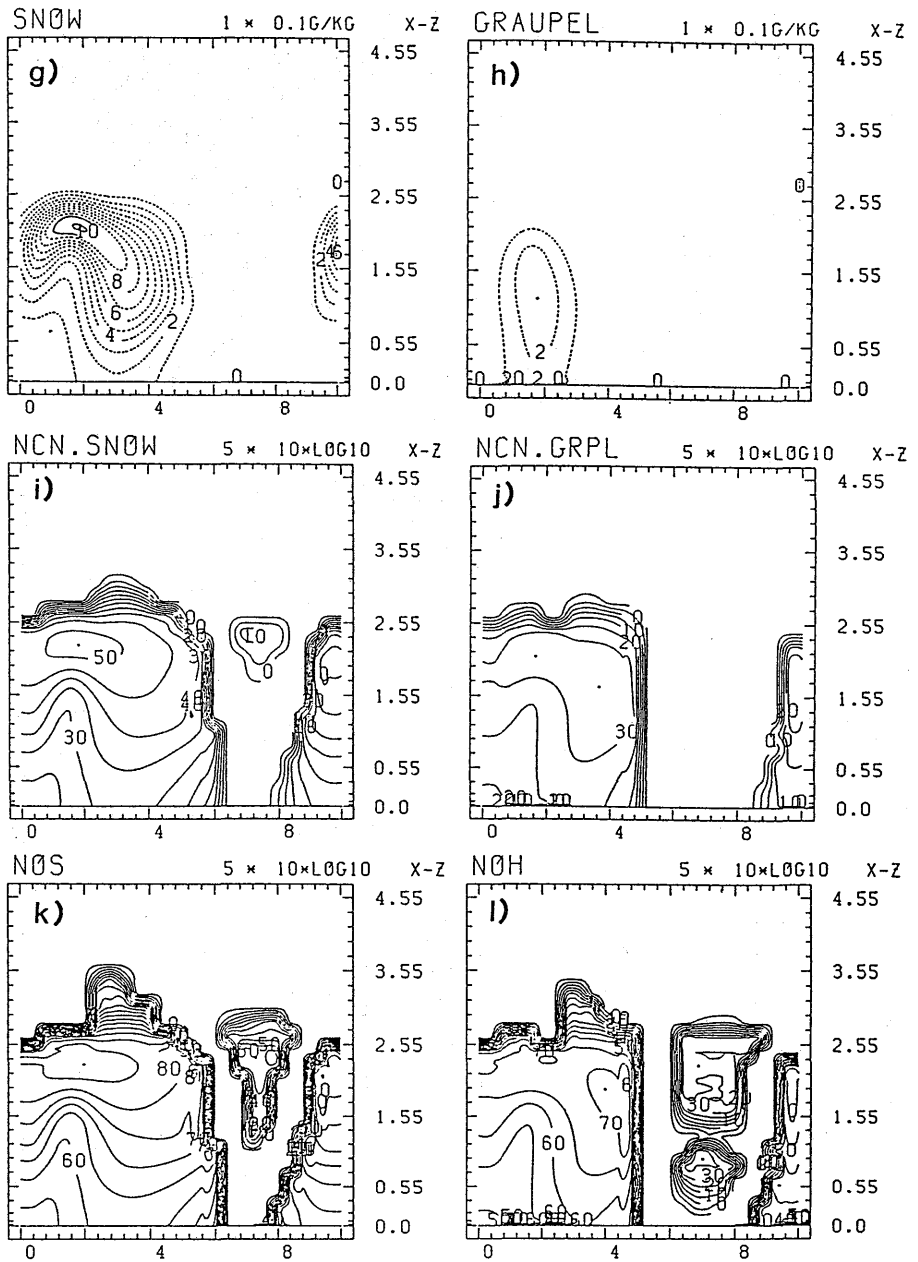


Fig. C-3-10 (Continued.)

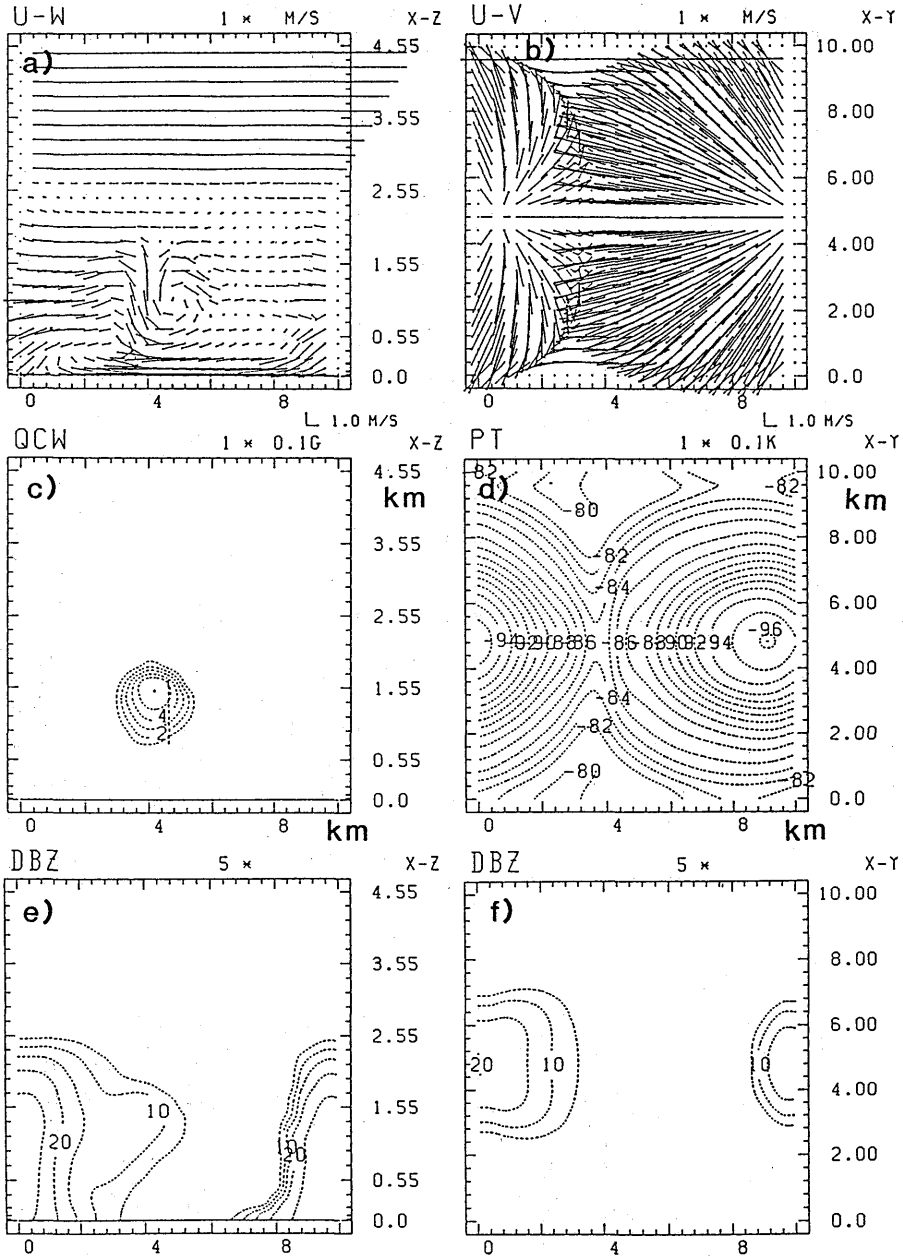


Fig. C-3-11 The cross sections of various fields at $t = 120$ min (the decayed stage of the first cloud and the formative stage of the newly excited cloud) by EXDS1.

- a) X-z cross section of the $u-w$ wind vector field at $y = 4.8$ km.
- b) X-y cross section of the $u-v$ wind vector field at $z = 0.03$ km.
- c) X-z cross section of Q_c at $y = 4.8$ km with contour intervals of 0.1 g/kg.
- d) X-y cross section of the deviation of the potential temperature from its reference field at $z = 0.03$ km. The unit is $0.1K$, with contour intervals of $0.1K$.
- e) X-z cross section of the radar reflectivity dBZ at $y = 4.8$ km with contour intervals of 5 dBZ.
- f) X-y cross section of the radar reflectivity dBZ at $z = 2.05$ with contour intervals of 5 dBZ.

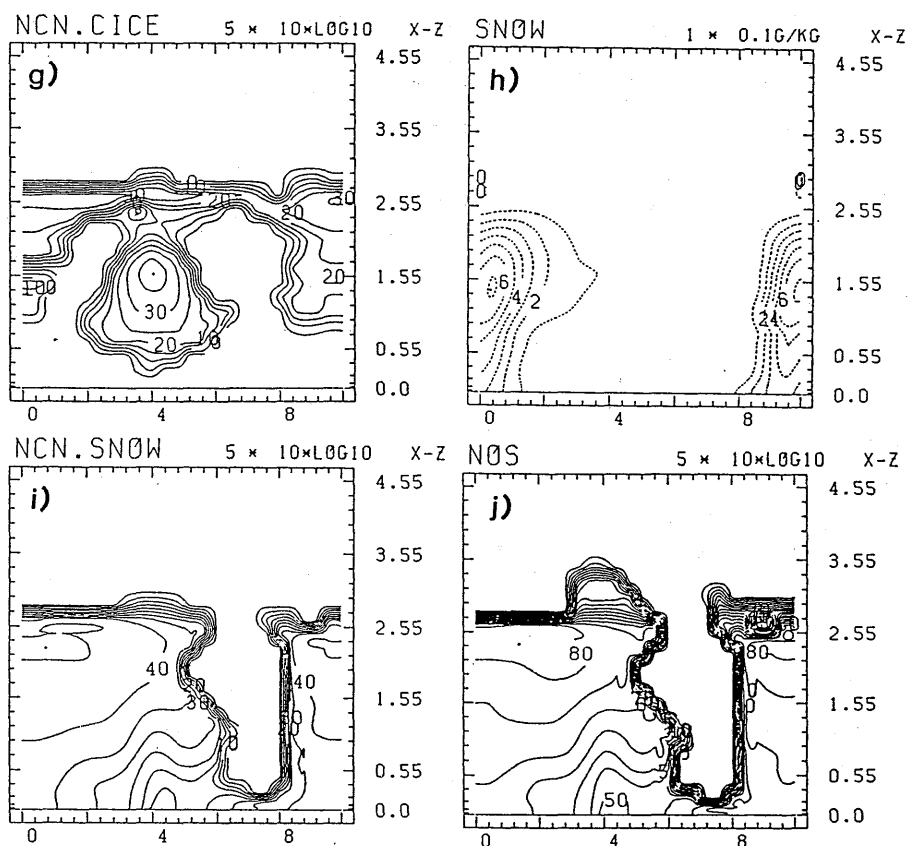


Fig. C-3-11 (Continued.)

- g) X-z cross section of $10 \times \log_{10}(Ni)$ at $y = 4.8$ km with contour intervals of 5. The unit of Ni is m^{-3} .
- h) The same as c), but for Qs .
- i) The same as g), but for Ns .
- j) X-z cross section of $10 \times \log_{10}(Nos)$ at $y = 4.8$ km with contour intervals of 5. The unit of Nos is m^{-4} .

to decrease due to the precipitation and sublimation below the cloud base; the amount of sublimation below the cloud base is greater than the amount of deposition above it. The number of snow particles decreases via aggregation, precipitation and sublimation.

C-3-6. Sensitivity experiments

a) Sensitivity to various ice nucleation terms

Results are summarized in Table C-3-3. The figures of EXN1, EXDS2, EXHM, EXBK1, EXBK2, EXS1 corresponding to Fig. C-3-7 of EXDS1 are shown in Figs. C-3-20, C-3-24, C-3-

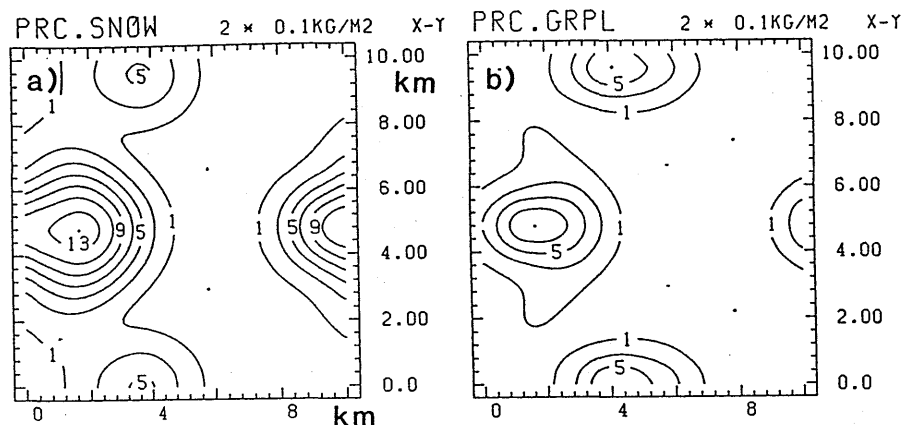


Fig. C-3-12 a) Total accumulated precipitation field of snow at $t = 213$ min by EXDS1. The unit is 0.1 kg/m^2 , and the contour interval is 0.2 kg/m^2 .
 b) The same as a) but for graupel.

27, C-3-30, C-3-31, C-3-32, respectively. The figures of EXN1, EXDS2, EXHM corresponding to Figs. C-3-17 and C-3-18 of EXDS1 are shown in Figs. C-3-21, C-3-22, C-3-25, C-3-26, C-3-28, C-3-29, respectively.

a-1) EXN1

As shown in Table C-3-3 and Fig. C-3-23, number concentration of ice particles is 1-order smaller than that of EXDS1. The maximum value of number concentration of ice particles is $1/4$ of the observed counterpart. The dominant generation term of cloud ice is not deposition/sorption nucleation (Pidsn, Nidsn) but freezing of cloud droplets (Pifzc, Nifzc) as shown in Fig. C-3-21b and C-3-22.

It is an interesting discovery that the conventional term of deposition/sorption nucleation by Fletcher is incapable of explaining the high number concentration of ice crystals in the observed cloud, while freezing of cloud droplets can produce fairly large number concentration of ice particles which is still smaller than the observed one but appears to be in a tolerable range.

In Fig. C-3-23, x - z cross sections of number concentrations of snow and graupel and radar reflectivity at $t = 80$ min in EXN1 are shown. The maximum of radar reflectivity in EXN1 is about 40dBZ, which is larger by 10dBZ than the observed value. Z (see Eq. 54 in Murakami, 1990) is approximated as

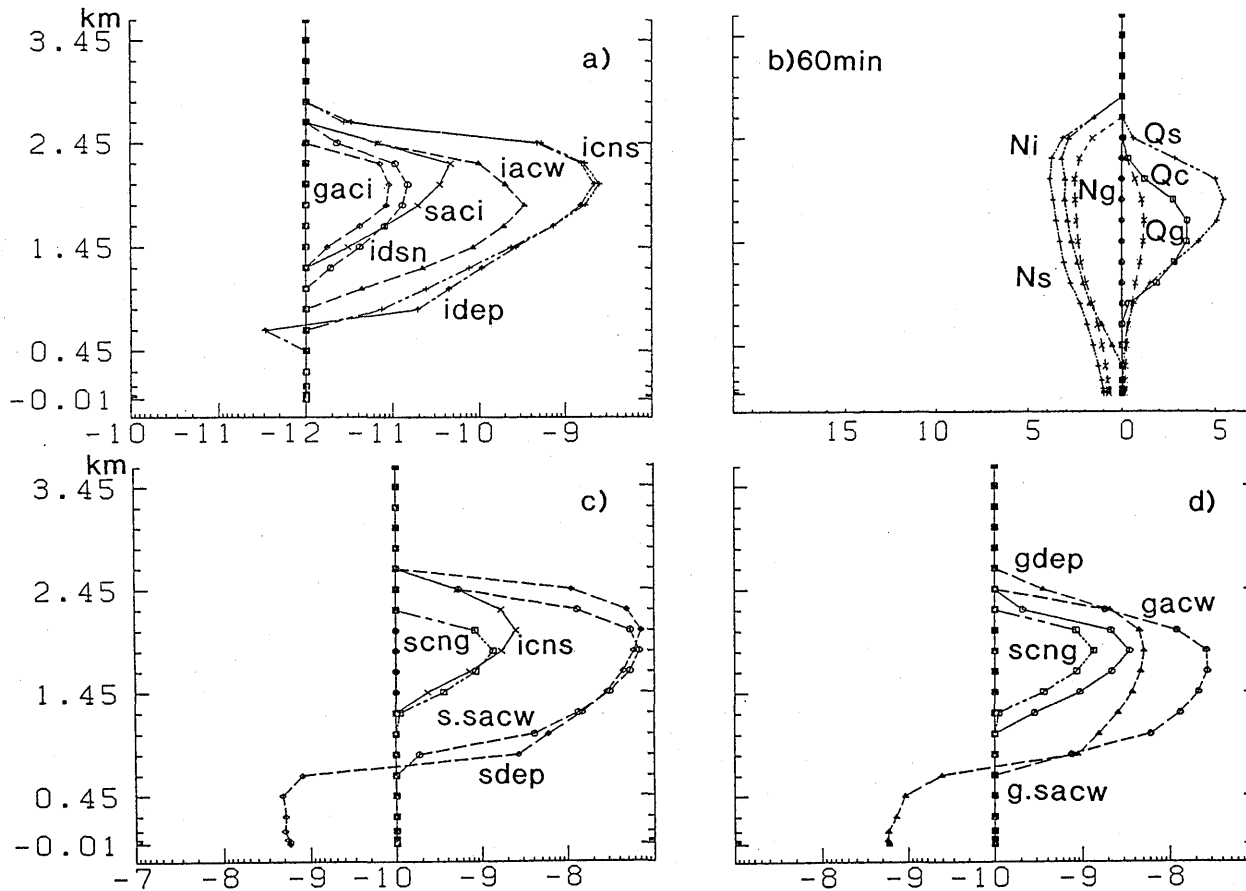


Fig. C-3-13 a) The dominant cloud microphysical processes (P_{xqqq} ; unit = s^{-1}) which are horizontally averaged values as a function of height at $t = 60$ min relating to cloud ice by EXDS1. For $P_{xqqq} > p_0 = 10^{-12} s^{-1}$, $\log_{10}(P_{xqqq})$ is plotted in the right side. For $P_{xqqq} < -p_0$, $\log_{10}(-P_{xqqq})$ is plotted in the left side. b) The horizontally averaged values of Q_c , Q_s , Q_g (right side: unit $10^{-5} kg/kg$), N_i , N_s and N_g (left side: unit m^{-3} , expressed in $\log_{10}(Nx)$) at $t = 60$ min as a function of height by EXDS1. c) The same as a) but for snow and $p_0 = 10^{-10} s^{-1}$. d) The same as a) but for graupel and $p_0 = 10^{-10} s^{-1}$.

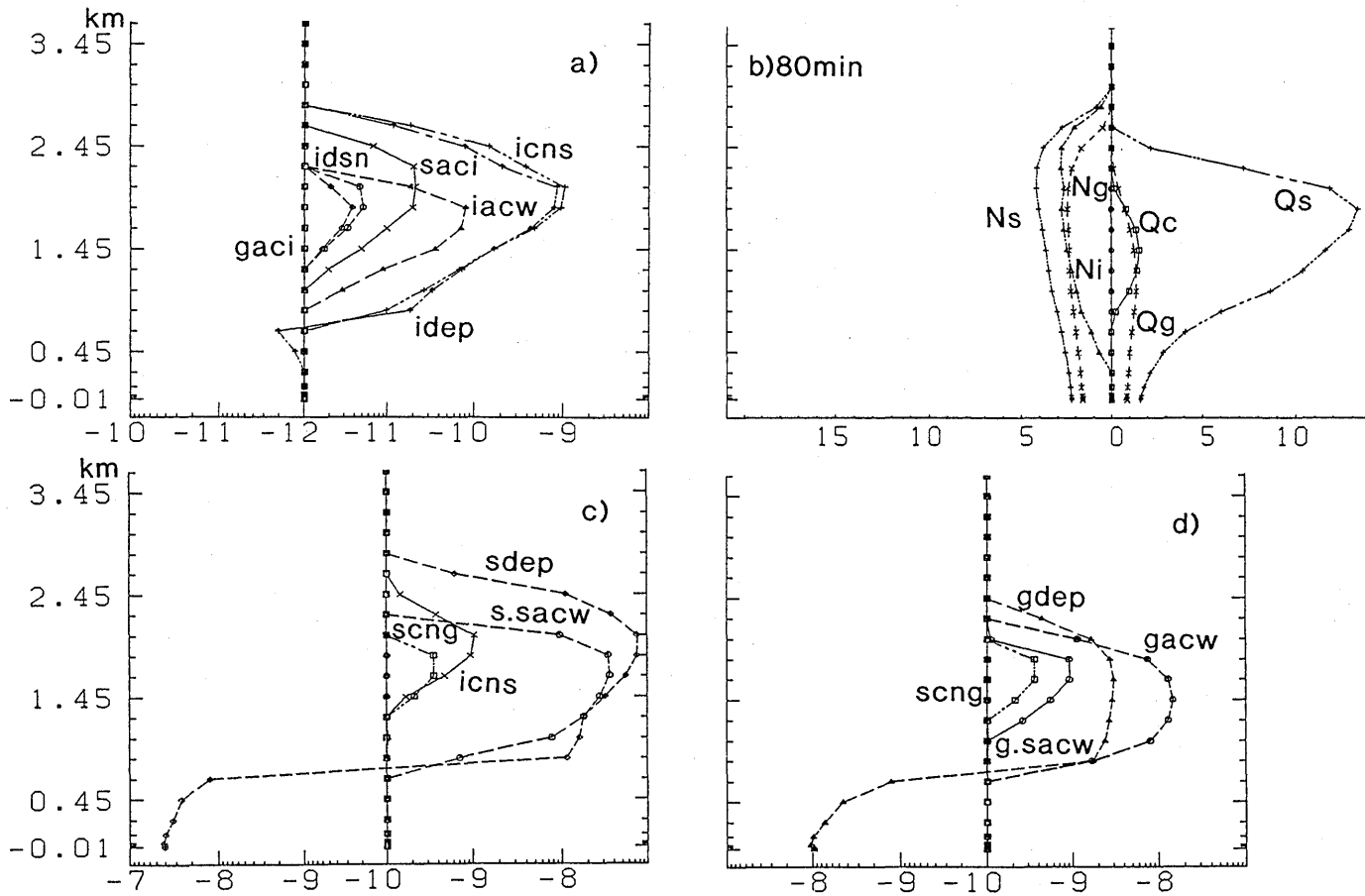


Fig. C-3-14 The same as Fig. C-3-13 but for $t = 80$ min.

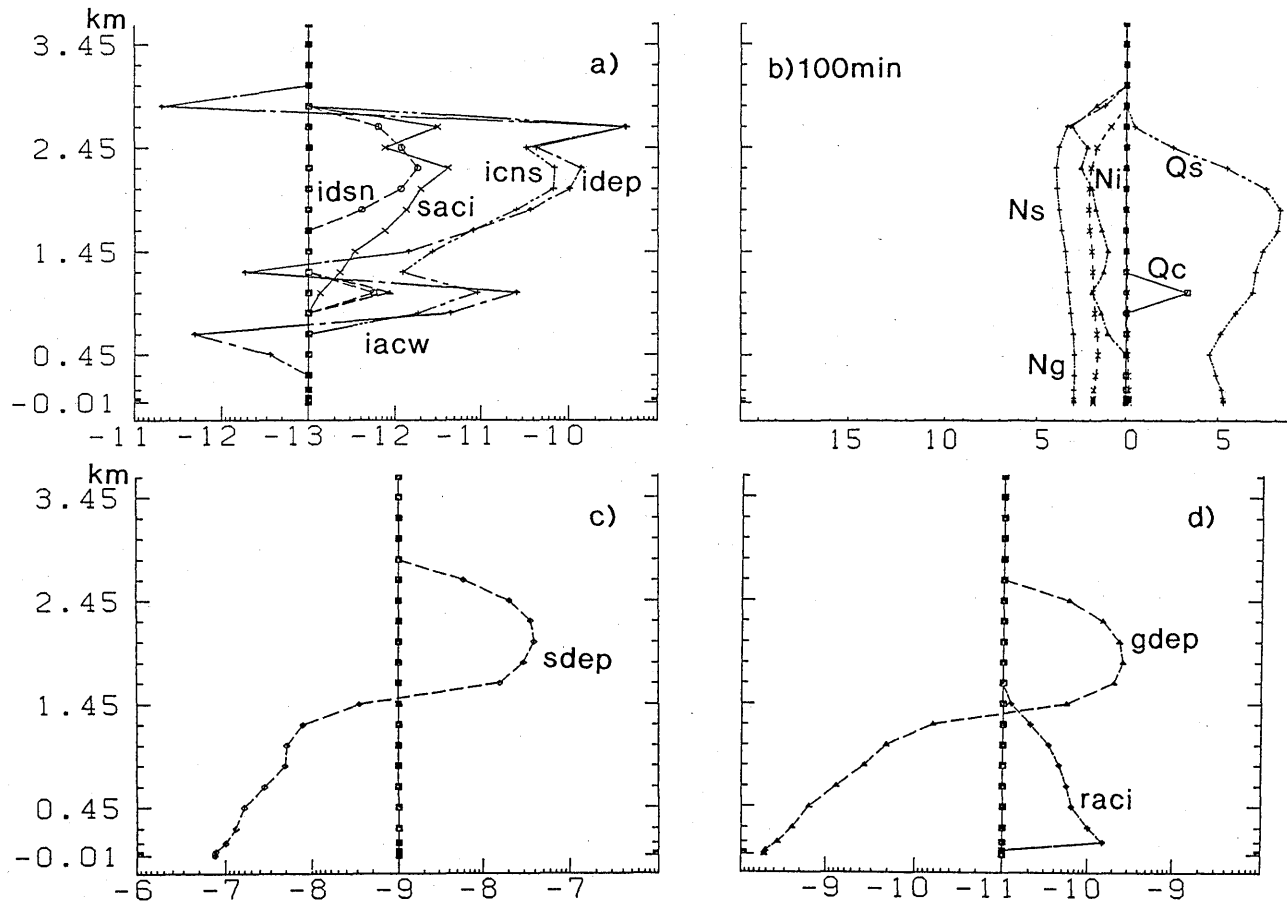


Fig. C-3-15 The same as Fig. C-3-13 but for $t = 100$ min. $p_0 = 10^{-13}, 10^{-9}, 10^{-11} s^{-1}$ are used for a), c) and d), respectively.

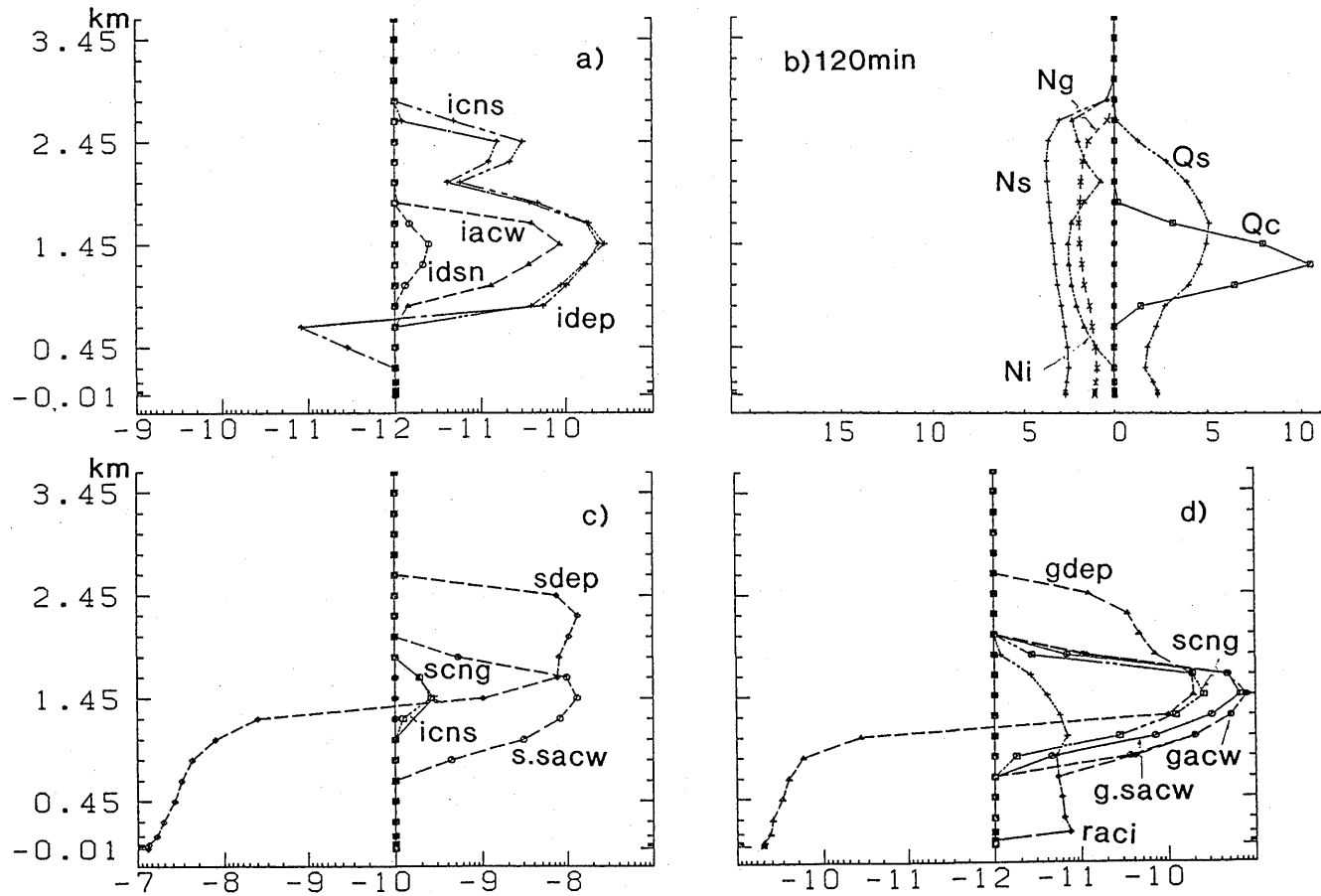


Fig. C-3-16 The same as Fig. C-3-13 but for $t = 120$ min. $p_0 = 10^{-12}, 10^{-10}, 10^{-12} \text{ s}^{-1}$ are used for a), c) and d), respectively.

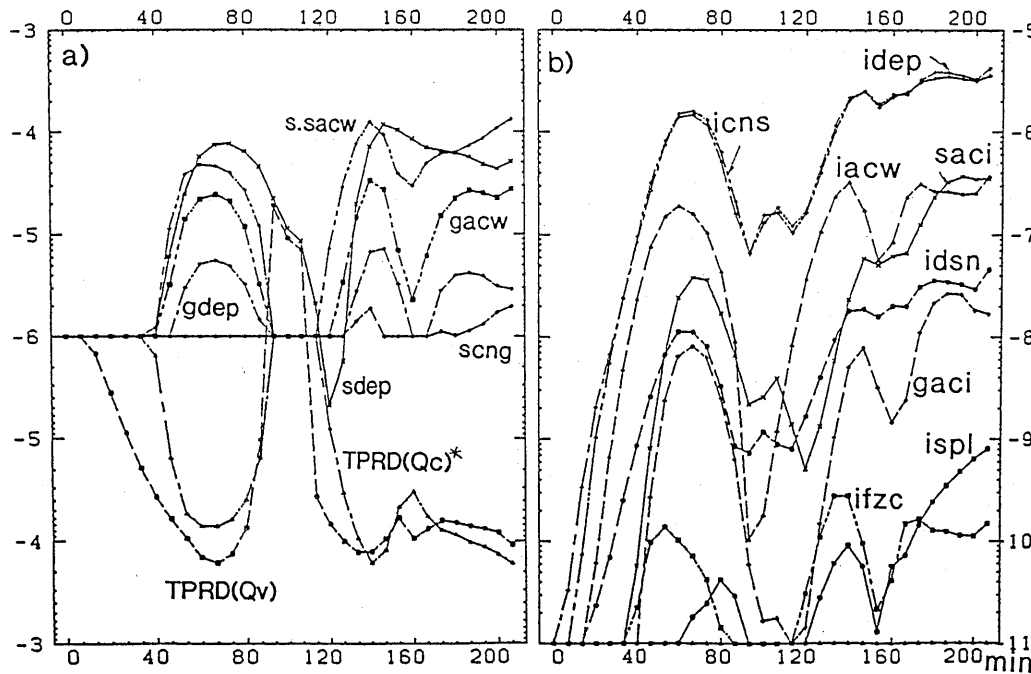


Fig. C-3-17 a) The dominant mass production terms ($TPxqqq: \text{kgm}^{-2}\text{s}^{-1}$) in forming snow and graupel as a function of time by EXDS1. $TPRD(Qc)* \equiv TPRD(Qc) - TPccnd$. For positive value $TPxqqq > 10^{-6}$, $\log_{10}(TPxqqq)$ is drawn in the upper part of the figure. For negative values $TPxqqq < -10^{-6}$, $-\log_{10}(-TPxqqq)$ is drawn in the lower part of the figure. For $-10^{-6} < TPxqqq < 10^{-6}$, values are plotted on the horizontal line indicated by -6 on the ordinate.
 b) The dominant mass production terms ($TPxqqq: \text{kgm}^{-2}\text{s}^{-1}$; expressed in $\log_{10}(TPxqqq)$) involving cloud ice as a function of time by EXDS1.

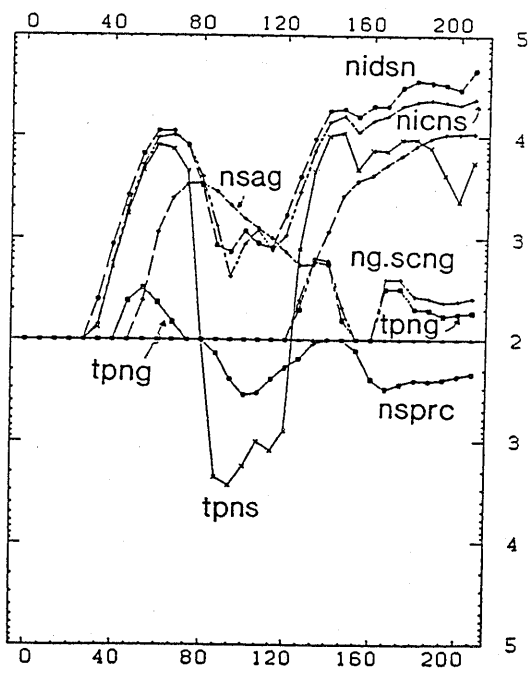


Fig. C-3-18 The dominant number production terms ($TNxqqq: \text{m}^{-2}\text{s}^{-1}$) in forming cloud ice, snow and graupel as a function of time by EXDS1. For positive values $TNxqqq > p_0 = 10^2$, $\log_{10}(TNxqqq)$ is drawn in the upper part of the figure. For negative values $TNxqqq < -p_0$, $-\log_{10}(-TNxqqq)$ is drawn in the lower part of the figure. For $-p_0 < TNxqqq < p_0$, values are plotted on the horizontal line indicated by 2 on the ordinate.

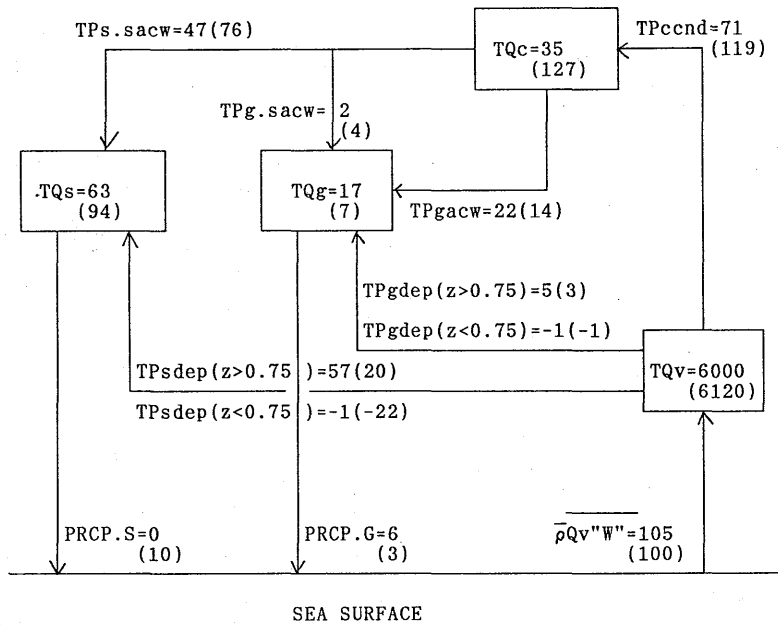


Fig. C-3-19a Dominant mass production terms in precipitation formation by EXDS1 at $t = 60$ min and $t = 133$ min (denoted by bracket)(a developing or mature stage). The unit for TQv , TQc , TQs and TQg is g/m^2 , and the unit for $TPccnd$, $TPs.sacw$ $PRCP.s$ is $10^{-3} g/m^2/s$.

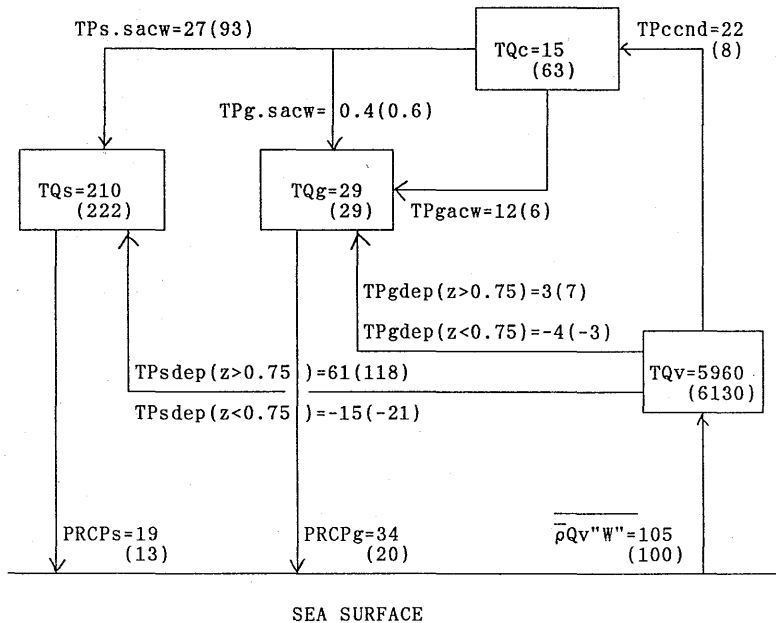


Fig. C-3-19b The same as Fig. C-3-19a, but for $t = 80$ min and $t = 147$ min (denoted by bracket)(a mature or decaying stage).

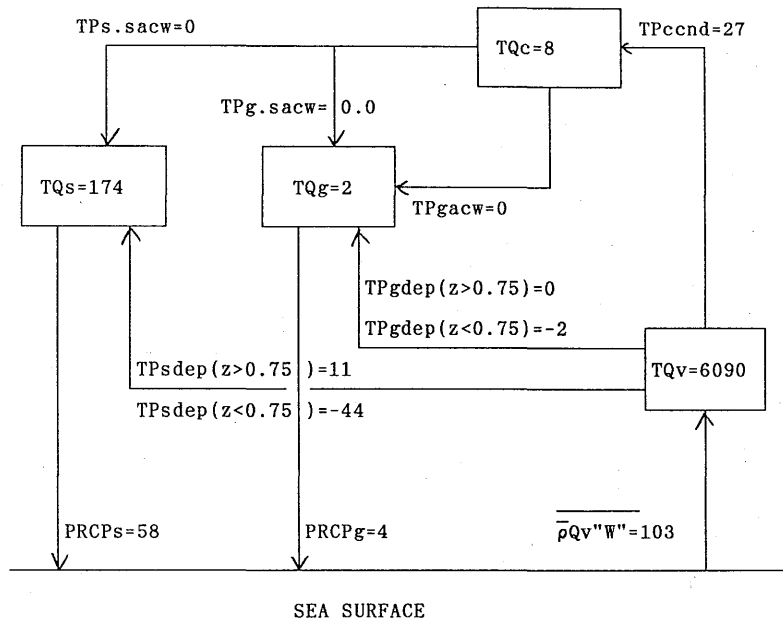


Fig. C-3-19c The same as Fig. C-3-19a, but for $t = 100$ min (a decayed stage).

$$Z = \sum D^6 \simeq N \left(\frac{\rho Q}{N} \right)^2 \propto N^{-1}$$

Therefore, this difference is partly attributable to the low ice nucleation rates and resultant low number concentrations of cloud ice and snow in EXN1.

In EXN1, Q_c exceeds the threshold value ($Q_{co} = 10^{-3}$) for the conversion of cloud water into rain which is given as

$$P_{ccnr} = 10^{-3}(Q_c - Q_{co}),$$

and rain is generated. However, the amount of rain is small; the generation term of graupel via collision between ice particles and rain (P_{iacr} , $P_{g.sacr}$) and freezing of rain (P_{gfzr}) is smaller than P_{scng} (at most $1/4$ of P_{scng}); the most dominant term of graupel generation is still P_{scng} ; the growth of snow and graupel by accretion of rain is still less than P_{sacw} and P_{gacw} . Therefore, rain does not play a dominant role in precipitation formation.

The differences between EXN1 and EXDS1 are summarized as follows: 1) The maximum of N_i and N_s is $3 \times 10^4 m^{-3}$, 1-order smaller than those by EXDS1. 2) In EXN1, freezing of

Table C-3-3 Results of the sensitivity experiments (Table C-3-1) to ice nucleation rates. The suffix "max" to Nx means the maximum value in the domain during $0 < t < 213$ min. In the row of TQc .max, the time when TQc takes its maximum is shown in the bracket, which reflects the onset time of glaciation. In the columns of EXS1 and EXS2, values left to the arrow symbol denote the maxima during $0 < t < 120$ min, and values right to the arrow symbol denote the maxima during $120 < t < 213$ min.

	EXN1	EXDS1 $ds \times 10^3$	EXDS2 $ds \times 10^6$	EXHM -3 ~ -30	EXFZ1 Bigg $\times 10^2$	EXFZ2 Bigg $\times 10^5$	EXBK1 A=10	EXBK2 A=100	EXS1 0.95-1.75	EXS2 1.75-3.15
Ni .max(m^{-3})	3×10^4	3×10^5	10^7	2×10^5	4×10^5	3×10^8	10^5	3×10^7	$10^6 \rightarrow 3 \times 10^4$	$4 \times 10^5 \rightarrow 2 \times 10^4$
TNi .max(m^{-2})	8×10^5	10^7	6×10^8	8×10^6	8×10^5	4×10^7	2×10^6	6×10^9	$5 \times 10^7 \rightarrow 10^6$	$10^7 \rightarrow 3 \times 10^5$
TQi .max($0.1kg/m^2$)	6×10^{-5}	6×10^{-4}	3×10^{-2}	5×10^{-4}	4×10^{-4}	2×10^{-5}	10^{-4}	8×10^{-2}	$10^{-3} \rightarrow 5 \times 10^{-5}$	$4 \times 10^{-4} \rightarrow 7 \times 10^{-5}$
Ns .max(m^{-3})	2×10^4	2×10^5	10^6	2×10^5	10^5	10^6	2×10^5	10^6	$10^6 \rightarrow 3 \times 10^4$	$6 \times 10^5 \rightarrow 10^4$
TNs .max(m^{-2})	3×10^6	3×10^7	3×10^8	5×10^7	10^7	10^8	8×10^6	2×10^8	$10^8 \rightarrow 2 \times 10^6$	$4 \times 10^7 \rightarrow 3 \times 10^6$
Ng .max(m^{-3})	3×10^3	10^4	10^4	2×10^4	10^4	3×10^4	2×10^3	5×10^4	$10^4 \rightarrow 3 \times 10^3$	$2 \times 10^4 \rightarrow 10^3$
TNg .max(m^{-2})	2×10^5	7×10^7	10^6	2×10^6	8×10^5	10^6	10^5	2×10^6	$6 \times 10^5 \rightarrow 10^5$	$6 \times 10^6 \rightarrow 10^5$
TQc .max	1.2	0.4	0.1	0.8	0.5	0.1	1.1	1.1	< 0.1	0.3
($0.1kg/m^2$)	(67min)	(53min)	(80min)	(60min)	(53min)	(53min)	(67min)	(67min)	(47min)	(53min)
	1.5	1.3		1.6	1.3		2.0	1.4	2.7	1.5
	(147min)	(133min)		(140min)	(140min)		(147min)	(140min)	(113min)	(127min)
at $t=213$ min										
TQs ($0.1kg/m^2$)	1.2	3.4	4.6	3.7	3.2	4.2	1.7	4.8	2.1	2.0
$TPRs$ ($0.1kg/m^2$)	2.6	2.6	1.2	1.6	2.8	1.8	1.8	0.5	2.0	2.8
$TQs + TPRs$ ($0.1kg/m^2$)	3.8	6.0	5.8	5.3	6.0	6.0	3.5	5.3	4.1	2.8
TQg ($0.1kg/m^2$)	0.9	0.2	<0.1	0.2	0.3	0.2	0.0	0.2	0.6	0.1
$TPRg$ ($0.1kg/m^2$)	1.6	1.2	0.1	2.1	1.3	0.5	1.2	1.0	2.4	1.3
$TQg + TPRg$ ($0.1kg/m^2$)	2.5	1.4	0.1	2.3	1.6	0.7	1.2	1.2	3.0	1.4
$TPRs + TPRg$ ($0.1kg/m^2$)	4.2	3.9	1.2	3.7	4.1	2.3	3.0	1.5	4.4	4.1
" + $TQs + TQg$ ($0.1kg/m^2$)	6.3	7.4	5.9	7.6	7.6	6.7	4.7	6.5	7.1	6.2

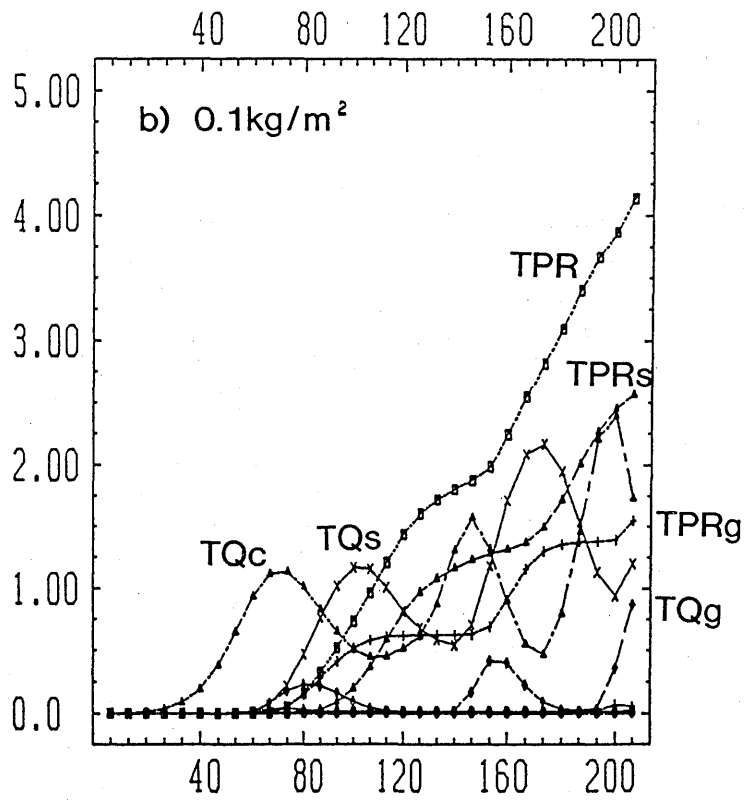
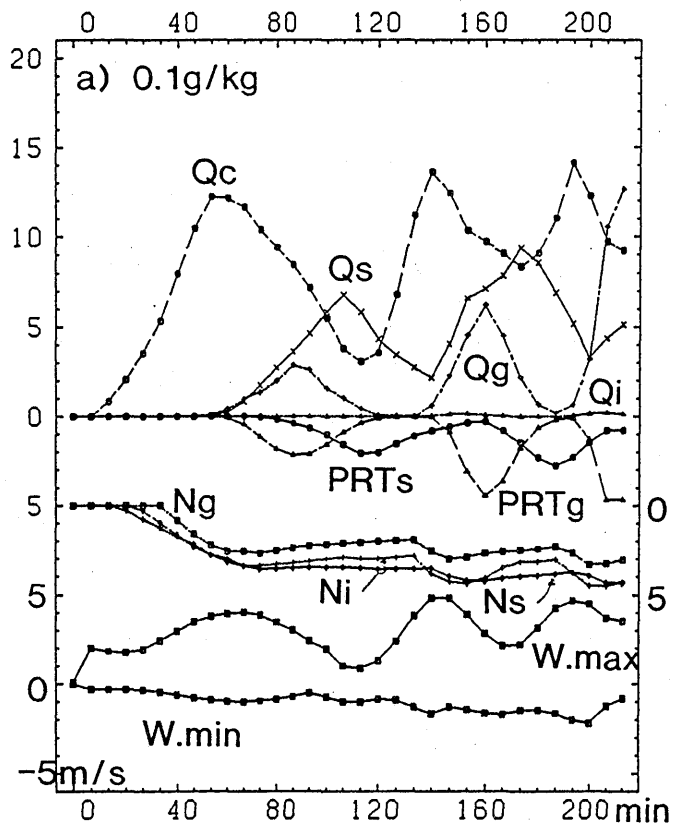


Fig. C-3-20 The same as Fig. C-3-7 but for EXN1.

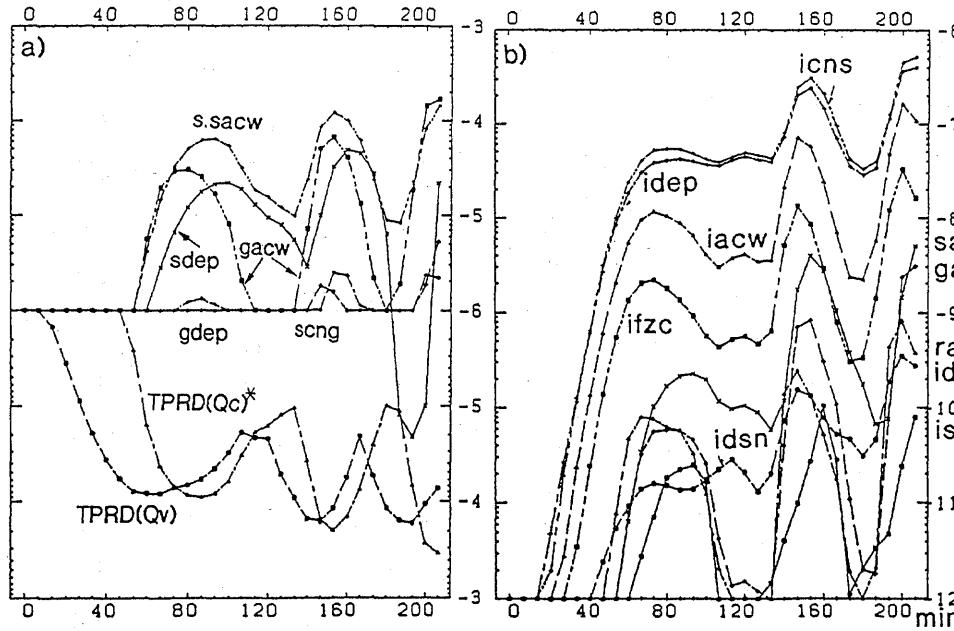


Fig. C-3-21 The same as Fig. C-3-17 but for EXN1.

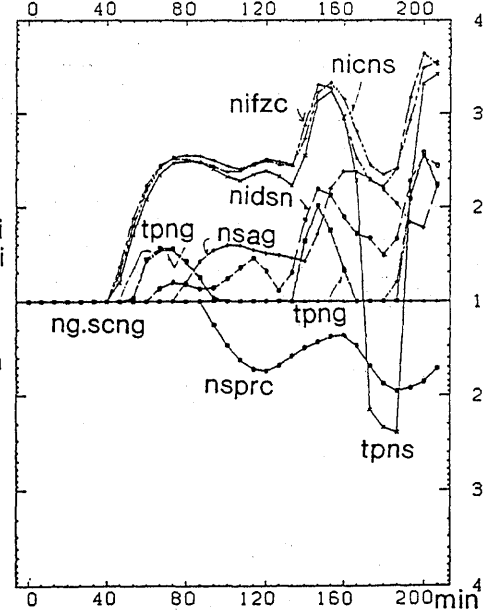


Fig. C-3-22 The same as Fig. C-3-18 but for EXN1 and $p_0 = 10$.

cloud droplets (P_{ifzc}) is the dominant generation term of cloud ice which is 10 times larger than deposition/sorption nucleation (P_{idsn}) but 1/10 of enhanced P_{idsn} in EXDS1. 3) TQ_c by EXN1 is larger than EXDS1 and TQ_s is by a factor of 0.3 ~ 0.5 smaller than that of EXDS1. 4) Glaciation in EXN1 occurs 13min later than EXDS1. As for 3), a qualitatively similar result was obtained by Rutledge and Hobbs (1984).

a-2) *EXDS2*

The differences between EXDS2 and EXDS1 are as follows: 1) TQ_c by EXDS2 is almost zero, much smaller than EXDS1. 2) The maxima of N_i and N_s are $10^7 m^{-3}$ and $10^6 m^{-3}$, respectively, much larger than those by EXDS1. 3) The cloud in EXDS2 is glaciated from the beginning of time, and main precipitation formation is depositional growth of cloud ice and snow rather than riming process. 4) Little precipitation occurs because of the small fall velocity of small snow particles.

a-3) *EXHM*

The differences between EXHM and EXDS1 are as follows: 1) TQ_c by EXHM is larger than EXDS1, although the maximum values of N_i and N_s are nearly the same as those by EXDS1. 2) The cloud in EXHM is glaciated 13min later than EXDS1, similar to EXN1. 3) The precipitation amount of graupel is much larger than that of EXDS1, while that of snow is much smaller than that of EXDS1. These characteristics are attributable to the timing of Hallet-Mossop rime-splinter production of ice nuclei. The number of ice crystals are almost the same as EXN1 until cloud water accumulates in air and riming occurs. Therefore, the beginning of glaciation is almost the same as EXN1. However, once riming takes place, the number of cloud ice particles rapidly increases, resulting in sharp glaciation.

a-4) *EXFZ1 and EXFZ2*

As shown in Table C-3-3, the results of EXFZ1 are similar to those of EXDS1, and those of EXFZ2 are between those of EXFZ1 and EXDS2.

a-5) *EXBK1 and EXBK2*

The characteristic features of EXBK1 are as follows: 1) During $0 < t < 80$ min when production and growth of graupel and snow are small, the results of EXBK1 are similar to EXN1. The beginning of glaciation is almost the same as EXN1. 2) TQ_s is larger than that

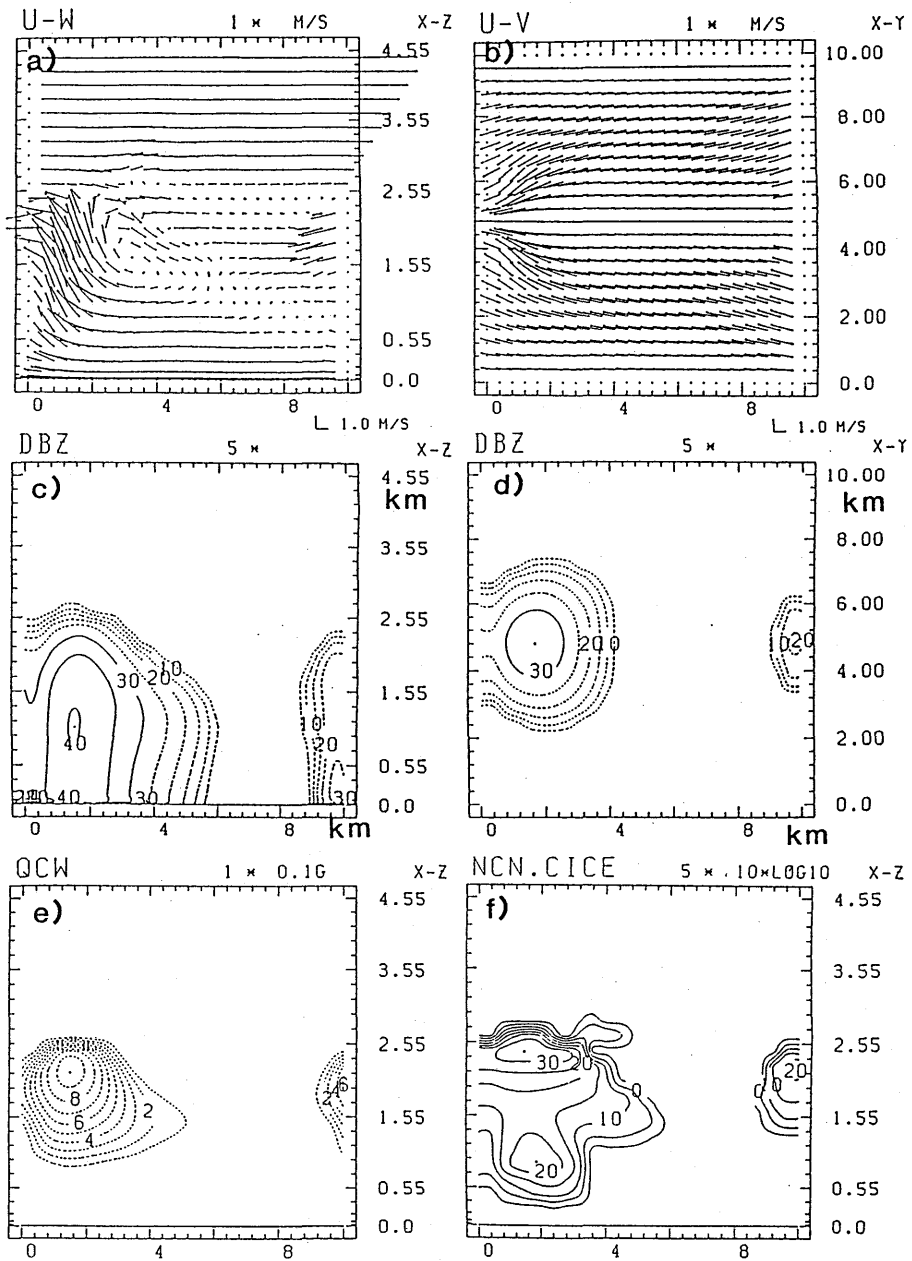
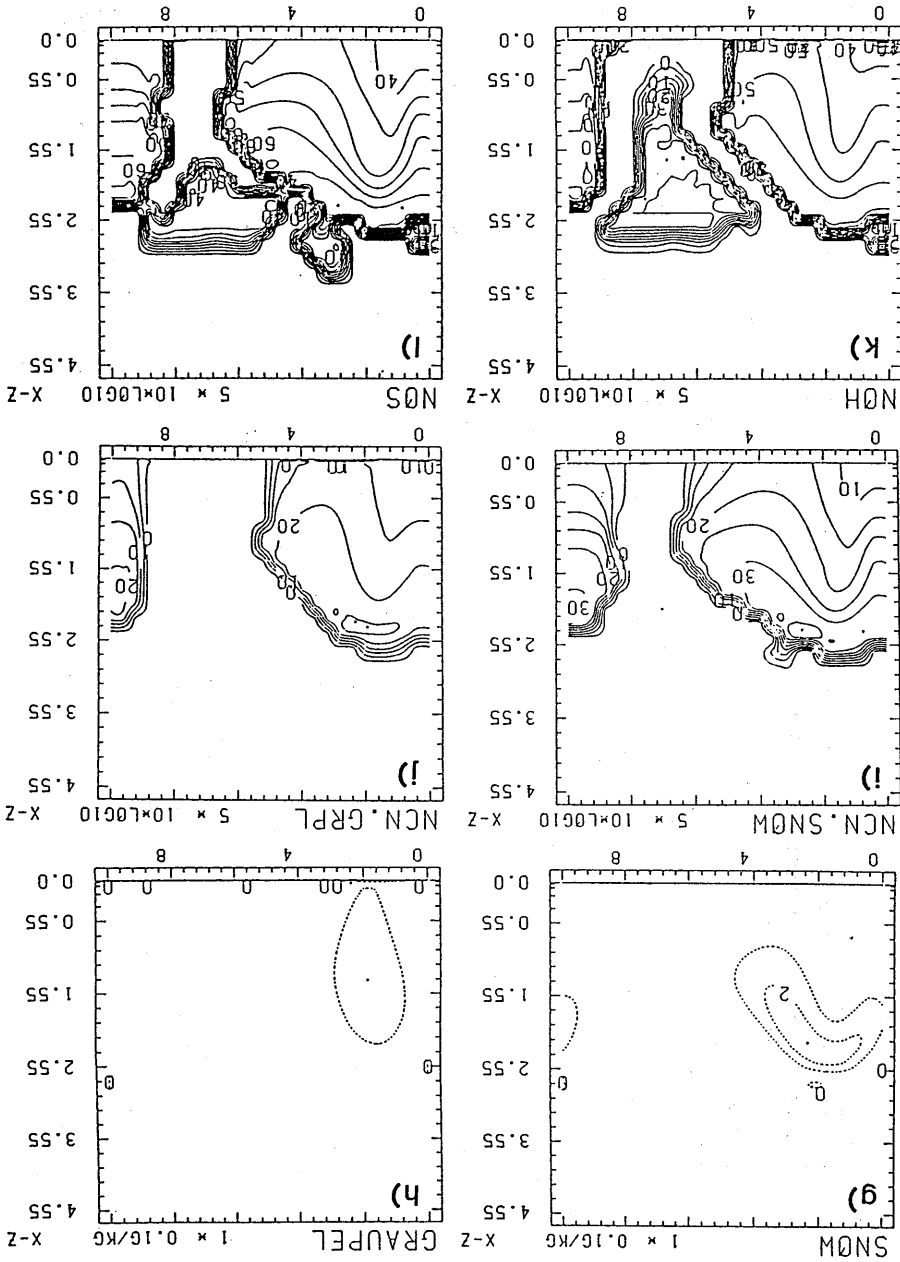


Fig. C-3-23 The same as Fig. C-3-10 but for EXN1.

Fig. C-3-23 (Continued.)



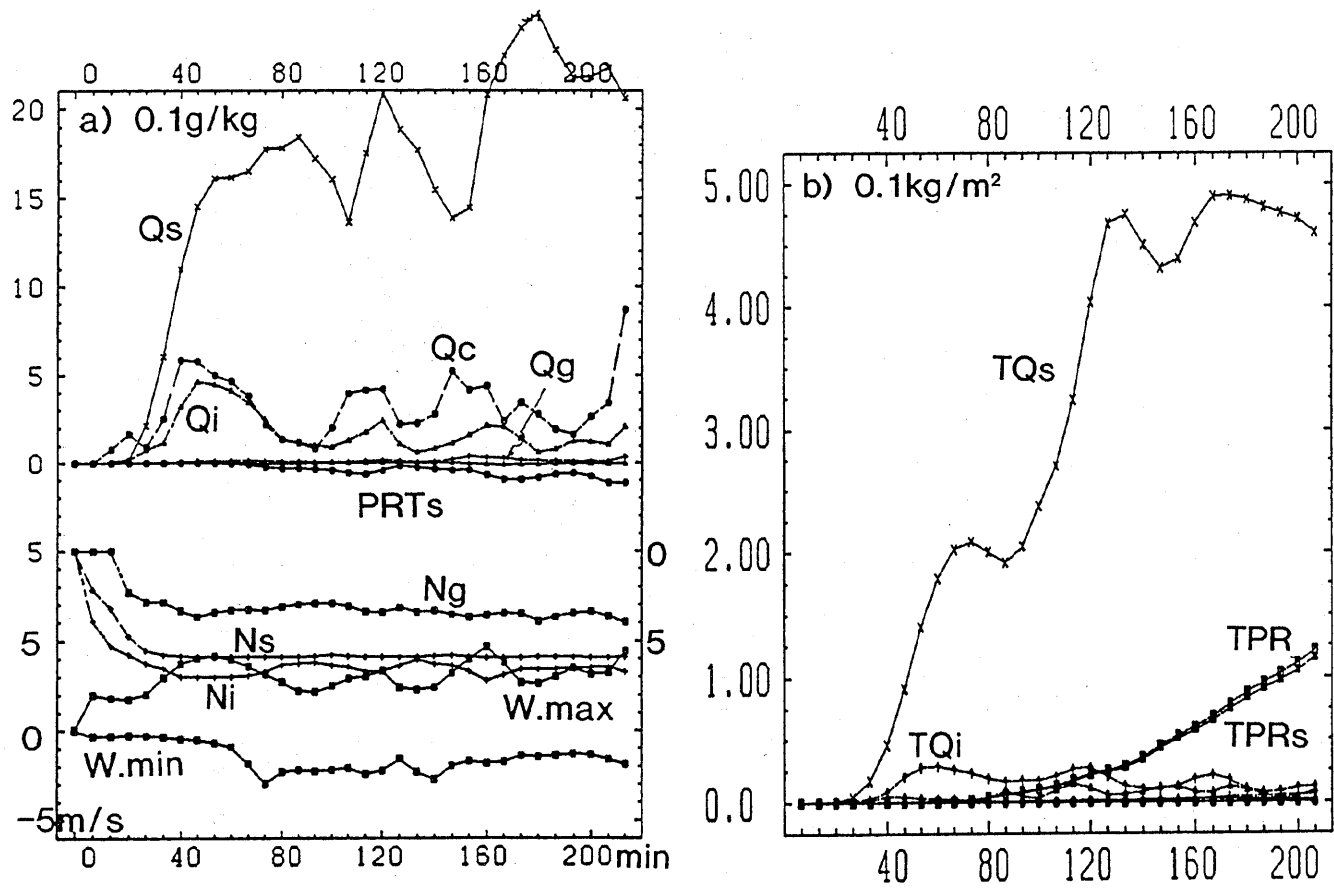


Fig. C-3-24 The same as Fig. C-3-7 but for EXDS2. The unit of Q_i in a) is 0.1 g/kg.

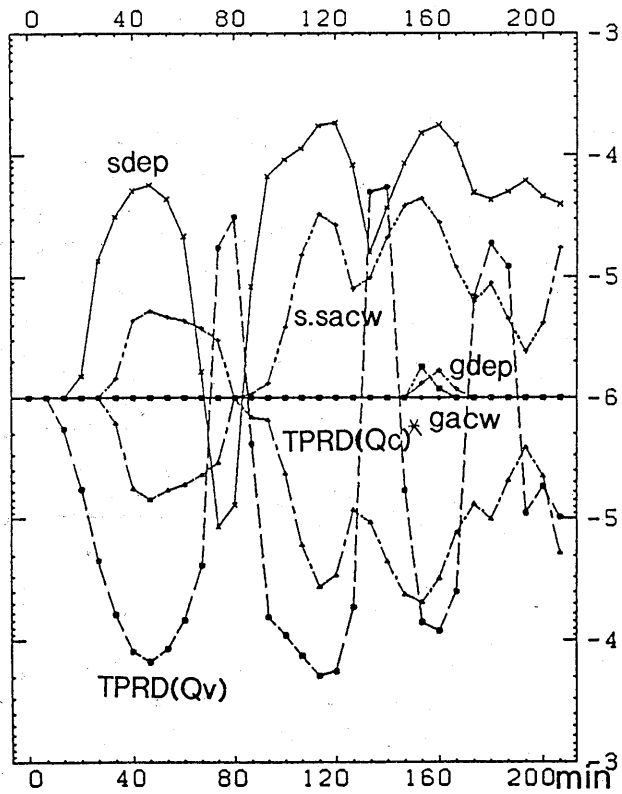


Fig. C-3-25 The same as Fig. C-3-17 but for EXDS2.

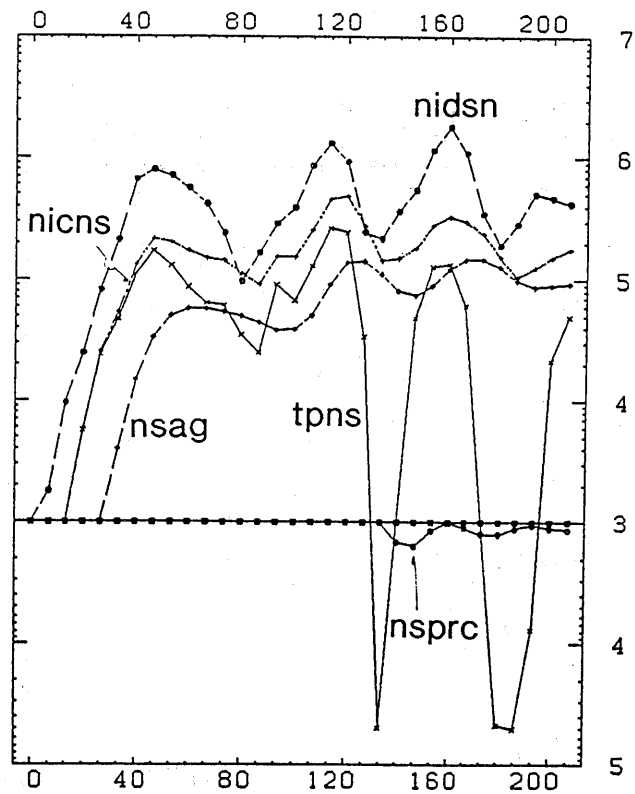


Fig. C-3-26 The same as Fig. C-3-18 but for EXDS2 and $p_0 = 10^3$.

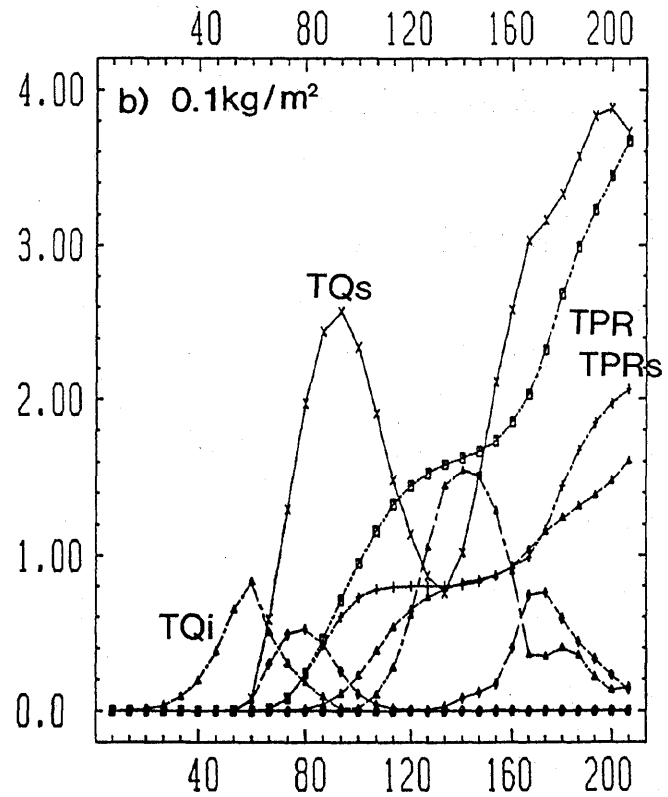
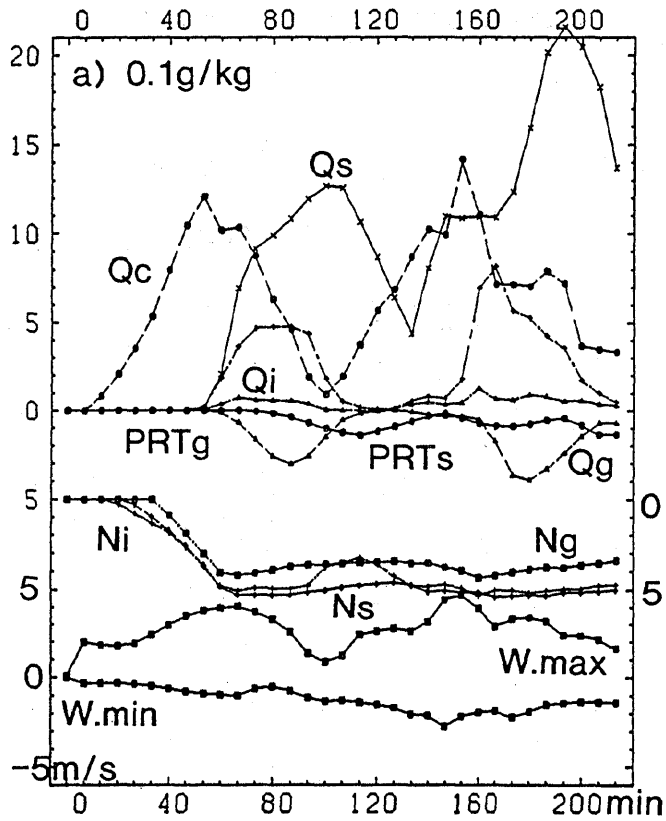


Fig. C-3-27 The same as Fig. C-3-7 but for EXHM.

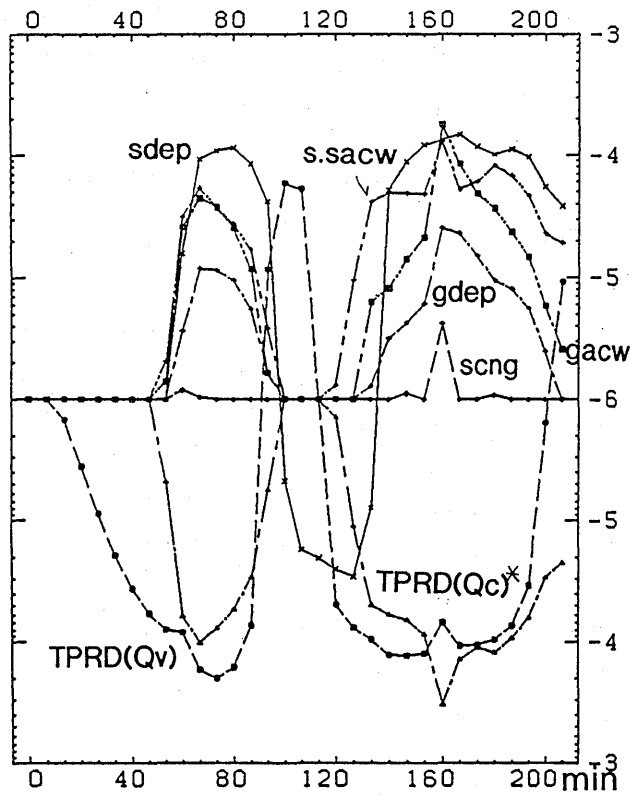


Fig. C-3-28 The same as Fig. C-3-17 but for EXHM.

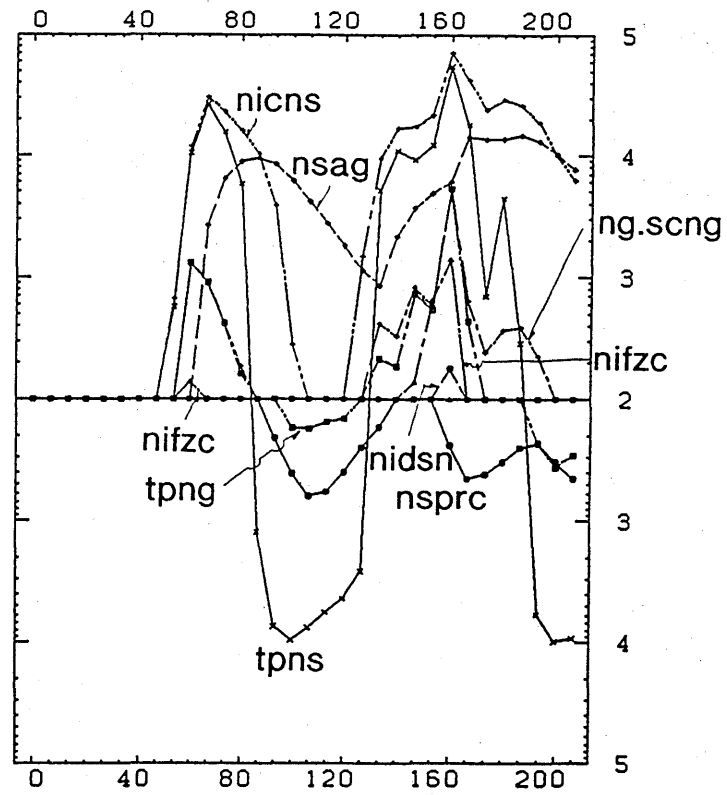


Fig. C-3-29 The same as Fig. C-3-18 but for EXHM and $p_0 = 10^2$.

of EXN1. 3) TNi and TNs are 2 ~ 3 times larger than those of EXN1 and almost the same as those of EXDS1.

The characteristic features of EXBK2 are as follows: 1) The maximum value of TQc is similar to that of EXN1. 2) TNi and TNs are 10^3 times larger than those of EXN1. 3) The precipitation amount is 1/3 of EXN1. Remarkable increase of Ni and Ns is attributable to that the number of collisions between snow and graupel is proportional to the product of Ns and Ng .

a-6) EXS1 and EXS2

The characteristic features of EXS1 are as follows: 1) During $0 < t < 60$ min, the results of EXS1 are similar to those of EXDS2 in large Ni , Ns and Qs , and very small Qc , Qg and little precipitation. 2) During $120 < t < 213$ min, the results of EXS1 are similar to those of EXN1 in large Qc , Qg , large precipitation rate and small Ni and Ns . Seeding effect in suppressing precipitation is remarkable (overseeding) until $t = 100$ min. However, this effect does not continue long. The seeding effect of EXS2 is not so remarkable as that of EXS1, indicating that seeding at the lower part is more effective.

a-7) Summary

In EXN1, the maximum value of number concentration of ice particles is 1/4 of the observed counterpart. The dominant generation term of cloud ice is not deposition/sorption nucleation ($Pidsn$, $Nidsn$) but freezing of cloud droplets ($Pifzc$, $Nifzc$). Freezing of cloud droplets can produce fairly large number concentration of ice particles which is still smaller than the observed one but appears to be in a tolerable range. The number concentration of ice particles is 1-order smaller than that of EXDS1. The radar reflectivity is the largest among all experiments, yielding a difference of 10dBZ from the observed value.

The increase in the number concentration of ice crystals to the observed value ($2 \times 10^5/m^3$) by enhancing Fletcher's deposition/sorption nucleation results in rapid glaciation (13min earlier), the decrease of cloud water, the increase of deposition, the decrease of riming, the increase of the number concentration of graupel, the increase of snow in mass and number, the decrease of the precipitation intensity of snow and the decrease of radar reflectivity to 37dBZ.

A further increase in the number concentration of ice crystals to the value ($10^7/m^3$) results in suppression of precipitation and glaciation of cloud with little cloud water, little

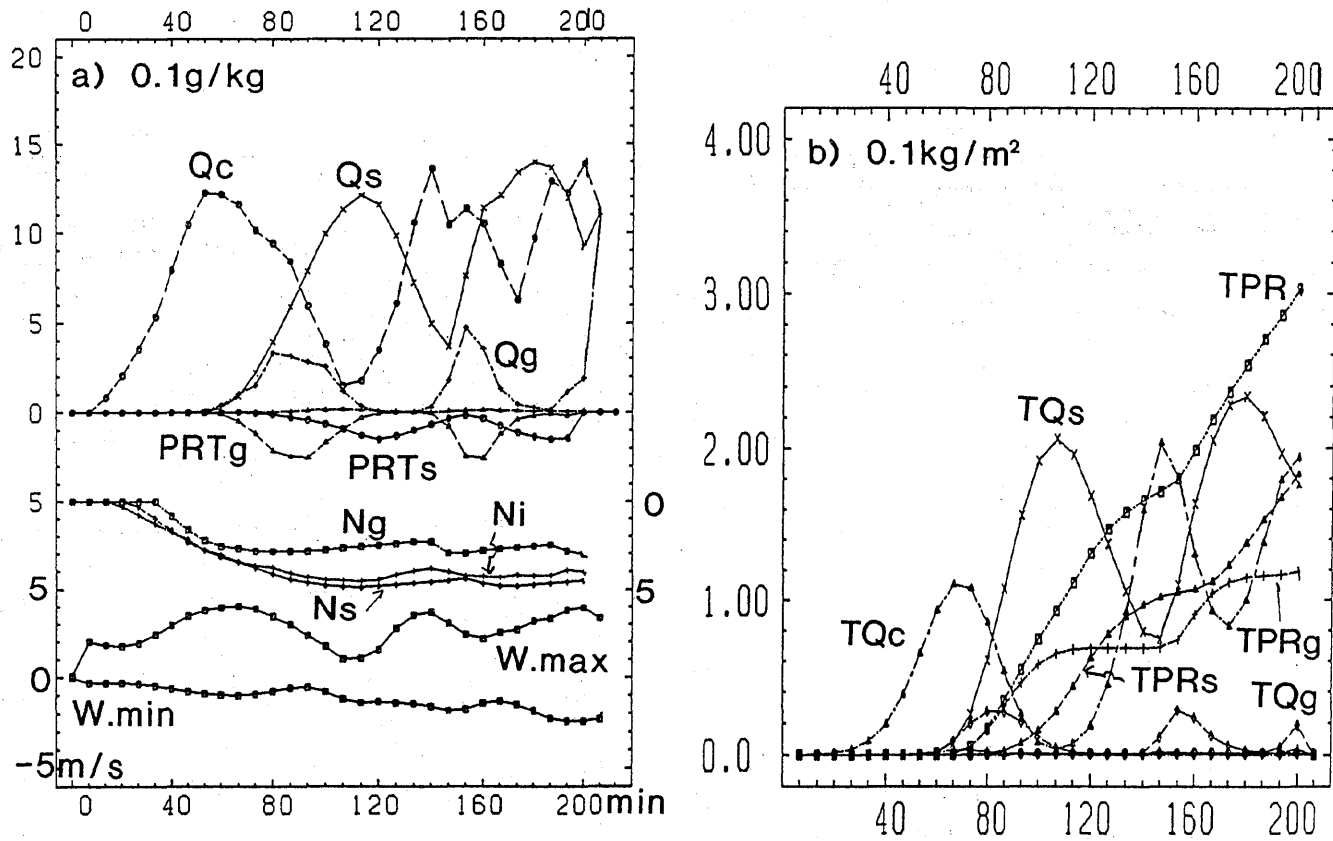


Fig. C-3-30 The same as Fig. C-3-7 but for EXBK1.

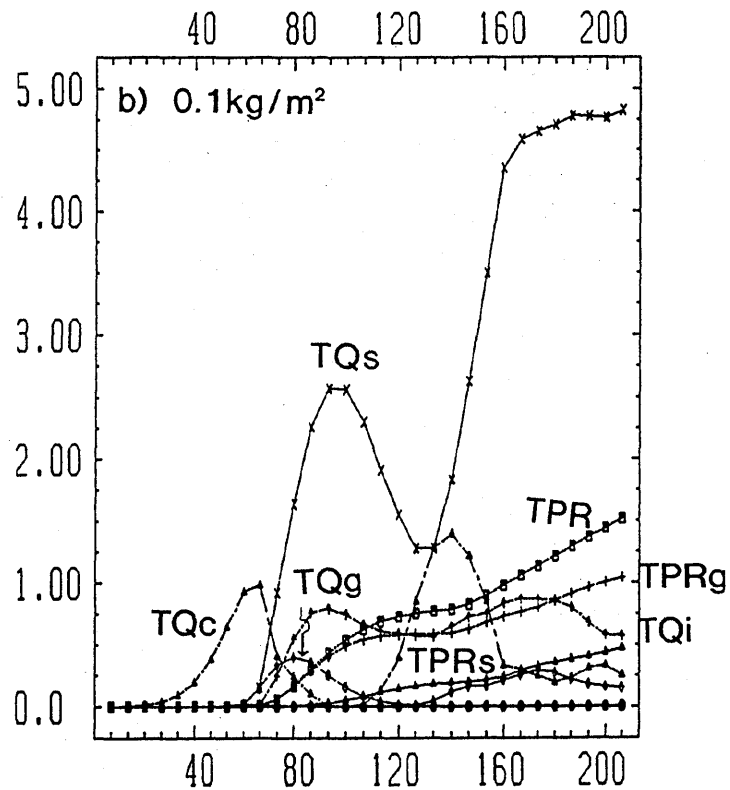
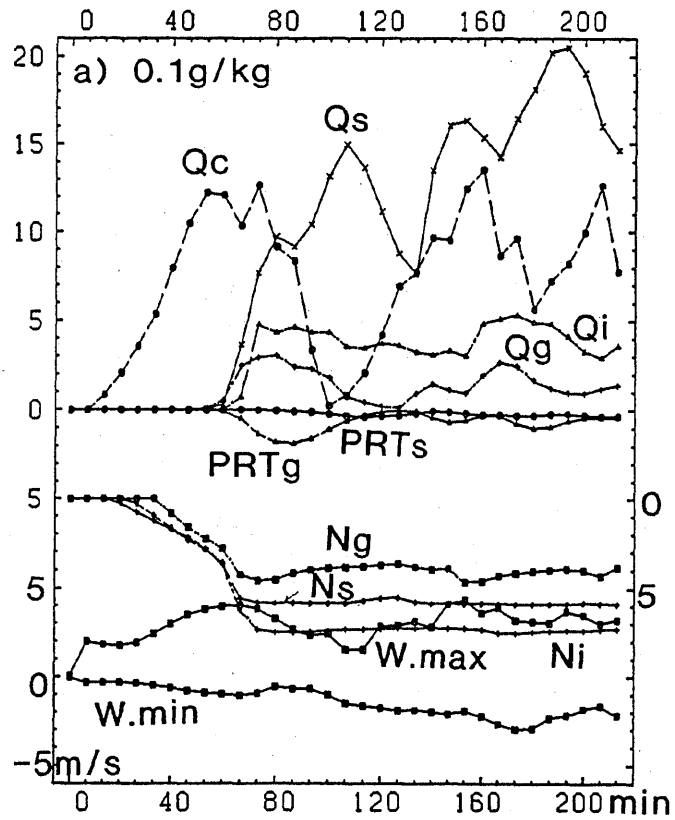


Fig. C-3-31 The same as Fig. C-3-7 but for EXBK2.

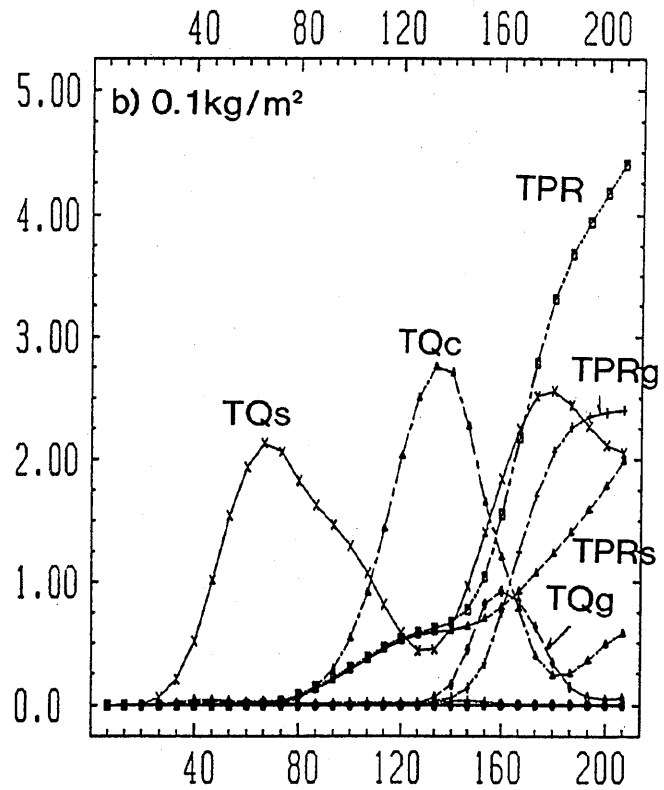
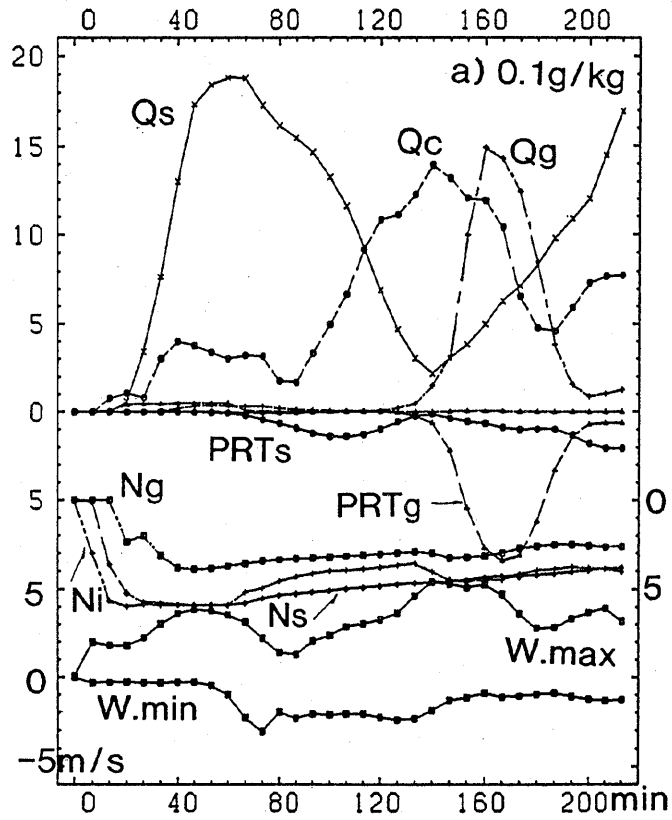


Fig. C-3-32 The same as Fig. C-3-7 but for EXS1.

graupel and abundant snow.

Based on these experiments including seeding experiments EXS1 and EXS2, it can be said that there is the possibility of suppressing precipitation or changing the location of precipitation leeward by overseeding.

The maximum of the number concentrations of cloud ice and snow obtained from EXN1, EXDS1, EXFZ1, EXHM and EXBK1 lies within a tolerable range, *i.e.*, within one order different from the observed counterpart. There are differences among these experiments in the amount of cloud water (TQc) and the onset time of glaciation. In EXHM and EXBK1, the amount of cloud water and onset time of glaciation are nearly the same with EXN1, while, in EXDS1, TQc is smaller and the onset time is earlier than that in EXN1. In most experiments, the level of the maximum Ni is higher than that of the maximum Qc by 0.5 ~ 1.0km. However, EXHM shows the proximity of both levels. In addition to these numerical sensitivity experiments, more observations are needed, especially on the developing stage of the cloud, for more understanding of the ice nucleation processes.

b) Sensitivity to r_0

The parameter r_0 (Eq. B-(11-27), Table B-11-1) is assumed to be the minimum radius of snow and graupel particles which determines the minimum weight of snow and graupel particles as follows:

$$m_{s0} = \frac{4\pi}{3} \rho_s r_0^3, \quad m_{g0} = \frac{4\pi}{3} \rho_g r_0^3.$$

The conversion term from cloud ice to snow (Picns: Eq. B-(11-30)) is highly dependent on m_{s0} . The conversion term from cloud ice to graupel via riming (Picng: Eq. B-(11-36)); Pgiacw: Eq. B-(11-38)) is also highly dependent on m_{g0} . However, in the present case, Pgiacw is less than Pidep, and Picng is not effective. Picns almost balances Pidep. As shown in Table C-3-4, the number and mass of cloud ice are highly dependent on the parameter r_0 , while the number of snow particles is not so sensitive to it from a global point of view. The total precipitation is not dependent on r_0 as shown in Table C-3-4. However, locally speaking, the parameter brings about some differences in the snow field. Around the region where updraft is strong and snow and graupel particles are vigorously generated, the number of snow particles in the case of small r_0 is larger than that for large r_0 , as shown in Fig. C-3-33. As a consequence, radar reflectivity for $r_0 = 50\mu\text{m}$ attains 33dBZ at this region, smaller than 37dBZ in the case of $r_0 = 75\mu\text{m}$ (see Fig. C-3-11e). Smaller r_0 gives rise to more realistic

Table C-3-4 Sensitivity to the parameter r_0 . "rnn" denotes the experiment which adopts the value "nn" μm for r_0 . In the experiments in the table, the value 32 is used for $\alpha 2\Delta t$. The unit of $Ni.\text{max}$ and $Ns.\text{max}$ is m^{-3} ; "max" denotes the maximum value during $0 < t < 213$ min; the unit of TQi , ... $TPR.g$ is kg/m^2 .

	$Ni.\text{max}$	TQi	$Ns.\text{max}$	TQs	$TPR.s$	TQg	$TPR.g$	$dBZ.\text{max}$
EXDS1.r50	$10^{5.0}$	2.8×10^{-5}	$10^{5.3}$	0.34	0.25	0.01	0.11	33
EXDS1.r75	$10^{5.3}$	6.0×10^{-4}	$10^{5.3}$	0.34	0.26	0.02	0.12	36-37
EXDS1.r100	$10^{5.8}$	1.2×10^{-3}	$10^{5.4}$	0.31	0.24	0.02	0.13	40

Table C-3-5 Sensitivity to the parameter $\alpha 2\Delta t$. "ann" denotes the experiment which adopts the value "nn" for $\alpha 2\Delta t$. $SUM.x \equiv TPR.x + TQx$ ($x = s$ or g). Values at $t = 213$ min are listed. The unit of TQx and $TPRx$ is kg/m^2 .

	TQs	$TPR.s$	$SUM.s$	TQg	$TPR.g$	$SUM.g$	$TPR.g/TPR.s$	$SUM.g/SUM.s$
EXN.a10	0.18	0.32	0.50	0.06	0.09	0.15	0.28	0.30
EXN.a32	0.12	0.26	0.38	0.09	0.15	0.24	0.58	0.63
EXN.a80	0.06	0.16	0.22	0.11	0.26	0.37	1.6	1.7

dBZ, but more unrealistic Ni .

c) Sensitivity to $\alpha 2\Delta t$

The parameter $\alpha 2\Delta t$ (see Eq. B-(11-43)) has a large influence on the conversion term of snow into graupel via riming (Pscng). Results of sensitivity experiments to $\alpha 2\Delta t$ are summarized in Table C-3-5. As $\alpha 2\Delta t$ becomes large, more graupel is generated and snow is suppressed. From observational studies, the ratio of the precipitation amount of graupel over that of snow is about 0.1 ~ 1.3 (Konishi *et al.*, 1989; Mizuno, 1989). An appropriate value for $\alpha 2\Delta t$ is considered to be 10 ~ 40.

C-3-7 Comparison with observations

Comparison with observations is summarized in Table C-3-6. Main discrepancy is in radar reflectivity. As for the maximum of the number concentrations of cloud ice and snow, EXN1, EXDS1, EXFZ1, EXHM and EXBK1 reproduce it within a tolerable range.

a) Contribution ratio of riming over deposition to the growth of ice particles

Harimaya and Sato (1989) measured the contribution ratio of riming over deposition to the growth of snow aggregates around Sapporo. They reported as follows: When a strong

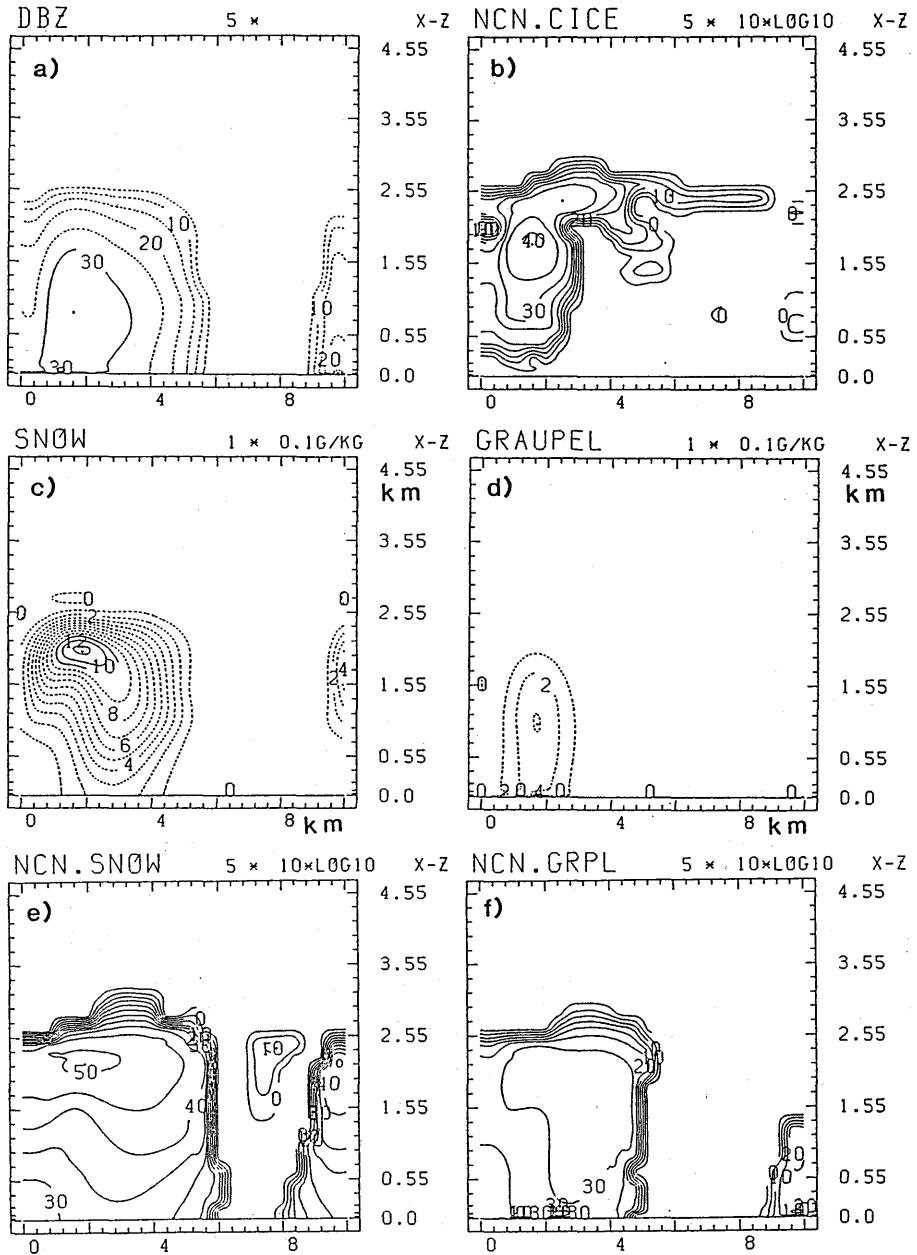


Fig. C-3-33 X-z cross sections at $t = 80$ min by EXDS1.r50.
 a) The same as Fig. C-3-10c but for $r_0 = 50\mu\text{m}$.
 b) The same as Fig. C-3-10f but for $r_0 = 50\mu\text{m}$.
 c) The same as Fig. C-3-10g but for $r_0 = 50\mu\text{m}$.
 d) The same as Fig. C-3-10h but for $r_0 = 50\mu\text{m}$.
 e) The same as Fig. C-3-10i but for $r_0 = 50\mu\text{m}$.
 f) The same as Fig. C-3-10j but for $r_0 = 50\mu\text{m}$.

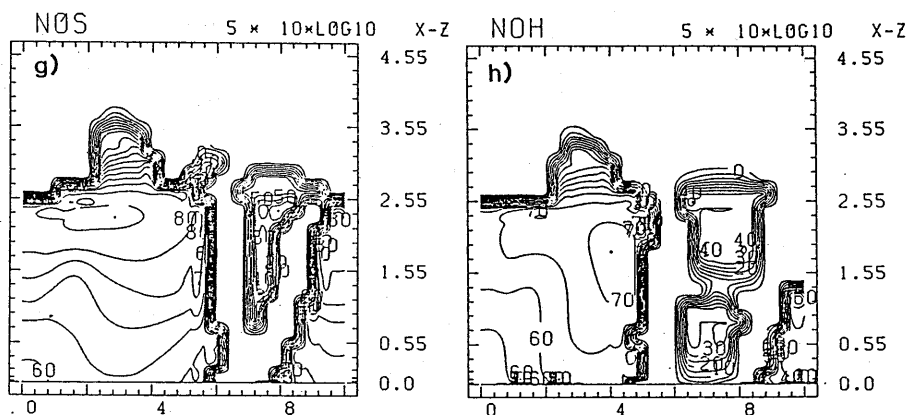


Fig. C-3-33 (Continued.)

- g) The same as Fig. C-3-10k but for $r_0 = 50\mu\text{m}$.
 h) The same as Fig. C-3-10l but for $r_0 = 50\mu\text{m}$.

Table C-3-6 Comparison between results of EXN1 and EXDS1 and observations at Tobishima (Murakami *et al.*, 1990) and Otaru (Magono and Lee, 1973).

	Tobishima (1989) Feb.			Otaru (1970) Jan.
	EXN1	sim. EXDS1	obs.	obs.
cloud top(km)	3.0	3.0	3.0	1.5 ~ 2.5
temp.(°C)	-20	-20		-15 ~ -22
cloud base	0.7	0.7	1.0	0.5 ~ 1.5
temp.(°C)	-8	-8		-9 ~ -15
horizontal scale (km)	5	5	5	
max.w(m/s)	4	4		
max dBZ	40	37	30	
max.Qc(g/kg)	1.4	1.0	0.12	1.0
max.(Ni + Ns)(m ⁻³)	5×10^4	5×10^5	2×10^5	5×10^4
max.Qs(g/kg)	0.7	1.2	0.25	0.1

snow cloud passed over the observation site, first, graupel particles fell and riming proportion increased (80–100%). Then the snowfall intensity continues to increase gradually. By contrast, the riming proportion decreased from 80–100% to 60%. In the later stage, both the snowfall intensity and riming proportion become small (40–60%). Mizuno *et al.* (1990) also observed snow clouds around Sakata. From their observation, at the first stage, graupel and heavily rimed snow particles fell with the riming proportion greater than 70%. At a later stage, rimed snow particles with the riming proportion of about 50% fell.

Table C-3-7 Riming proportion ratio in EXDS1 and EXN1.

	EXDS1		EXN1			
	developing to mature	mature to decay	developing to mature	mature to decay		
<i>t</i> (min)	60	133	80	80	147	100
<i>Rrim</i>	0.54	0.76	0.41	0.85	0.80	0.56

These characteristic features are well reproduced by the model. The riming proportion ratio defined as

$$Rrim = \frac{TPs.sacw + TPg.sacw + TPgacw}{TPs.sacw + TPg.sacw + TPpdep + TPgacw + TPgdep}$$

is listed in Table C-3-7. This ratio does not directly correspond to the observed ones by Harimaya and Sato (1989) and Mizuno *et al.* (1990). However, it can be said that, at least qualitatively, the model reproduces the riming proportion ratio successfully.

b) Comparison of Nos and Nog with observations

Harimaya (1978) observed size distributions of snow and graupel around Sapporo (43.08N, 141.35E). Yagi *et al.* (1979) did the same at Nagaoka (37.45N, 138.80E). Kajikawa and Kiba (1878) observed that of graupel around Akita (39.75N, 140.10E). These observed Nos and Nog as a function of precipitation rate R (mm/hr) are plotted in Fig. C-3-34, together with Nos obtained by Gunn and Marshall (1958). Sapporo and Nagaoka are located about 15km distant from the sea coast. Moreover, a range of hills as high as 400m lies between Nagaoka and the sea coast. Therefore, the clouds observed by Harimaya and Yagi *et al.* are not considered to be representative convective clouds over the warm Sea of Japan. The dependency of Nos and Nog on precipitation rate, R , show a lot of variation, suggesting the complex influence of meteorological and geographical conditions on Nos and Nog . This dependency of Nos on R is different from Gunn-Marshall's which is considered to fit well with the stratiform cloud where aggregational growth is dominant.

For the observed case of Feb. 4, 1989 at Tobishima (see Fig. C-3-4), Nos estimated by extrapolating the size distribution curve to $D = 0$ is $10^6 \sim 8 \times 10^7 m^{-4}$, showing a large variation with height. On the other hand, that estimated by the formula based on the inverse exponential size distribution function,

$$Nos = N_s \left(\frac{\pi \rho_s N_s}{\rho Q_s} \right)^{1/3}$$

Table C-3-8 N_{os} and N_{og} (m^{-4}) simulated in EXDS1 and EXN1 as a function of the cloud stage and precipitation rate, R (mm/hr). These are shown in Fig. C-3-34 (EXDS1, Δ ; EXN1, \times).

	EXDS1			EXN1		
time(min)	80	100	120	100	113	127
PRCP.s(mm/hr)	1.0	2.0	1.0	1	2.5	1
$N_{os}(m^{-4})$	2×10^6	2×10^7	5×10^7	1×10^5	3×10^5	5×10^5

	EXDS1			EXN1		
time(min)	73	80	87	80	87	93
PRCP.g(mm/hr)	1	2.5	1	1	2.5	1
$N_{og}(m^{-4})$	1×10^6	2×10^6	3×10^6	3×10^4	6×10^4	2×10^5

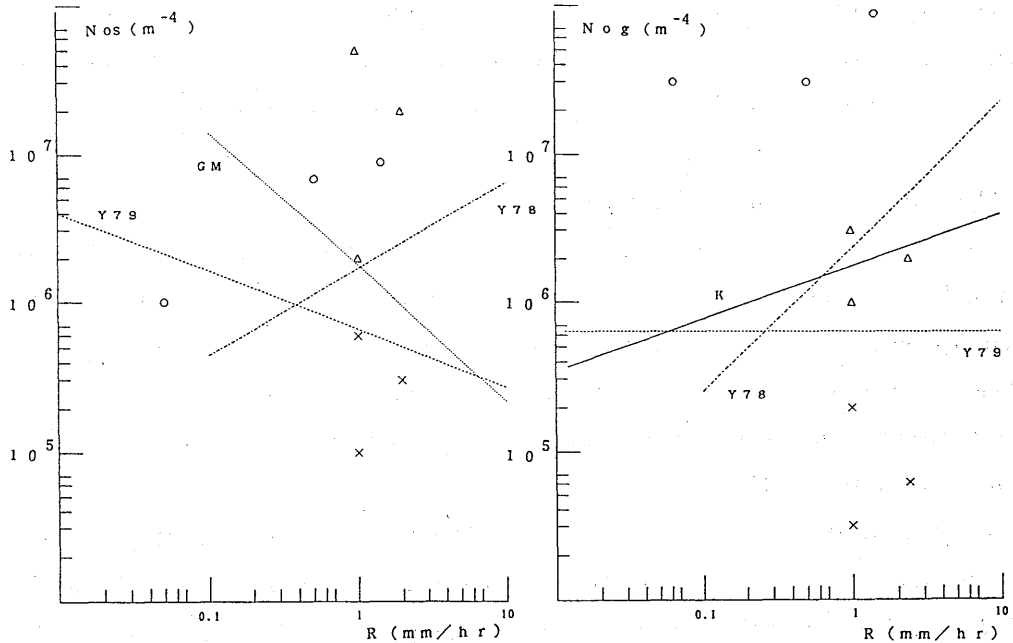


Fig. C-3-34 N_{os} and N_{og} (m^{-4}) simulated in EXDS1 (Δ) and EXN1 (\times) as a function of precipitation rate, R (mm/hr). Empirical formula of Yagi *et al.* between N_{os} and R based on observational studies for the cases of 1978 and 1979 are indicated by Y78, and Y79; that of Kajikawa by K; that of Gunn and Marshall by GM. Harimaya's data are indicated by \circ .

with substitution of $N_s = 10^5 m^{-3}$ and $\rho Q_s = 0.13 g/m^3$, is $6 \times 10^8 m^{-4}$. This large difference means the inadequacy of the assumed inverse exponential size distribution. Precipitation rate for this case is about $R = 0.5 mm/hr$.

N_{os} and N_{og} in the simulated clouds are listed in Table C-3-8, and also added in Fig. C-3-34. N_{os} and N_{og} obtained in the simulation show remarkable dependency on the stage

of the cloud rather than the precipitation rate. Nog increases monotonically as the cloud evolves from stage 3 to 5; Nog at the stage 5 is larger than that at stage 3, even for the same precipitation rate. The same can be said about Nos . The examples of Nos in EXN1 are shown in Fig. C-3-35. These results simply reflect the fact that relatively large particles fall down to the ground faster than smaller ones and that large particles are more abundant at the developing or mature stage of cloud than small ones at the decaying stage.

A direct comparison between the observed and simulated Nos and Nog is not fruitful because of neglecting the stage of the cloud in observations and the long distance of Sapporo and Nagaoka from the sea coast. With these reservations, the following might be said: Nos of EXDS1 is larger than the observed counterpart, while Nos of EXN1 is smaller; Nog of EXDS1 is close to the observed counterpart, while Nog of EXN1 is smaller. These discrepancies are partly related to the essential unknowns about ice nucleation terms, and partly to the insufficiency of the bulk parameterization adopted in the model.

C-3-8. Summary and conclusion

We have developed a bulk parameterization scheme of cloud microphysics which predicts not only the number concentrations of cloud ice and snow but also that of graupel (Ni , Ns and Ng) in addition to the mixing ratios of six water species (water vapor, cloud water, cloud ice, snow and graupel), and this scheme is applied to the 3-dimensional simulation of the convective snow cloud observed over the Sea of Japan on Feb. 4, 1989, with the cloud top temperature at -20°C .

Sensitivity experiments are conducted for three kinds of generation terms, *i.e.*, ice nucleation rates (C-3-6 a)), the conversion term of cloud ice into snow via depositional growth (C-3-6 b); $Picns$), and the conversion term of snow into graupel via riming growth (C-3-6 c); $Pscng$).

Ice nucleation terms exert a large influence on the number concentrations of cloud ice, snow and graupel, the amount of supercooled cloud water, the amounts of riming and deposition and the timing of glaciation. When conventional parameters for Fletcher's deposition/sorption nucleation, Bigg's freezing of supercooled droplets and Hallet-Mossop rime splinter nucleation are used, the maximum number of ice particles reproduced by the model is 1/4 of the observed counterpart. Radar reflectivity is larger by 10dBZ than the observed one, and Nos and Nog are smaller than the observed ones. In this case, freezing of cloud droplets plays a dominant role in ice crystal generation rather than Fletcher's deposition/sorption

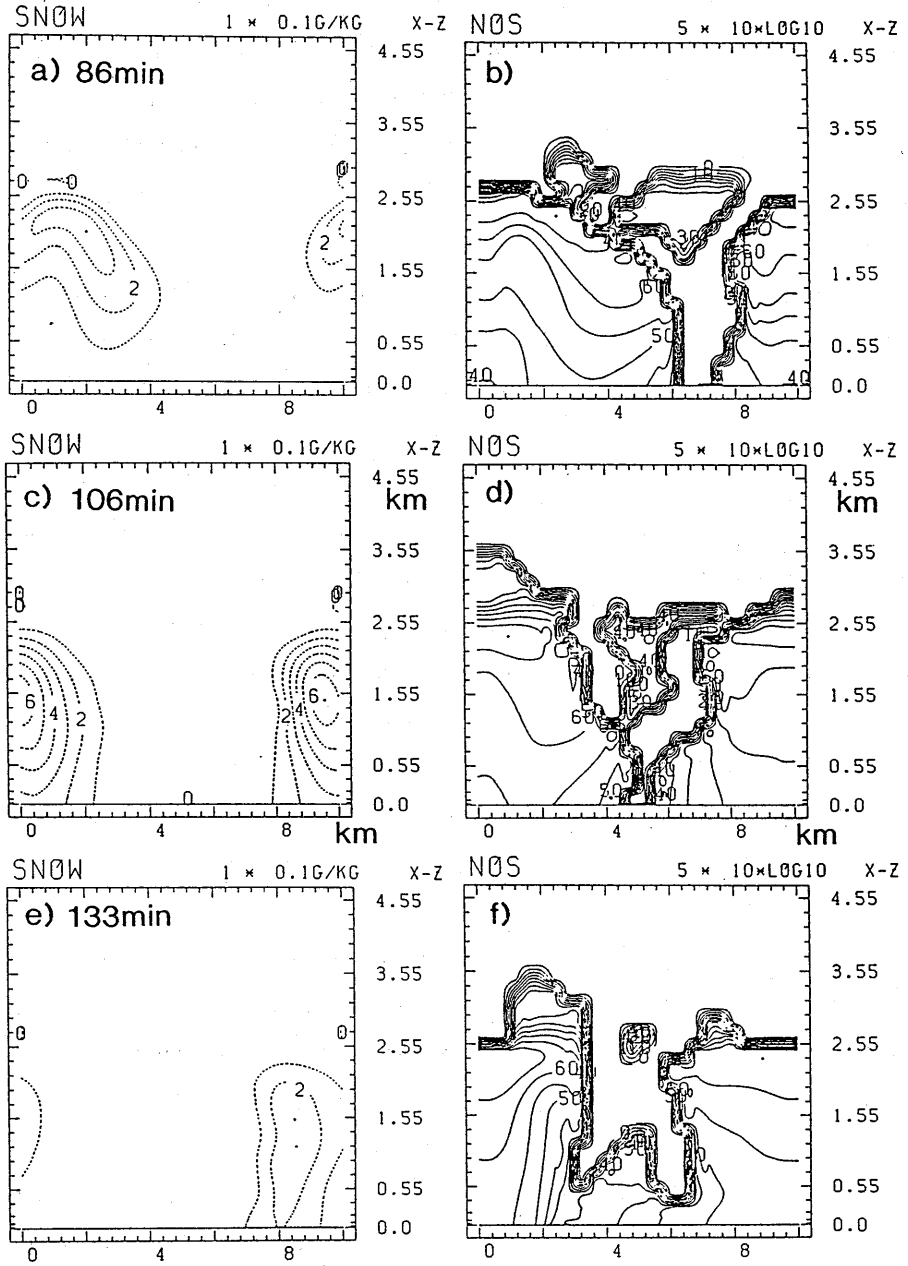


Fig. C-3-35 Q_s and Nos fields by EXN1.

- a) X-z cross section of Q_s at $t = 87$ min with contour intervals of 0.1 g/kg.
- b) X-z cross section of $\log_{10}(Nos)$ at $t = 87$ min with contour intervals of 5. The unit of Nos is m^{-4} .
- c) The same as a) but for $t = 107$ min.
- d) The same as b) but for $t = 107$ min.
- e) The same as a) but for $t = 133$ min.
- f) The same as b) but for $t = 133$ min.

nucleation. When ice nucleation terms are enhanced to reproduce the number concentration of 10^5-10^6m^{-3} , the amount of supercooled cloud water decreases, the amount of snow increases in mass and number, and radar reflectivity decreases. Further enhancement of the number concentration of ice particles to 10^6-10^7m^{-3} leads to the suppression of precipitation with abundant snow in air. This gives some support to the possibility of suppression of precipitation by overseeding.

Sensitivity experiments to the parameter r_0 which has a large influence on the conversion term of cloud ice into snow (Picns) reveals that the parameter r_0 have a large influence on the mass and number of cloud ice particles, but not on the mass and number of snow and graupel particles.

Sensitivity experiments to the parameter $\alpha 2\Delta t$ which has a large influence on the conversion term of snow into graupel (Pscng) reveals that the parameter $\alpha 2\Delta t$ has a large influence on the mass and number of snow and graupel particles and their precipitation amount. $\alpha 2\Delta t$ is tuned so as to reproduce the observed ratio of precipitation amount of graupel to that of snow, and $10 \leq \alpha 2\Delta t \leq 40$ is found to be appropriate for the present case. Such a tuning appears to be inevitable to some extent in a bulk parameterization.

Precipitation formation in the simulated cloud is as follows (C-3-5 c)): The water vapor supplied from the warm sea surface is lifted upward by convection and condenses to form supercooled cloud droplets. At the developing and mature stages of the cloud, these supercooled droplets are accreted on snow and graupel particles, and this riming process is more dominant than the depositional process in precipitation formation. At the dissipation stage, almost all of the supercooled cloud droplets are depleted, and graupel particles are absent; depositional growth is the dominant process for the growth of snow above the cloud base; below it, sublimation from snow particles is active enough to be almost equal to deposition above the cloud base. Aggregation of snow becomes active after the mature stage. The net decrease in the number of snow at the decayed stage is due to aggregation, precipitation and sublimation. These features are consistent with observational studies of Harimaya and Sato (1989) and Mizuno *et al.* (1990).

In this simulation, N_{os} and N_{og} are found to be more dependent on the stage of the cloud than the precipitation rate. Even for the two cases of the same precipitation rate, N_{os} at the developing stage is smaller than that at the dissipating stage. This point should be confirmed in future field experiments.

The merits of predicting number concentrations of cloud ice, snow and graupel are as

follows:

- i) No need of the prescription of N_{os} and N_{og} .
- ii) Capability of simulating the separation between heavy large particles and light small particles via precipitation.
- iii) Capability of simulating aggregational growth.
- iv) Applicability to seeding experiments.

However, for predicting number concentrations of ice particles realistically, more reliable knowledge about ice nucleation is needed, because they are so sensitive to ice nucleation terms as they are demonstrated in this study.